

# **Guiding of Laser Ablation Plasma by Axial Magnetic Field for a Well-controlled Ion Source**

A thesis presented  
by

Shunsuke Ikeda

Department of Energy Sciences  
Interdisciplinary Graduate School of Science and Engineering  
March 2016



TOKYO INSTITUTE OF TECHNOLOGY



# Contents

Title Page . . . . .	i
Table of Contents . . . . .	iii
List of Figures . . . . .	v
List of Tables . . . . .	ix
Acknowledgments . . . . .	xi
<b>1 Introduction</b>	<b>1</b>
1.1 Laser ablation plasma for heavy ion sources . . . . .	1
1.2 Interaction of laser ablation plasma with axial magnetic field . . . . .	6
1.3 Scope and outline . . . . .	13
<b>2 Effect of Axial Magnetic Field on Plasma Dynamics</b>	<b>15</b>
2.1 Introduction . . . . .	15
2.2 Experimental setup for measurements of plasma ion current density . . . . .	16
2.3 Plasma ion current waveform on axis . . . . .	18
2.3.1 Plasma ion current waveform at a distance from target . . . . .	20
2.3.2 Evolution of current density with distance from target . . . . .	21
2.4 Behavior of tail of plasma plume . . . . .	23
2.4.1 Longitudinal distributions of current density of slices . . . . .	24
2.4.2 Transverse distributions of current density of slices . . . . .	25
2.4.3 Dependency of plasma dynamics on strength of magnetic field . . . . .	29
2.5 Behavior of head of plasma plume . . . . .	30
2.6 Discussion . . . . .	32
2.7 Concluding remarks . . . . .	32
<b>3 Response of Axial Magnetic Field against Plasma Plume Injection</b>	<b>35</b>
3.1 Experimental setup for measurement of diamagnetic field . . . . .	35
3.2 Plasma ion current density measurement . . . . .	39
3.3 Response of axial magnetic field . . . . .	40
3.4 Estimation of diamagnetic current density distribution . . . . .	45
3.4.1 Reconstruction method . . . . .	47
3.4.2 Estimated current density distributions . . . . .	50

3.5	Discussion . . . . .	52
3.6	Concluding remarks . . . . .	54
<b>4</b>	<b>Guiding at Hot-dense Plasma Region</b>	<b>57</b>
4.1	Experimental setup for plasma ion current density measurement . . . . .	58
4.2	Effects of magnetic field applications at hot-dense and lower density re- gions on plasma ion current density . . . . .	63
4.2.1	Application at hot-dense region . . . . .	63
4.2.2	Application at lower density region . . . . .	66
4.3	Dependency on charge state . . . . .	68
4.3.1	Principle of electrostatic ion analyzer and experimental conditions .	68
4.3.2	Flux of ions with various magnetic field . . . . .	70
4.4	Concluding remarks . . . . .	73
<b>5</b>	<b>Plasma Control with Pulsed Magnetic Field</b>	<b>75</b>
5.1	Concept of control with pulsed field . . . . .	75
5.2	Design of solenoid and pulse circuit . . . . .	76
5.3	Effect of pulsed magnetic field . . . . .	83
5.4	Concluding remarks . . . . .	89
<b>6</b>	<b>Conclusions</b>	<b>91</b>
<b>A</b>	<b>Guiding of Plasma with Long Solenoid</b>	<b>95</b>
A.1	Effects on current and total charge of beam extracted from laser ablation plasma . . . . .	95
A.1.1	Experimental setup for beam current measurement . . . . .	96
A.1.2	Results and discussion . . . . .	97
A.1.3	Summary . . . . .	98
A.2	Influence on beam extraction . . . . .	98
A.2.1	Experimental setup for phase space profile measurement . . . . .	100
A.2.2	Results and discussion . . . . .	101
A.2.3	Summary . . . . .	104
A.3	Plasma ion current in solenoid . . . . .	106
A.3.1	Experimental setup for plasma ion current measurement in solenoid	106
A.3.2	Results and discussion . . . . .	108
A.3.3	Summary . . . . .	110
A.4	Concluding remarks . . . . .	110
	<b>Bibliography</b>	<b>111</b>

# List of Figures

1.1	Schematic of temporal structure of plasma ion current density. . . . .	4
1.2	Shape of sheath boundary and beam divergence depending on plasma ion current density. . . . .	5
1.3	Interaction of injected plasma and magnetic field when $R_m \gg 1$ . . . . .	10
1.4	Motions of magnetized electrons and ions in axial magnetic field. . . . .	11
2.1	Schematic of experimental setups for (a) longitudinal and (b) transverse measurement of plasma ion current density. . . . .	17
2.2	Typical waveform of coil current. . . . .	18
2.3	Calculated longitudinal magnetic flux density $B_z$ as functions of (a) longitudinal and (b) transverse distances. . . . .	19
2.4	Configuration of current density detector. . . . .	19
2.5	Photo of current density detector covered with stainless shell. . . . .	20
2.6	Waveforms of plasma ion current densities versus time from laser pulse at a distance of 690 mm from the target, for various magnetic fields at the solenoid center. . . . .	21
2.7	Plasma ion current density on the solenoid axis at various distances from the target with magnetic field of 40 G. . . . .	22
2.8	Time of flight of current density peak $t_{peak}$ and the current density $i_{peak}$ as a function of distance from the target $z$ without magnetic field. . . . .	23
2.9	Slice model of drifting plasma plume. . . . .	23
2.10	Plasma ion current density at a distance of 870 mm. . . . .	25
2.11	Plasma ion current densities of slices whose velocities are (a) 10, (b) 11, (c) 12, and (d) 14 mm/ $\mu$ s as functions of longitudinal distance (each plots was average of 5 data). . . . .	26
2.12	Image of the inner diverging core and the outer converging region . . . . .	27
2.13	Transverse distributions of plasma ion current density for slices whose velocities are (a) 10, (b) 11, (c) 12, and (d) 14 mm/ $\mu$ s. . . . .	28
2.14	Dependence of plasma ion current density on magnetic field for slice with 22 mm/ $\mu$ s . . . . .	30

2.15	Plasma ion current densities of slice with 36 mm/ $\mu$ s with various magnetic field. . . . .	31
2.16	Image of guiding of the head of the plasma plume in the initial phase of the plasma interaction. . . . .	31
2.17	Image of the interaction obtained by measurements of plasma ion current density. . . . .	32
3.1	Experimental setup for measurement of magnetic field. . . . .	36
3.2	Calculated longitudinal magnetic field $B_z$ on $z$ and $x$ axes. . . . .	38
3.3	Schematic diagram of magnetic probe. . . . .	39
3.4	Magnetic field measured by the magnetic probe and calculated from the solenoid current measured by a current transformer (CT). . . . .	39
3.5	Plasma ion current density as a function of time at a distance of 740 mm. . . . .	40
3.6	Estimated plasma ion current density at center of solenoid. . . . .	41
3.7	Three magnetic probe signals as a function of time taken at same condition. . . . .	42
3.8	Averaged magnetic probe signals of both ends. . . . .	42
3.9	$\Delta B_z$ and plasma ion current density as a function of time at the center. . . . .	43
3.10	$\Delta B_z$ as a function of time measured at various longitudinal and transverse distances. . . . .	44
3.11	$\Delta B_z$ as functions of longitudinal and transverse distance at 6, 8, 10, and 14 $\mu$ s after the laser pulse. . . . .	46
3.12	Image of exclusion and drag of magnetic field by plasma plume. . . . .	47
3.13	Calculated and measured $B_z$ on $z$ axis as a function of longitudinal distance and on solenoid midplane as a function of radial distance at 10 $\mu$ s. . . . .	51
3.14	Diamagnetic current density distribution as functions of $r$ and $z$ at (a) 6, (b) 8, (c) 10, (d) 12, (e) 14, and (f) 16 $\mu$ s. . . . .	53
4.1	Schematic of experimental setup for plasma ion current density measurement. . . . .	58
4.2	Diagram of solenoids. . . . .	60
4.3	Calculated magnetic flux density of the solenoids on the axes when the current is 1 A. . . . .	60
4.4	Diagram of pulse circuit energizing solenoids. . . . .	61
4.5	Typical waveform of current in pair of solenoids. . . . .	61
4.6	Schematic of plasma ion current density detector. . . . .	62
4.7	Peak plasma ion current as a function of absolute value of bias voltage. . . . .	62
4.8	Typical waveforms of the ion probe signal with and without the magnetic field generated by the split pair solenoid and target configuration. 3 waveforms taken at same condition are overlaid in each figure. . . . .	64
4.9	Plasma ion current density waveform on the solenoid axis and angular distribution of peak ion current density at a distance of 170 mm from the target with various magnetic fields. . . . .	65

4.10	Plasma ion current density waveform on the solenoidal axis and angular distribution of peak ion current density at a distance of 280 mm from the target with various strengths of magnetic field. . . . .	66
4.11	Plasma ion current density waveform on the solenoidal axis and angular distribution of peak ion current density at $z=170$ mm with various strengths of magnetic field. . . . .	67
4.12	Schematic of electrostatic ion analyzer and arrangements of target and ion probe. . . . .	69
4.13	Overlaid three signals of secondary electron multiplier taken at same $U$ . . .	71
4.14	Flux of each charge as a function of time and estimated plasma ion current density at 1500 mm. . . . .	72
5.1	Image of ablation plasma control with pulsed magnetic field. . . . .	76
5.2	Setup of laser ion source in Brookhaven National Laboratory. . . . .	77
5.3	Dimension of pulse solenoid. . . . .	79
5.4	Calculated magnetic flux on axis as a function of distance from target. . . .	79
5.5	Cut view of pulse solenoid. . . . .	80
5.6	Photo of pulse solenoid. . . . .	80
5.7	Equivalent circuit of the pulse solenoid. . . . .	81
5.8	Typical current waveform of the pulsed circuit. . . . .	82
5.9	Magnetic flux densities calculated from solenoidal current and measured with magnetic probe as a function of time. . . . .	82
5.10	Beam currents as a function of time in the cases of 0 G and 60 G with the some trigger timings $t_{on}$ . . . . .	84
5.11	Estimated current with no magnetic field at center of pulse solenoid. . . . .	86
5.12	Time sequence from pulse compression to extraction. . . . .	87
5.13	Beam currents as a function of time with various pulsed magnetic field amplitudes. . . . .	88
5.14	Example of flat-topped current shape formed by applying pulsed magnetic field of 60 G at $t_{on}=14$ $\mu$ s. . . . .	89
6.1	Illustration of interaction between laser ablation plasma and magnetic field. .	93
A.1	Schematic diagram of experimental setup for beam current measurement. . .	96
A.2	Iron beam current waveforms measured by a current transformer. . . . .	97
A.3	Amplifications of the peak current and the total charge within a beam pulse as a function of the magnetic flux density. . . . .	99
A.4	Schematic diagram of experimental setup for beam profile measurement. . .	101
A.5	Photo of Faraday cup. . . . .	102
A.6	Diagram of Faraday cup. . . . .	102
A.7	Plasma ion current density waveform at the exit of the solenoid. . . . .	102
A.8	Typical phase space profile in X-X' plane. . . . .	103
A.9	Twiss parameters as a function of time from laser shot. . . . .	105

A.10 Schematic diagram of experimental setup for current measurement in solenoid.	107
A.11 Longitudinal components of magnetic flux density on axis as a function of longitudinal distance from entrance of solenoid. . . . .	107
A.12 Plasma ion current at distance waveform of 230 mm from solenoid entrance.	108
A.13 Total charge within a single beam pulse as function of distance from solenoid entrance. . . . .	109



# List of Tables

2.1	Conditions for plasma ion current density measurement. . . . .	16
3.1	Laser conditions for plasma ion current density measurement . . . . .	36
4.1	Laser conditions. . . . .	59
5.1	Laser specifications for laser ion source in Brookhaven National Laboratory.	77
5.2	Laser conditions for plasma ion current density measurement. . . . .	83
A.1	Laser conditions for beam current measurement. . . . .	96
A.2	Laser conditions for beam profile measurement. . . . .	101
A.3	Integrated Twiss parameters. . . . .	103
A.4	Laser specifications for current measurement in solenoid. . . . .	106



# Acknowledgments

This thesis has been supported tremendously from numerous people. I would like to express my deepest appreciation to many people.

First, I would like to acknowledge my supervisor Professor Kazuhiko Horioka at Tokyo Institute of Technology. He encouraged me since I was an undergraduate student. He always answered my questions on physics, direction of research, and the course earnestly. This thesis could not have been possible without his help.

I would like to thank Dr. Masahiro Okamura at Brookhaven National Laboratory. In Ph.D. course, he taught me physics, experiments, and how to live in the US. I had fruitful time there through his help.

I would like to express my gratitude to Dr. Hideto En'yo at RIKEN. He supported my research in Ph.D. course in many aspects. Discussions with him were helpful and interesting. In addition, his and his group's friendly atmosphere were impressive and I had fun in some events with them. Without his help, I could not live the full study life.

I would like to thank Assistant Professor Mitsuo Nakajima at Tokyo Institute of Technology. He taught me physics, mathematics, biology, economics, history, cooking, and so on. His talk always stimulated my intellectual curiosity.

I would like to appreciate Associate Professor Jun Hasegawa at Tokyo Institute of Technology. He is enthusiastic for education. He taught me physics and academic writing earnestly. Discussion with him improved this thesis in many respects.

I would like to express my appreciation to Associate Professor Tohru Kawamura at Tokyo Institute of Technology. His comments on my study, this thesis, and attitude as researcher were to the point and helpful.

I would like to thank Dr. Takeshi Kanetsue at Brookhaven National Laboratory. He is a diligent and friendly person, and possesses knowledge on physics and techniques of accelerators especially for laser ion source. He helped me for the experiments and the life in the US kindly.

I would like to thank Dr. James Alessi, Dr. Edward Beebe, and Dr. Alexander Pikin at Brookhaven National Laboratory. They gave welcome to me. Conversations with them in coffee break were very fun.

I would like to express my appreciation to Mr. Michael Costanzo, Mr. Robert Lambiase, and Mr. Chong-Jer Liaw at Brookhaven National Laboratory. Thanks to their cooper-

ation, we could develop a device discussed in this thesis successfully.

I would like to thank Dr. Huanyu Zhao at Institute of Modern Physics. She and her group members welcomed me to their laboratory. Thanks to them, I had fun in the visit.

I would like to thank the member of thesis committee; Professor Ken Takayama (KEK), Associate Professor Noriyosu Hayashizaki (Tokyo Institute of Technology) for their kind reviews of this thesis.

Special thanks are due to Horioka, Kawamura, Takayama laboratory members (Mr. Yasuo Sakai, Ms. Fumika Isono, Mr. Tomoaki Kawasaki, Mr. Yoshiki Shou, Mr. Kenta Kawaguchi, Mr. Tomonobu Itagaki, Mr. Shotaro Kittaka, Mr. Daisuke Nishii, Mr. Seiichi Yoshioka, Mr. Rimpei Chiba as the present members, Dr. Kazumasa Takahashi, Dr. Adachi Koichiro, Dr. Xigguang Liu, Mr. Shuichi Yamamura, Mr. Nao Tatsumura, Mr. Takashi Yoshimoto, Mr. Naoya Munemoto, Mr. Seika Liu, Mr. Ken Yonezawa, Mr. Masashi Masuda, Mr. Akihito Tezuka, Mr. Koki Kano, Mr. Kaneo Kato as the graduates) and other colleagues (Dr. Kotaro Kondo, Dr. Jun Tamura, Ms. Megumi Sekine, Mr. Takayuki Sako, Dr. Yoshihiro Morimoto, Mr. Akira Kawasaki, Mr. Masafumi Kumaki, Mr. Yasurio Fuwa) could help my study life to be fruitful.

In addition, I gratefully acknowledge financial support by Junior Research Associate program at RIKEN.

Finally I would like to thank my family for their supports and encouragements.

Yokohama, Japan

*Shunsuke Ikeda*

# Chapter 1

## Introduction

### 1.1 Laser ablation plasma for heavy ion sources

Heavy ion accelerators have applications in a variety of fields of science and technology. Some accelerators are operated or under construction for the production of relativistic heavy ions [1,2], or for rare isotope beam [3–6] used for studies on nuclear physics. Other accelerators are used for the biological effect, such as cancer therapy [7], a cosmic ray simulator [8], and a beam-breeding of plants [9]. Among them, sources with extremely high-flux have been searched for energy drivers of heavy ion inertial fusion [10,11].

For the accelerators, both the current and the emittance are important because these determine the power level, the reaction rate, the energy deposition, and/or the accelerator size. Those parameters are basically conserved throughout the accelerators and thus the available parameter regions are limited by the quality of the ion source. Therefore, a high current and low emittance source is desired in all of the application fields. We aim to improve the ion source performance using a plasma produced by laser ablation process.

When a solid is irradiated with a high power laser, the solid surface is vaporized and then, electrons are generated by a multi-photon absorption process. The electrons are accelerated through an absorption process dominated by the inverse bremsstrahlung and the energized electrons make free electrons through successive impact ionizations. By the chain reactions, a large amount of electrons and ions are generated and, consequently a part of the target material evolves to a dense plasma. This phenomena accompanied by the laser

absorption, the vaporization of target material, the ionization, and the plasma evolution is called "Laser ablation".

The ablation plasma has advantageous features for heavy ion sources [12]. The advantages are: (1) reproducible ion supply, (2) ion production with highly charged state, (3) capability of producing many types of ions, (4) compatibility with high vacuum, and (5) simplicity. Because of the features, many researchers have studied the source [13–15]. For example, researchers at Institute for Theoretical and Experimental Physics -Moscow [16] produced  $\text{Pb}^{27+}$  ions with 100 J and  $3 \times 10^{13} \text{W/cm}^2$   $\text{CO}_2$  laser. In addition, Au beams containing  $\text{Au}^{1+}$  to  $\text{Au}^{52+}$  were produced with 26 J and  $5 \times 10^{14} \text{W/cm}^2$  iodine laser by Picciotto *et al.* [17]. Alternatively, a laser ion source has been developed in Brookhaven National Laboratory [18] to produce primary ions for the electron beam ion source [19]. The source was used for the Relativistic Heavy Ion Collider and the irradiation facility at NASA Space Radiation Laboratory.

Besides those, the plasma has advantages for a high current and low emittance ion source. The plasma density can be increased to the critical density described by

$$n_{cr} = \frac{\omega_L^2 m_e \epsilon_0}{e^2}, \quad (1.1)$$

where  $\omega_L$  is the laser frequency,  $m_e$  is the electron mass,  $e$  is the elemental charge,  $\epsilon_0$  is the permittivity of vacuum. For example, the critical number density for Nd:YAG laser is estimated to be  $\sim 10^{21} \text{cm}^{-3}$ . With low power density laser  $\sim 10^8 \text{W/cm}^2$ , it was reported that the ablation plasma can produce 87  $\mu\text{C}$  from a Cu target [20]. If the all the ions are in 100  $\mu\text{s}$  beam pulse, the current corresponds to  $\sim 1 \text{A}$ . This is two orders of magnitude larger than typical ion sources [21, 22]. The current is expected to increase more by irradiation with shorter pulse width and/or larger power density.

Furthermore, the ablation plasma expands adiabatically from a high density state to a low density and finally to a collisionless state. Consequently, the plasma obtains a drift velocity while the temperature decreases. In typical static ion sources, intrinsic beam emittance depends on ion temperature and plasma current density available in an extraction

electrode is limited by the Bohm criterion which can be described by [23]

$$J_{\text{Bohm}} = n_p e \sqrt{\frac{kT_e}{m_i}}, \quad (1.2)$$

where  $n_p$  is ion density at the plasma-sheath boundary,  $k$  is the Boltzmann constant,  $T_e$  is electron temperature, and  $m_i$  is ion mass. Therefore, there is a trade-off between high beam current and low emittance.

On the other hand, when the drift velocity dominates the ion flux, the limit of the plasma ion current density is described as  $Zen_i v_d$ , where  $Z$  is the charge state,  $n_i$  is the ions number density, and  $v_d$  is the drift velocity. Then the current density from the ablation plasma does not depend on the thermal velocity. Therefore, the plasma is expected to be a high current and low emittance source while avoiding the trade-off.

However, some issues remain in the expansion phase after the production. In a typical configuration, the plasma expands without external field. After the expansion phase, the plasma becomes collisionless gradually and spreads almost three-dimensionally with drifting. The longitudinal width of the plasma determines the pulse width of the extracted beam. That is, to obtain a required pulse width, the plasma should be spread to the corresponding length. Thus the plasma has to be transported for a long distance far beyond the expansion limit. Since the plasma also diverges transversely, the density varies within the plume. For instance, the divergent angle was more than 20 degree with  $10^8 - 10^{13} \text{ W/cm}^2$  nano-second laser [20, 24, 25]. Thus, without any guiding devices, most of the ions escape out of an aperture of an extractor.

In addition, the plasma ion current density at an extractor varies with time. In the case that laser pulse duration is less than the specific time of the plasma flow, the velocity is often described as a drifted Maxwellian profile [26]

$$f(v_x, v_y, v_z) = \left( \frac{m}{2\pi kT} \right)^{3/2} \exp \left( \frac{-m(v_x^2 + v_y^2 + (v_z - v_d)^2)}{2kT} \right), \quad (1.3)$$

where  $z$  is drifting direction,  $x$ ,  $y$  are transverse directions,  $m$  and  $v_x$ ,  $v_y$ ,  $v_z$  are mass and velocities of an ion, and  $T$  is temperature of ions. In this case, the plasma ion current

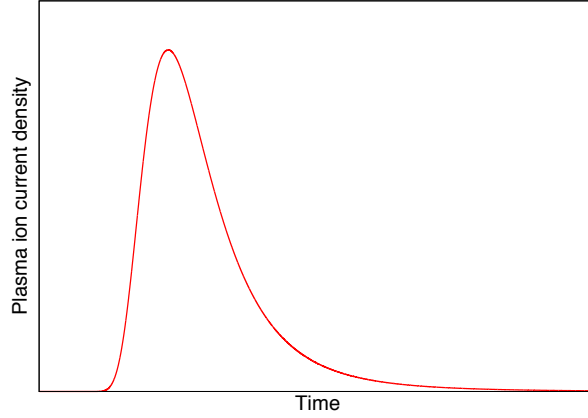


Figure 1.1: Schematic of temporal structure of plasma ion current density.

density  $i$  at a distance large enough to take the laser spot size as a point is described by

$$i \propto L^2 t^{-5} \exp \left( \frac{-m}{2kT} \left( \frac{L}{t} - v_d \right)^2 \right), \quad (1.4)$$

where  $L$  is distance from a target surface. A typical time-evolution of the ion current density is shown in Fig.1.1.

In an extractor, the electrons in the injected plasma are repelled while the ions are accelerated. Then a sheath boundary is formed between the plasma and the beam. The boundary is also defined as an edge of the plasma from which ions are accelerated. The boundary has a three dimensional shape. The shape is determined by a difference between the plasma ion current density  $J_p$  and a current density specific to the electrode  $J_{CL}$  as shown in Fig. 1.2, where  $J_{CL}$  is the Child-Langmuire current density described by

$$J_{CL} = \frac{4\epsilon_0}{9} \sqrt{\frac{2e}{m}} \frac{V^{\frac{3}{2}}}{d^2}, \quad (1.5)$$

where  $V$  and  $d$  is voltage and gap width, respectively. Since the electric field is normal to the boundary surface, the ions are emitted in that direction. Therefore, (a) the beam converges when  $J_p < J_{CL}$ , (b) the beam is extracted parallel when  $J_p = J_{CL}$ , and (c) the beam diverges when  $J_p > J_{CL}$ .

As has been discussed above, the ion current of laser ablation plasma,  $J_p$  varies with



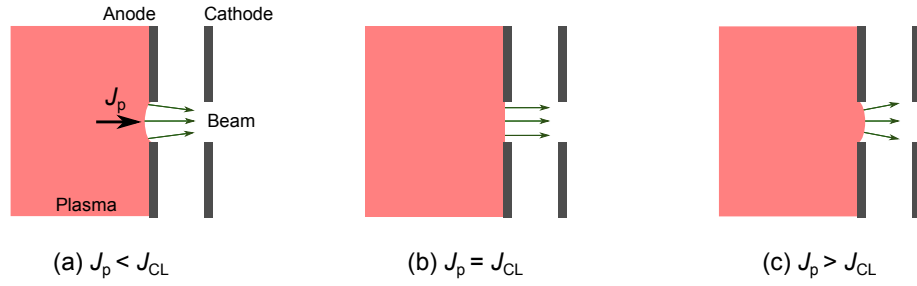


Figure 1.2: Shape of sheath boundary and beam divergence depending on plasma ion current density.

the time. This means that the divergence varies within a beam pulse depending on the current and the transverse phase space distribution of ions rotates within the beam pulse. To transport such a beam, the accelerator acceptance needs to contain the whole area swept by the rotating distribution, which is larger than the distribution at a given time. As a result, the effective emittance becomes larger.

In addition, the variation of the plasma ion current density leads to the variation of the current of the extracted beam. The variation causes a change of space charge effect within the beam pulse.

To overcome the problems, a method to control the plasma is necessary. As has been reported, for this purpose, guiding by axial magnetic field is considered to be useful [14, 27–29]. Wolowski *et al.* observed two or three times enhancement of the plasma ion current density when they applied a field of 4.5 kG generated by a Helmholtz coil [30]. Okamura *et al.* reported that solenoidal magnetic field of 200 G enhances the current density by four times [31]. In addition, as discussed in the Appendix of this thesis, solenoidal field is effective for the control of ion current density. These results indicate that, by using the guiding properly, we can develop an ion source with high current and low emittance. However, any discussions in the previous studies are limited within phenomenological understanding. In order to control the ablation plasma for a novel ion source, we need to make the interaction process between the plasma and axial magnetic field clear.

## 1.2 Interaction of laser ablation plasma with axial magnetic field

Typically, the interaction of plasma with magnetic field is discussed with Magnetohydrodynamic (MHD) equations. In this section, first we introduce the equations of motion and induction equation, and from them we derive the magnetic Reynolds number to show the qualitative behavior of the interacting plasma [32].

First, we assume the following:

- fully ionized state
- quasi-neutrality
- $m_e \ll m_i$
- $T_e = T_i$
- isotropic distribution functions for both electrons and ions
- non relativistic

where  $m_\alpha$  and  $T_\alpha$  are the mass and the temperature of electrons or ions. In this case, the plasma behaves as a single fluid and the equation of motion is

$$\begin{aligned}
 \rho \frac{dv}{dt} &= -\nabla p + \mathbf{j} \times \mathbf{B}, \\
 \rho &= \rho_i + \rho_e = n_e m_e + n_i m_i \approx \rho_i, \\
 \mathbf{v} &= \frac{\rho_i \mathbf{v}_i + \rho_e \mathbf{v}_e}{\rho} \approx \mathbf{v}_i, \\
 p &= p_e + p_i, \\
 \mathbf{j} &= -n_e e (\mathbf{v}_e - \mathbf{v}_i),
 \end{aligned} \tag{1.6}$$

where  $\mathbf{B}$  is the magnetic field,  $n_\alpha$  is the number density,  $m_\alpha$  is the mass,  $\mathbf{v}_\alpha$  is the mean velocity, and  $p_\alpha$  is the pressure of electrons or ions.

In addition, the ohm's law can be derived as

$$\mathbf{E} = -(\mathbf{v} \times \mathbf{B}) + \frac{\mathbf{j}}{\sigma} + \frac{1}{en_e}(\mathbf{j} \times \mathbf{B}) - \frac{1}{en_e} \nabla p_e, \tag{1.7}$$

where  $\mathbf{E}$  is electric field and  $\sigma$  is plasma conductivity. Then if the Larmor radius of ions  $r_L$  is much smaller than the typical length scale  $L$ , namely

- $r_L/L \ll 1$ ,

the third and fourth terms in the right hand of Eq.1.7 become negligibly small compared to the first term. Then we obtain the following,

$$\mathbf{E} = -(\mathbf{v} \times \mathbf{B}) + \frac{\mathbf{j}}{\sigma}. \quad (1.8)$$

From the non relativistic assumption ( $v/c \ll 1$ ), Maxwell's equations are simplified as follows:

$$\begin{aligned} \nabla \times \mathbf{E} &= -\frac{\partial \mathbf{B}}{\partial t}, \\ \nabla \cdot \mathbf{B} &= 0, \\ \nabla \times \mathbf{B} &= \mu_0 \mathbf{j}, \end{aligned} \quad (1.9)$$

where  $\mu_0$  is permeability of vacuum. By combining the first equation and Eq.1.8, we obtain the following (magnetic) induction equation,

$$\frac{\partial \mathbf{B}}{\partial t} = \nabla \times (\mathbf{v} \times \mathbf{B}) + \frac{1}{\sigma \mu_0} \nabla^2 \mathbf{B}. \quad (1.10)$$

The induction equation describes the variation of the magnetic field induced by a plasma. Here, we consider the total time derivative of the magnetic flux through a closed curve that moves with the plasma.

From, analysis of vector field and  $\nabla \cdot \mathbf{B} = 0$ , we obtain

$$\frac{d}{dt} \int_S \mathbf{B} \cdot \mathbf{n} = \int \left( \frac{\partial \mathbf{B}}{\partial t} - \nabla \times (\mathbf{v} \times \mathbf{B}) \right) \cdot \mathbf{n} dS. \quad (1.11)$$

Then, if we can neglect the second term in the right hand side of Eq.1.10, Eq.1.10 becomes

$$\frac{\partial \mathbf{B}}{\partial t} = \nabla \times (\mathbf{v} \times \mathbf{B}). \quad (1.12)$$

This leads to

$$\frac{d}{dt} \int_S \mathbf{B} \cdot \mathbf{n} = 0. \quad (1.13)$$

This means that the magnetic flux is conserved in the plasma at any time, or the magnetic field line are frozen to the plasma. Therefore, the first term represents the convective effect of the plasma. The typical time scale of this convective process  $\tau_c$  is determined by the motion of the plasma, thus

$$\tau_c = \frac{L_t}{u}, \quad (1.14)$$

where  $L_t$  is the typical length and  $u$  is the typical velocity.

On the other hand, if we can neglect the first term of Eq. 1.10, Eq. 1.10 becomes,

$$\frac{\partial \mathbf{B}}{\partial t} = \frac{1}{\sigma \mu_0} \nabla^2 \mathbf{B} \quad (1.15)$$

This is a diffusion equation. Therefore, the first term represents the magnetic field diffusion due to the finite value of conductivity  $\sigma$ . To estimate the typical time scale of this diffusion process  $\tau_d$ , we can modify the equation as follows:

$$\frac{B}{\tau_d} = \frac{1}{\sigma \mu_0} \frac{B}{L_t^2}. \quad (1.16)$$

Then, we obtain

$$\tau_d = L_t^2 \sigma \mu_0. \quad (1.17)$$

As shown in Eq. 1.10, the magnetic field is influenced by both of the convective and the diffusive effects. To see which effect dominates, the ratio of the timescales are used. Namely, the ratio can be described as follows:

$$R_m = \frac{\tau_d}{\tau_c} = \sigma \mu_0 u L_t. \quad (1.18)$$

This ratio is called magnetic Reynolds number that indicates the qualitative interaction

process between the plasma and the magnetic field.

For example, when  $R_m \gg 1$  such as in the case of interaction of a perfect conductor ( $\sigma = \infty$ ), the induction equation reduces to Eq.1.12 and we know that the magnetic field is frozen or completely excluded from the plasma.

On the other hand, the plasma is influenced by the magnetic field via a Lorentz force  $\mathbf{j} \times \mathbf{B}$  in Eq.1.6. By using  $\nabla \times \mathbf{B} = \mu_0 \mathbf{j}$ , the term becomes

$$\begin{aligned} \mathbf{j} \times \mathbf{B} &= \frac{1}{\mu_0} (\mathbf{B} \cdot \nabla) \mathbf{B} - \nabla \left( \frac{B^2}{2\mu_0} \right) \\ &= -\nabla_{\perp} \left( \frac{B^2}{2\mu_0} \right) + \frac{B^2}{\mu_0 R_c} \mathbf{e}_n, \end{aligned} \quad (1.19)$$

where  $\nabla_{\perp}$  is  $\nabla$  operator perpendicular to the magnetic field lines,  $R_c$  is the local radius of curvature,  $\mathbf{e}_n$  is the unit vector in the direction from the local center of curvature to the point of interest.  $B^2/2\mu_0$  in the first term of Eq. 1.19 is called magnetic pressure. The gradient is the force perpendicular to the magnetic field line and it induces the force to the plasma from a high pressure to a low pressure regions similar to the force induced by the gas pressure in the conventional hydrodynamics. The second term is the magnetic tension force that is driven when the magnetic field line is bent.

These mean that the force to the plasma is driven by the field distortions, namely compression and/or bending, of the magnetic field. On the other hand, the distortion is driven by the plasma according to the induction equation Eq. 1.10. So, the plasma and the magnetic field interact in a manner described by the equations and qualitatively the interaction process can be characterized by  $R_m$ .

Here we show the interaction for a simple case in which a plasma plume is injected into an axial magnetic field under the condition of  $R_m \gg 1$  as shown in Fig.1.3. Because  $R_m \gg 1$ , Eq. 1.12 can be applied for the process. Therefore, the magnetic flux through the plasma is conserved. This means that the change in the flux is 0 at any time. So, the plasma excludes the magnetic field completely. On the other hand, due to the distortion, the difference of the magnetic pressure occurs between the inside and outside of the magnetized region. Therefore, the plasma is compressed radially by the magnetic pressure.

This process is described by the snowplow model [33]. In this model, the surface is

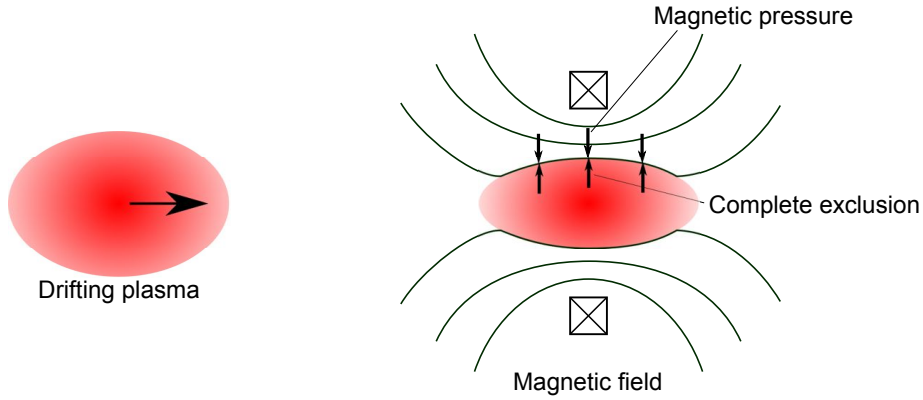


Figure 1.3: Interaction of injected plasma and magnetic field when  $R_m \gg 1$ .

compressed to the center with sweeping the inner plasma. All of the plasma is accumulated within the surface and obtain velocity of the surface. We consider a condition in which the plasma is long enough for variations along the longitudinal distance to be small. Then the equation of motion is described as

$$2\pi r_s(P_m - P_p) = -\frac{d}{dt} \left( M \frac{dr_s}{dt} \right), \quad (1.20)$$

where  $P_m$  is the magnetic pressure,  $P_p$  is the plasma kinetic pressure,  $r_s$  is the surface radius, and  $M$  is the mass of the surface per unit length. When the initial radius is denoted by  $r_0$ , then

$$M = \pi n_e(r_0^2 - r_s^2)(m_i + m_e). \quad (1.21)$$

If the plasma is collisionless and adiabatic,  $P_p V^2$  is constant, where  $V$  is the volume. It leads to

$$P_p = P_{p,0} R^{-4}, \quad (1.22)$$

where  $R = r_s/r_0$ .

Therefore, in this simplified case, the plasma and the magnetic field interacts by pressing the surface. In this case, the pressure can be estimated easily.

Another simple case is the guiding with the parameter region where  $R_m \ll 1$ . In this

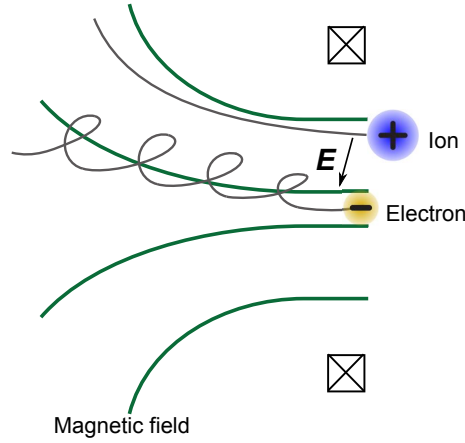


Figure 1.4: Motions of magnetized electrons and ions in axial magnetic field.

case, the magnetic field diffuses into the plasma plume immediately. The ions and electrons move along the magnetic field while the particles are attracted to maintain the charge neutrality as shown in Fig. 1.4.

We have studied the interaction of the plasma and the magnetic field based on the Magnetohydrodynamical model. On the other hand, if the number density becomes low, the ions and the electrons become collisionless and the distortion of magnetic field become negligible small. In this case, the particles move along the magnetic field while attracting each other electrically to maintain the charge neutrality. A collective focusing model was developed to describe the process in a neutralized high current ion beam with a density of  $10^{10} \text{ cm}^{-3}$  [33–37].

This can be modeled as a cylinder of singly charged ions and electrons injected into an axial field. The Lagrangians of the electrons and the ions are described by

$$L_{\alpha} = \frac{1}{2}m_{\alpha}V_{\alpha}^2 + q_{\alpha}V_{\alpha} \cdot \mathbf{A} - q_{\alpha}\phi, \quad (1.23)$$

where  $m_{\alpha}$  is the mass,  $V_{\alpha}$  is the velocity,  $q_{\alpha}$  is the charge of each particle,  $\mathbf{A}$  is a vector potential, and  $\phi$  is the electric potential. Because of the axial symmetry, the vector potential has only an azimuthal component, that is  $\mathbf{A} = A_{\theta}\mathbf{e}_{\theta}$ . In this symmetry, the canonical

angular momentum is conserved and described by

$$P_{\theta,\alpha} = m_\alpha r^2 \frac{\partial \theta_\alpha}{\partial t} - q_\alpha r A_\theta = \text{const.} \quad (1.24)$$

The constant value depends on the situation. In our case, since the particles are injected from the outside,  $P_{\theta,\alpha} = 0$ . Furthermore, we assume that the positions of the electrons and the ions are the same to maintain the charge neutrality, namely  $r = r_e = r_i$ , and  $z = z_e = z_i$ . It leads to the equations of motion and electric field:

$$\frac{\partial^2 r}{\partial t^2} + \left( \frac{e^2}{m_e m_i} \right) A_\theta \frac{\partial A_\theta}{\partial r} = 0, \quad (1.25)$$

$$E_r = \frac{e}{m_e m_i} (m_e - m_i) A_\theta \frac{\partial A_\theta}{\partial r}, \quad (1.26)$$

$$\frac{\partial^2 z}{\partial t^2} + \left( \frac{e^2}{m_e m_i} \right) A_\theta \frac{\partial A_\theta}{\partial z} = 0, \quad (1.27)$$

$$E_z = \frac{e}{m_e m_i} (m_e - m_i) A_\theta \frac{\partial A_\theta}{\partial z}. \quad (1.28)$$

As shown above, the equations of motion are the same as those of a particle with mass of  $\sqrt{m_e m_i}$ . This shows that, in this condition, the gyroradius of the ion becomes smaller because of the attractive force of the electric field.

We reviewed the interaction in the parameter region where  $R_m \gg 1$  and  $R_m \ll 1$ , and the behaviors of low density electrons and ions. For laser ablation plasma, the density varies from about solid density to low density where the ions and electrons behave as single particles as the plasma expands and spreads. Therefore, the behaviors of the particles and the magnetic field depend on the expansion phase. To control many particles for a high current ion source, we need to consider the high or moderate density region in which the interaction is characterized with  $R_m$ .

$R_m$  depends on the plasma velocity and the conductivity, hence the temperature. The ablation plasma is produced with high temperature and density, and then expands resulting in a decrease of those parameters and an increase in the velocity. When we apply a magnetic field to control the plasma in this parameter region, the corresponding  $R_m$  is estimated to be around 1. For example, a Cu plasma produced by a laser irradiation with  $8 \times 10^8 \text{ W/cm}^2$



has a temperature of about 0.5 eV, a density of  $10^{13} \text{ cm}^{-3}$ , and a velocity of  $3 \times 10^4 \text{ m/s}$  at a distance of 5 cm from the target [38]. The resistivity can be estimated from the Spitzer resistivity in emu [39],

$$\begin{aligned}\eta &= \frac{3.8 \times 10^{12} Z \ln \Lambda}{\gamma_E T^{\frac{3}{2}}}, \\ \Lambda &= \frac{3}{2Ze^3} \left( \frac{k^3 T^3}{\pi n_e} \right)^{\frac{1}{2}},\end{aligned}\tag{1.29}$$

where  $Z$  is the charge state of the ion,  $\gamma_E$  is a coefficient concerning internal degree of atomic structure as a function of  $Z$ . Then the resistivity is estimated to be  $1 \times 10^{-3} \Omega \text{ m}$ , assuming  $Z = 1$ . In addition, since typically the extraction electrode of ion sources is 10 mm, we assume that the typical length  $L$  is 10 mm. Then we obtain  $R_m=0.4$  to characterize the interaction.

In the interaction with the parameter region where  $R_m \sim 1$ , both of the convective and the diffusive effects play some role. In other words, the plasma should be partially magnetized and partially convective. In addition, the plasma velocity, the density, and the temperature vary in the plume [40–44]. Furthermore, the plasma is forced by the magnetic field and, at the same time, the magnetic field is distorted by the plasma. Therefore, the interaction should give a structure to the laser plume. In order to utilize the guiding effect, the structure in the plasma plume are needed to be made clear.

### 1.3 Scope and outline

The aim of this thesis is to investigate the interaction processes between a laser ablation plasma and an axial magnetic field with  $R_m \sim 1$  and thereby to elucidate the guiding mechanism for controlling the ablation plasma. For this purpose, we investigate the behavior of laser ablation plasma through an axial magnetic coil. The guiding mechanism is discussed from the view point of ion source. We propose and demonstrate two ways to guide the plasma that result in a well-controlled ion source.

The thesis started with an introduction of laser ablation ion source. Advantages and issues of the ablation plasma for ion sources were discussed in the introduction in which

the motivation of this study was also shown.

In chapter 2, the influence of the magnetic field on the plasma behavior is discussed based on measurements of plasma ion current density. The temporal and spatial distributions of plasma ion current density were measured with an ion probe. The results show that the plasma behaves differently depending on the position within the plasma plume. This indicates that the difference of the magnetization level of the plasma causes the different behavior.

In chapter 3, response of the magnetic field to the injection of the plasma is discussed. The variation of the magnetic field is measured by a magnetic probe. The results show the magnetization progresses temporally and spatially within the plasma plume. From comparisons of the results with the ion probe measurements in chapter 2, the structures of the plasma plume and the magnetic field is correlated. The results show that the the head of the plume near the axis is well-directed by the magnetic field. The guiding mechanism is desirable for the ion source because one can guide the plasma without strong magnetization.

In chapter 4, we investigate the guiding during the early phase of plasma expansion. In the expansion, the temperature is higher and hence the magnetic Reynolds number is higher than those discussed in the chapters 2 and 3. In this parameter region, more plasma is expected to be directed by the magnetic field. The plasma ion current density measurements support the expectation.

In chapter 5, we propose a method for pulse shape control by a fast rising magnetic field. If we apply the field rising faster than the characteristic time of the plasma flow, the field is expected to press the part of the plasma and make a guide effect. We design a fast field coil and apply such a field to the plasma plume tail. We observed the partial enhancement of the current density and demonstrated a modulation of the current waveform to a flat-topped shape.

In chapter 6, we summarize the results and discussions and finally conclude the thesis with an illustration of the guiding effects for controlling of the laser ion source based on our findings.

## Chapter 2

# Effect of Axial Magnetic Field on Plasma Dynamics

As indicated in chapter 1, effect of an axial magnetic field on laser ablation plasma is expected to be different within the plasma plume. In this chapter, the effects on the plasma dynamics will be discussed based on measurements of plasma ion current density [45, 46].

First, from a measured plasma ion current density, the magnetic Reynolds number is estimated to be around 1 at the interaction region. Then, time-space distribution of the plasma ion current density is analyzed with a slice model to discuss the differences of the effects of the magnetic field within the plume.

### 2.1 Introduction

After the production in vacuum, the plasma plume expands rapidly and then collisions between ions become negligible small gradually. Typically, if the distance between the target and an ion detector is much larger than the spot size, it is assumed that the ions evolve from a point source to the free space with a shifted Maxwellian velocity distribution. In such a case, temporal and spatial distribution of the plasma ion current density has been analyzed. We think the Cartesian coordinate in which the origin is the laser spot,  $z$  direction is normal to the target surface, and  $x$  and  $y$  are perpendicular to  $z$  axis. Kelly *et al.* showed that the plasma ion current density waveform on  $z$  axis is described by  $i(t, z) \propto z^{-3} g(z/t)$ ,

Table 2.1: Conditions for plasma ion current density measurement.

Laser Model	THALES SAGA 230
Laser type	Nd:YAG Laser
Wave length	1064 nm
Pulse width (FWHM)	6 ns
Spot size	0.1 cm <sup>2</sup>
Laser energy on target	380 mJ
Power density	$6 \times 10^8$ W/cm <sup>2</sup>

where  $g(w) = w^5 f(w)$ ,  $f(w) = f(0, 0, w)$ , and  $f(v_x, v_y, v_z)$  is the velocity distribution function. A typical waveform is shown in Fig. 1.1. Typically, plasma ion current density waveform has a peak. Since the shape of the plasma ion current density waveform depends on  $g(z/t)$  only, the ratio of  $z$  to the time of flight of the current density peak  $t_{peak}$  is constant. Namely,  $z/t_{peak} = w_{peak}$  is constant. Moreover, the current density peak  $i_{peak}$  is described by  $i(t_{peak}, z) \propto z^{-3} g(z/t_{peak}) = z^{-3} g(w_{peak}) \propto z^{-3}$ . On the other hand, Kools *et al.* showed that the angular distribution of the plasma ion current density is approximately proportional to  $\cos^p \theta$ , where  $p$  is a constant and  $\tan \theta = \sqrt{x^2 + y^2}/z$  [47].

If an axial magnetic field is applied, the plasma dynamics is affected in the field. Then after the interaction, the ions move without collisions with the other ions. From this view point, by comparing the distribution of the plasma ion current density after the interaction to that without magnetic field, we can understand the affected plasma dynamics and the effect of the magnetic field.

## 2.2 Experimental setup for measurements of plasma ion current density

Figures 2.1 (a) and (b) are schematic diagrams of the experimental setups. An iron target was placed in a vacuum chamber evacuated to less than  $4 \times 10^{-4}$  Pa. The target was irradiated with a Nd-YAG laser with conditions shown in Table 2.1. The laser around the power density produces singly charged ions mainly [48]. The ablation plasma expands and drifts in the direction normal to the target surface.

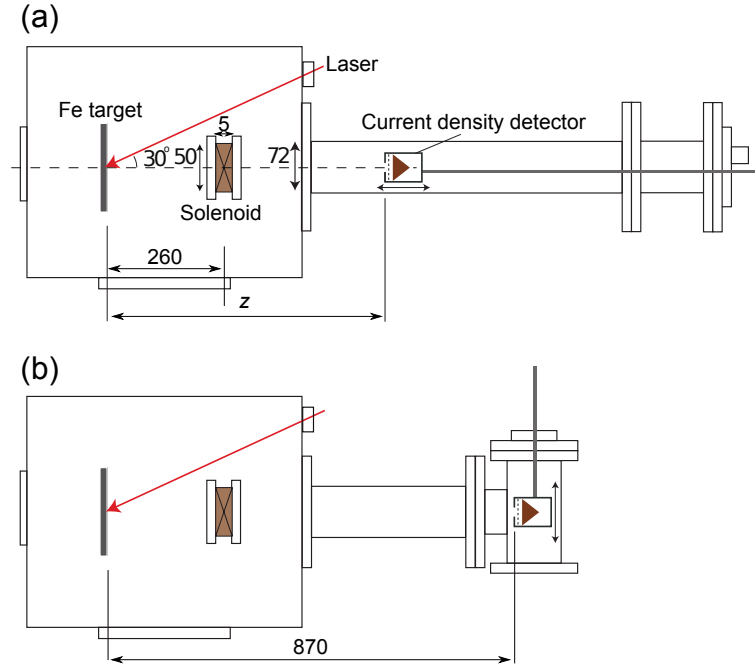


Figure 2.1: Schematic of experimental setups for (a) longitudinal and (b) transverse measurement of plasma ion current density.

An axial magnetic field was applied to the drifting plasma. The magnetic field was generated by a 6-turn short solenoid with 50 mm in diameter and 5 mm in length. The solenoid was placed 260 mm from the target. A quasi-steady current was driven in the solenoid by a pulse circuit composed of a 50 microfarad storage capacitor. Figure 2.2 shows a typical waveform of the coil current measured with a current transformer (Pearson, Current Transformer Model 4160). The fitting function of current was proportional to  $\{\exp(-2.9 \times 10^3 t) - \exp(-9.66 \times 10^5 t)\}$ , where  $t$  is the time in second from the start of the discharge. The discharge was driven 10  $\mu$ s before the laser shot in order that the plasma passed through the solenoid during the decay of the current in the solenoid. Because the solenoid current decayed by only 5% during the time of the plasma passes,  $\sim 20 \mu$ s, we can regard the total magnetic flux as almost constant during the interaction. The magnetic field was calculated with a software (OPERA). Figures 2.3 (a) shows the longitudinal magnetic flux density  $B_z$  on the axis as a function of the longitudinal distance from the target,  $z$ . Figures 2.3 (b) shows  $B_z$  at the solenoid midplane as a function of the transverse distance from the axis. The solenoid was covered by aluminum sheets for electric shielding in order

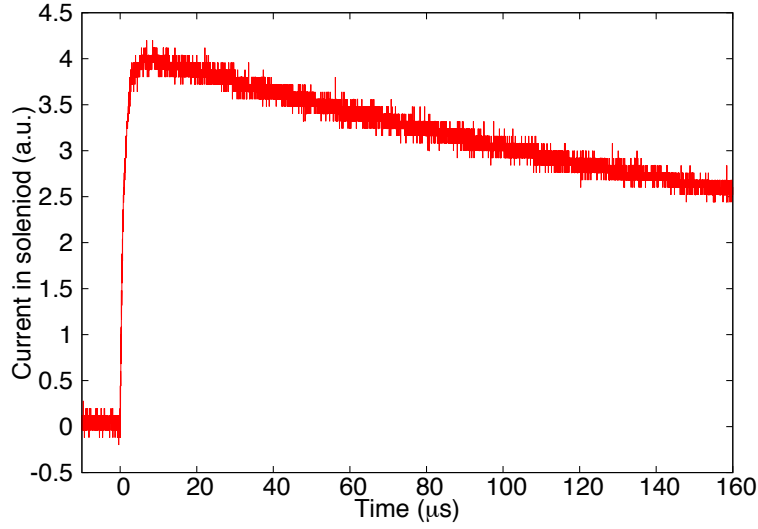


Figure 2.2: Typical waveform of coil current.

not to disturb the plasma. In addition, the sheets were separated with axial spaces to prevent the eddy current induced by the pulsed magnetic field.

The plasma ion current density was measured with a current density detector. The configuration and the photo are shown in Fig. 2.4 and Fig. 2.5. We grounded the metal mesh and applied -180 V on the copper cup to repel the co-moving electrons in the plasma that passed through an 2-mm-diameter aperture in front of the mesh. On the other hand, the ions that passed through the aperture were accelerated toward the cup and then detected as a current. The plasma ion current density was obtained by dividing the measured ion current by the aperture area. The components were covered by a stainless steel shell. The detector was scanned with changing longitudinal and transverse distances in the setups shown in Fig. 2.1(a) and (b).

## 2.3 Plasma ion current waveform on axis

In this section, first, we show the plasma ion current density waveform measured at a distance from the target with various magnetic field. From the waveform, we discuss effects of the field on the plasma plume. Next, we show waveforms measured at various distances with a strength of the magnetic field. Then, we introduce a slice model to analyze

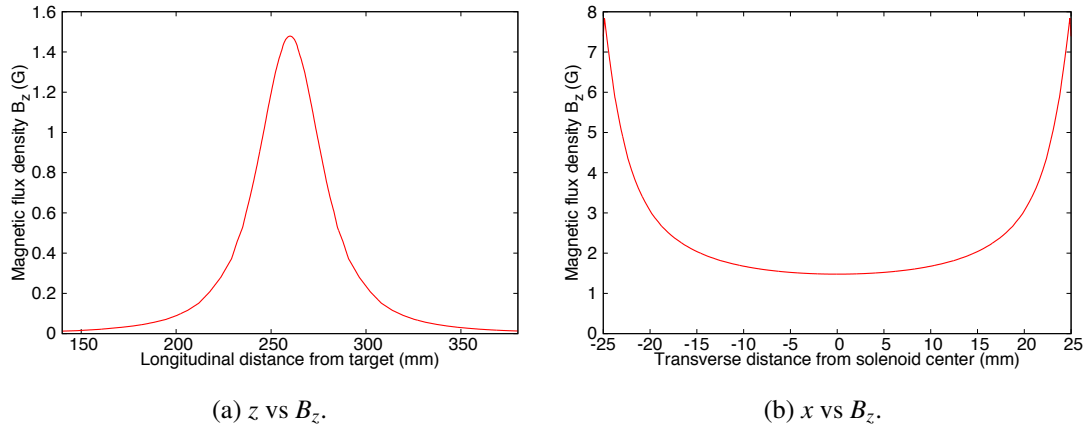


Figure 2.3: Calculated longitudinal magnetic flux density  $B_z$  as functions of (a) longitudinal and (b) transverse distances.

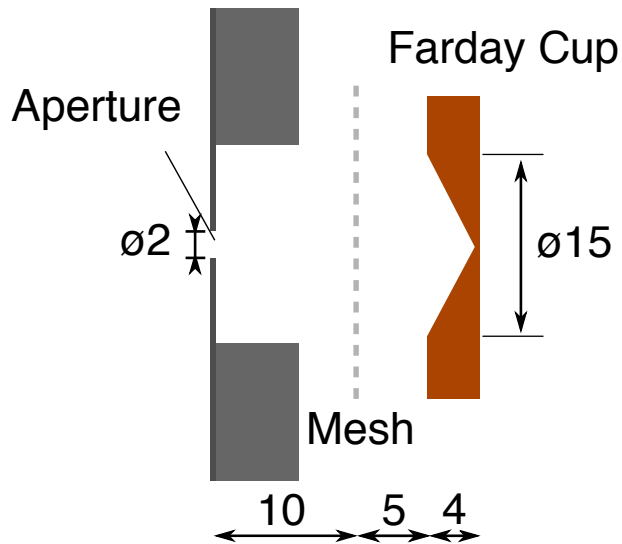


Figure 2.4: Configuration of current density detector.



Figure 2.5: Photo of current density detector covered with stainless shell.

the waveforms.

### 2.3.1 Plasma ion current waveform at a distance from target

Figure 2.6 shows plasma ion current density waveforms at a distance of 690 mm from the target with various strengths of magnetic field. The horizontal axis is the time from the laser shot. The red curve shows a waveform obtained without the magnetic field. Here, we estimate the magnetic Reynolds number  $R_m$  as below. The plasma arrived around 20  $\mu\text{s}$  and thus the typical velocity  $u$  is estimated to be  $\sim 3 \times 10 \text{ mm}/\mu\text{s}$ . Using a scaling law describing the relation that the plasma ion current density is proportional to  $z^{-3}$ , the current density at the solenoid center is estimated to be  $\sim 2 \times 10^2 \text{ mA}/\text{cm}^2$ . From those parameters, the number density of the ions is estimated to be  $\sim 4 \times 10^{11} \text{ cm}^{-3}$  assuming single charge state. The electron temperature is assumed to be  $\sim 1 \text{ eV}$  from the laser power density. Then, the plasma resistivity  $\eta$  is estimated to be  $\sim 6 \times 10^{-2} \Omega \cdot \text{cm}$  using the Spitzer resistivity described by Eq. 1.29. The typical length  $L_t$  is assumed to be the radius of the solenoid. Consequently, we obtain  $R_m = \mu_0 L_t^2 u / \eta \sim 1$  at the interaction region.

As shown in Fig. 2.6, the plasma ion current density was enhanced with the increase in the magnetic field. Furthermore, the waveforms were composed of two peaks. The first peak was around 20  $\mu\text{s}$  regardless of the magnetic flux densities. The other peak appeared later and shifted earlier with increasing the magnetic field. The separation of the peaks



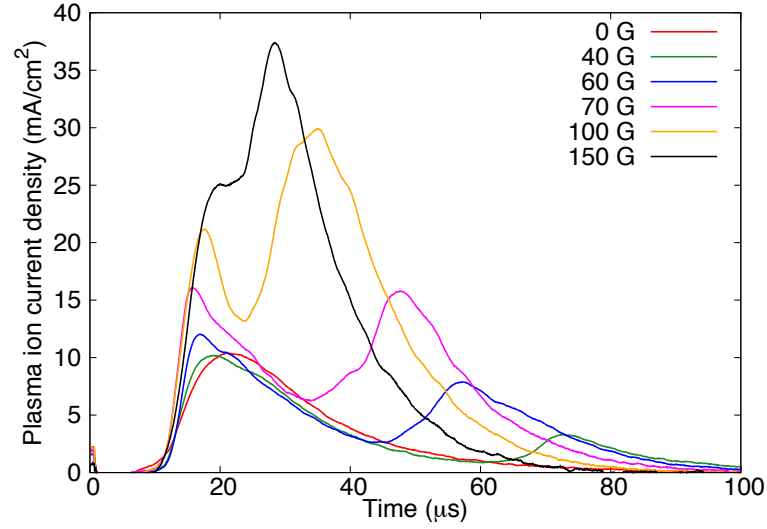


Figure 2.6: Waveforms of plasma ion current densities versus time from laser pulse at a distance of 690 mm from the target, for various magnetic fields at the solenoid center.

indicates that the underlying mechanisms of the current enhancement are different between the head and the tail of the plume.

### 2.3.2 Evolution of current density with distance from target

We scanned the detector along the axis in the longitudinal direction and then obtained plasma ion current density waveforms with applied magnetic field of 40 G as shown in Fig. 2.7. The horizontal axis is the time from the laser irradiation. As shown, both of the fast and the slow peaks were observed at any distances. Arrival time of the fast peak became later and the plasma ion current density decreased with increasing distance. On the other hand, the behavior of the slow peak was more complicated. To investigate the behaviors, we consider a slice model of the plasma plume explained below.

As explained in section 2.1, if it is assumed that the ions evolve from a point source to the free space with a velocity distribution,  $z/t_{peak} = w_{peak}$  is constant and the current density peak  $i_{peak}$  is proportional to  $\propto z^{-3}$ . From the waveforms measured at various  $z$  without magnetic field, we plotted  $t_{peak}$  and  $i_{peak}$  as a function of  $z$  as shown in Fig. 2.8(a) and Fig. 2.8(b), respectively. Fig. 2.8(a) shows the proportional relation between  $z$  and  $t_{peak}$  while Fig. 2.8(b) shows the fitting curve proportional to  $z^{-3}$  was well fitted to the plots of

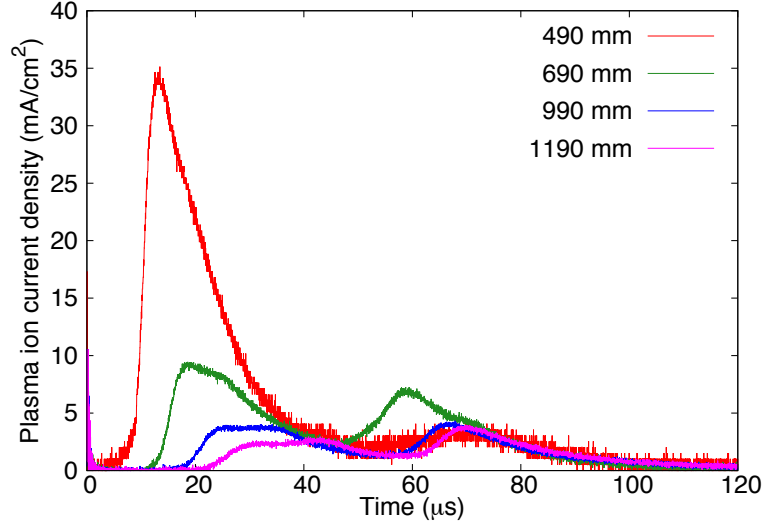


Figure 2.7: Plasma ion current density on the solenoid axis at various distances from the target with magnetic field of 40 G.

$i_{peak}$ . These show that the model and the assumption about the velocity distribution and the point source are valid for our experimental condition.

On the other hand, as shown in Fig. 2.6, the front edge of the waveforms with magnetic field were almost same as those without the field. This means that the longitudinal velocities  $v_z$  of the ions were almost not affected. Therefore, we assume that the  $v_z$  of ions were constant even with the field. Under this assumption, the changes of the plasma ion current density by magnetic field are attributed to the transverse behavior of the plasma.

Under the assumptions, we consider a thin slice of the plasma plume with a constant drift velocity  $v_z = z/t$  as shown in Fig. 2.9. Since an arrival time can be calculated from  $v_z$  and the distance to the detector  $z$ , we can obtain the plasma ion current density of the slice at  $z$  from the plasma ion current density waveform at  $z$ . For example, if the velocity is given to be  $v_z = 11 \text{ mm}/\mu\text{s}$ , the arrival time at a distance of  $z = 690 \text{ mm}$  is calculated to be  $z/v_z = 63 \mu\text{s}$ . Then, from the waveform in Fig. 2.7, it is found that the current density at the time was  $6 \text{ mA}/\text{cm}^2$ . By scanning the detector longitudinally or transversely, we can obtain the plasma ion current density of the slice as a function of  $z$  or transverse distance from the axis. From the current density distribution, we can understand the transverse behavior of the slice. For instance, without magnetic field, the plasma ion current density on the axis

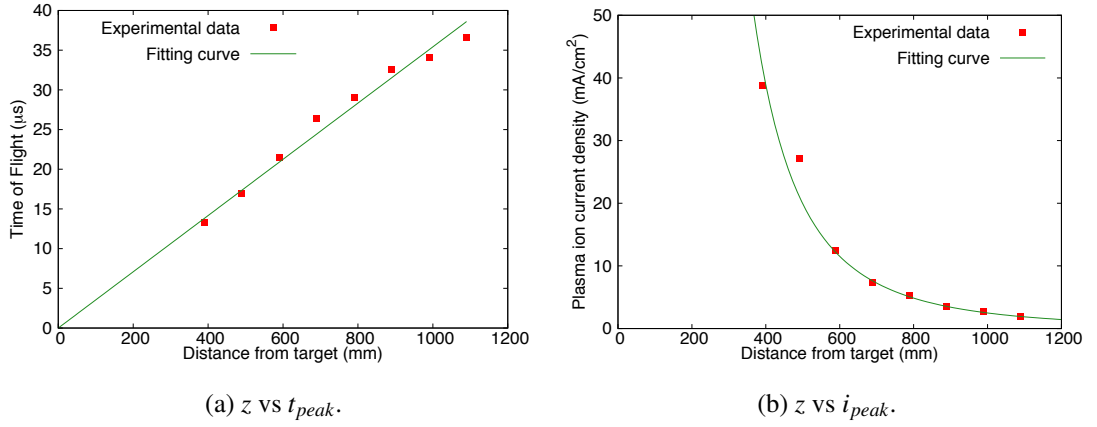


Figure 2.8: Time of flight of current density peak  $t_{peak}$  and the current density  $i_{peak}$  as a function of distance from the target  $z$  without magnetic field.

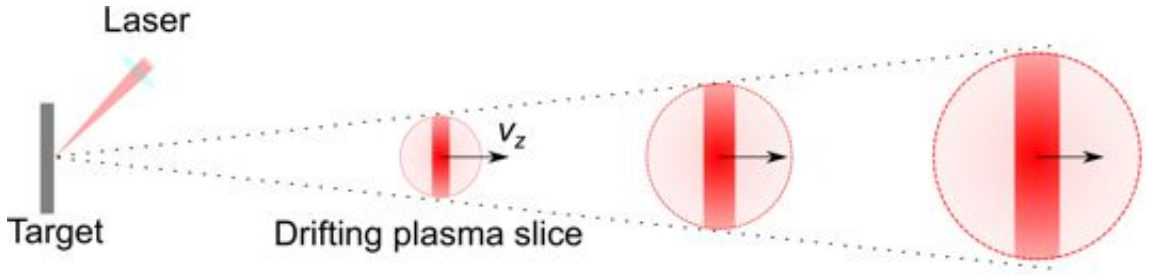


Figure 2.9: Slice model of drifting plasma plume.

are described by  $i(z) \propto z^{-3}g(v_z) = z^{-3}g(v_z) \propto z^{-3}$ . Therefore, if a measured distribution  $i(z)$  are fitted by  $z^{-3}$  well, we can find that the slice spreads three-dimensionally from the target while drifting.

## 2.4 Behavior of tail of plasma plume

Using the slice model, we investigate the behavior of tail of plasma plume. We show longitudinal distributions of plasma ion current density of slices with various velocities and with a strength of the magnetic field. We also show transverse distributions at a distance from the target. From the distributions, we discuss the behavior of the tail. Then, we investigate the dependency of the behavior on the strength of the magnetic field.

### 2.4.1 Longitudinal distributions of current density of slices

We investigate plasma ion current density of four slices with velocities of 10, 11, 12, and 14 mm/ $\mu$ s. Here, Fig. 2.10 is the plasma current density waveforms at 870 mm. With magnetic field of 40 G, a slow peak appeared around 80  $\mu$ s. We calculated the arrival times of the slices, which are shown in the figure. As shown, the plasma ion current density of the slice with 11 mm/ $\mu$ s corresponded to the slow peak while the current densities of the other slices were around the peak. Briefly, the slices were corresponding to the slow peak.

Figure 2.11 shows that the plasma ion current density of the slices on the axis as a function of  $z$ . The red plots show the current densities without magnetic field while the green plots show those with the field. Regardless of  $v_z$ , the current density without magnetic field decreased monotonically and are fitted well by curves proportional to  $z^{-3}$ . This means that the ions emitted three-dimensionally from the laser spot while maintaining the velocity distribution as mentioned above.

Figure 2.11(a) shows that in the presence of the magnetic field, the plasma ion current density of the slice with 10 mm/ $\mu$ s decreased monotonically with increasing  $z$  when  $z$  was less than 600 mm. The current density was almost same as that without magnetic field. On the other hand, when  $z$  was larger than 600 mm, the current density was enhanced and a peak was formed around  $z=800$  mm. Figure 2.11(b) and (c) also show the similar tendency of the slices with 11 and 12 mm/ $\mu$ s while the peak positions became farther as  $v_z$  became larger. Figure 2.11(d) shows the monotonical decrease of the current density with 14 mm/ $\mu$ s. However, the peak was not formed.

The monotonical decreases of the plasma ion current density without enhancement when  $z$  was less than a specific distance mean that the ions near the axis diverged almost without effects of the magnetic field. On the other hand, the current density enhancements mean that the plasma number density near the axis was enhanced by the magnetic field application. Additionally, the density enhancement was largest at the distance where the current density peak formed. These show that the outer plasma gradually concentrating to the axis with increasing distance. These tendencies indicate that the inner plasma of the slice diverges while the outer plasma converges after interacting the magnetic field as illustrated in Fig. 2.12. In this interpretation, the dependency of the peak position on  $v_z$

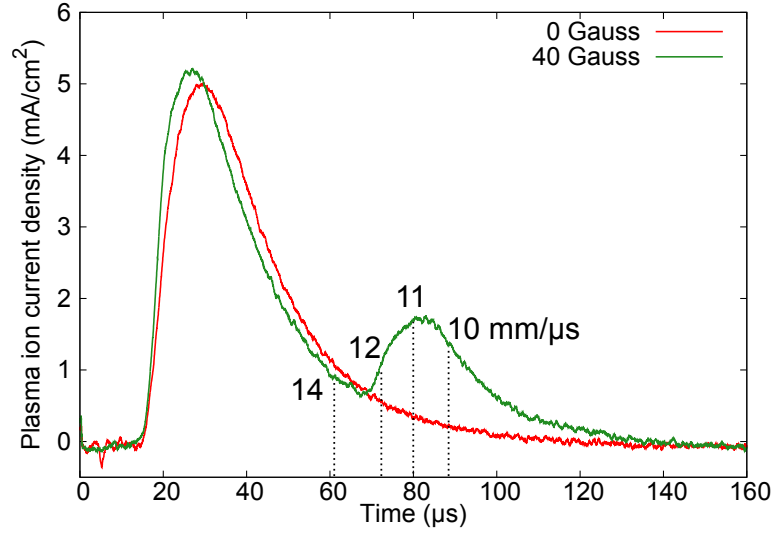


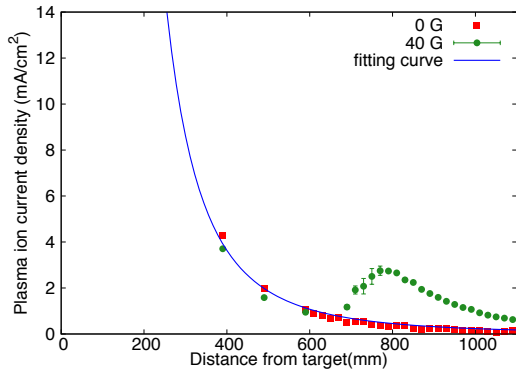
Figure 2.10: Plasma ion current density at a distance of 870 mm.

means that the focal point depends on  $v_z$  as in solenoidal lens as used for charged particle beam transport. The lack of an observed peak for the slice with 14 mm/ $\mu$ s indicates that the focusing point was farther than our scanning range (see Fig. 2.11 (d)).

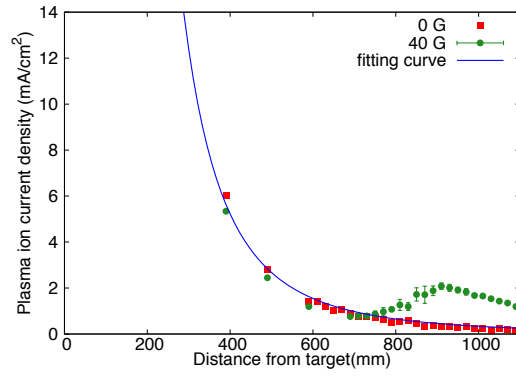
### 2.4.2 Transverse distributions of current density of slices

We scanned the ion probe transversely with the setup shown in Fig.2.1(b) to obtain the transverse distributions of the plasma ion current density for slices at a distance of 870 mm. The slice velocities were 10, 11, 12, and 14 mm/ $\mu$ s. Figures 2.13 show that the plasma ion current densities as a function of the transverse distance. Each plotted point is the average of 3 measured data. For all velocities, the plasma ion current density was almost uniform in the absence of the magnetic field. In the presence of the field, the enhancement of the plasma ion current density was observed. The distribution with 11mm/ $\mu$ s (Fig.2.13(b)) was narrower than those with 10 (Fig.2.13(a)) and 12 mm/ $\mu$ s (Fig.2.13(c)). On the other hand, hollow regions appeared in the distributions in Figs. 2.13 (c) and (d). The region with 14 mm/ $\mu$ s was larger than for 12 mm/ $\mu$ s.

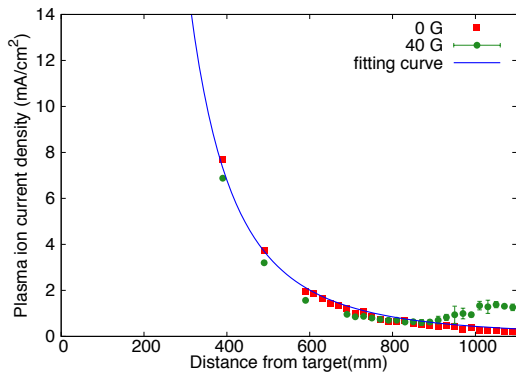
The narrow distributions indicate the convergence of the slice. Moreover, the narrower distribution with 11 mm/ $\mu$ s indicate that the convergent point was closer to the distance of 870 mm than those with 10 and 12 mm/ $\mu$ s. This is consistent with the results of the



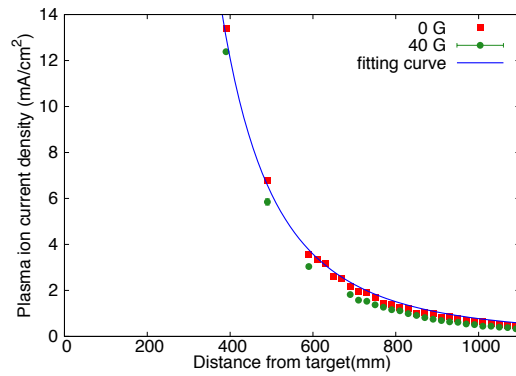
(a) 10 mm/μs.



(b) 11 mm/μs.



(c) 12 mm/μs.



(d) 14 mm/μs.

Figure 2.11: Plasma ion current densities of slices whose velocities are (a) 10, (b) 11, (c) 12, and (d) 14 mm/μs as functions of longitudinal distance (each plots was average of 5 data).

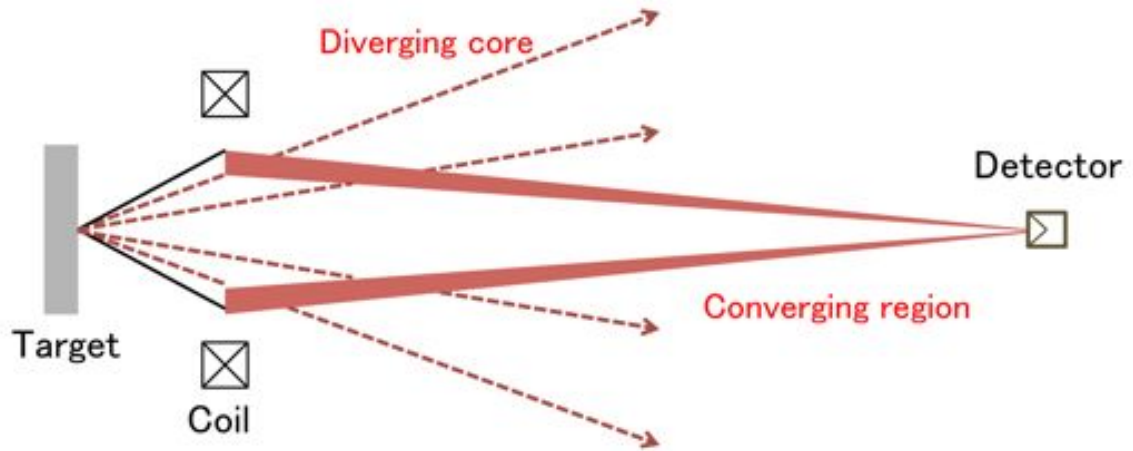


Figure 2.12: Image of the inner diverging core and the outer converging region

longitudinal scan that showed that the the plasma slice with  $11\text{mm}/\mu\text{s}$  converged around  $900\text{ mm}$ , the slice with  $10\text{ mm}/\mu\text{s}$  converged closer, and the slice with  $12\text{ mm}/\mu\text{s}$  converged at a farther point.

The formation of the hollow region in the distribution with  $14\text{ mm}/\mu\text{s}$  can be explained by assuming followings: (1) the inner region of the plasma slice diverged without effects of magnetic field while the outer region converged to a point depending on the velocity as illustrated in Fig. 2.12, and (2) the convergent point is farther than  $870\text{ mm}$ . In that case, at  $870\text{ mm}$ , the converging outer region do not reach the axis while the plasma near the axis consists of only diverging inner region plasma. If so, the plasma ion current density distribution would have the enhanced outer region and the non-enhanced inner region as shown in Fig. 2.13 (d). Then if the convergent point of the slice with  $12\text{ mm}/\mu\text{s}$  was right after  $870\text{ mm}$ , the outer converging plasma reached closer to the center axis than the slice with  $14\text{ mm}/\mu\text{s}$ . This is consistent with the smaller hollow region in Fig. 2.13 (c) than Fig. 2.13 (d). Therefore, the transverse distributions indicate the plasma behavior as illustrated in Fig. 2.12 as well as the results of the longitudinal scan.

From the consistent results of the longitudinal and transverse scan, the behavior of the tail of the plasma plume after the interaction with magnetic field was shown. Namely, the inner region of the plasma plume diverges without effects of magnetic field while the outer region converges to a point depending on the velocity as illustrated in Fig. 2.12.

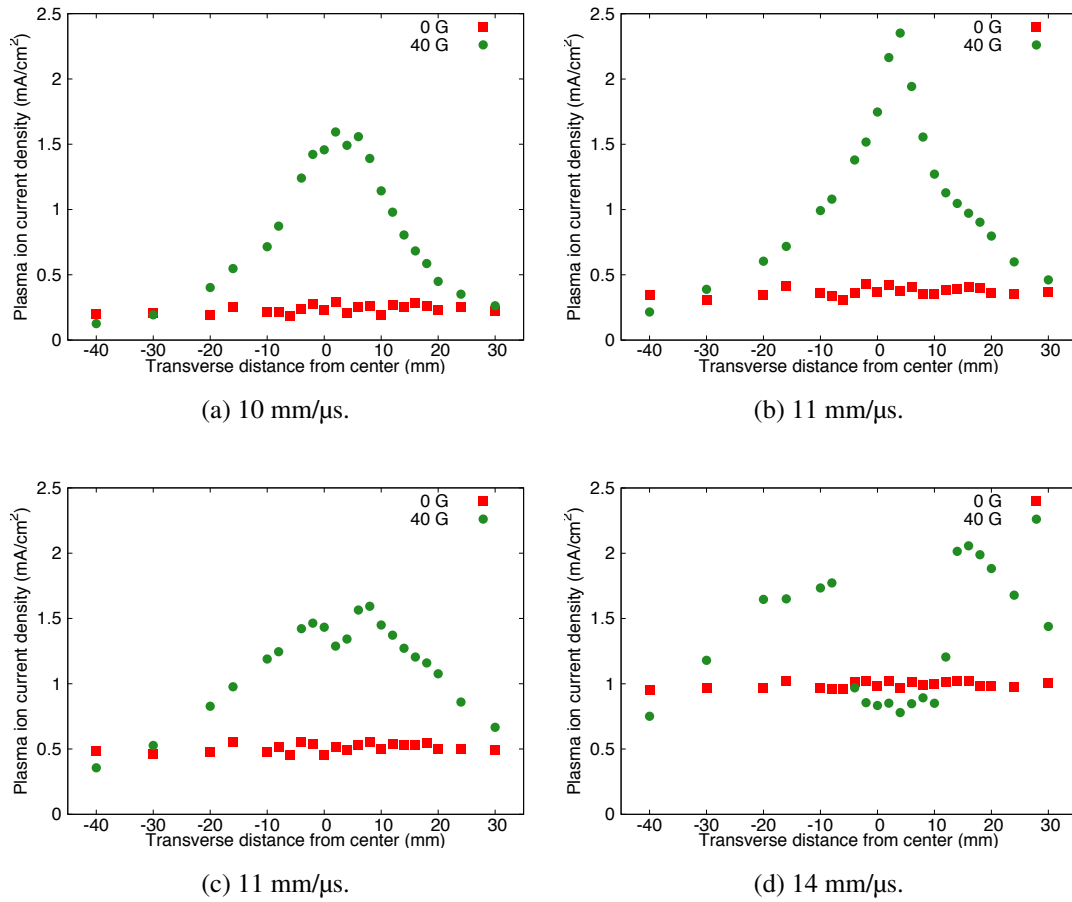


Figure 2.13: Transverse distributions of plasma ion current density for slices whose velocities are (a) 10, (b) 11, (c) 12, and (d) 14 mm/μs.



### 2.4.3 Dependency of plasma dynamics on strength of magnetic field

We measured the plasma ion current density of a slice with 22 mm/ $\mu$ s as a function of longitudinal distance  $z$ . The arrival time of the slice at the distance of 690 mm is estimated to be 30  $\mu$ s. At this time, the slow peak was formed in the plasma ion current density waveform with the magnetic field of 100 G as shown in Fig. 2.6. Namely, the slice consisted of the slow peak.

Figure 2.14 shows the plasma ion current density of the slice with various magnetic field. The red plots show the current density without magnetic field. We can find the current density decreased monotonically. The green plots show that with the magnetic field of 40 G, the current density also decreased monotonically and was almost not enhanced. On the other hand, with 70 and 100 G, enhancement and peak formation were observed after monotonical decrease to specific distances. The peak position became closer to the target with increase in the magnetic field.

The peak formation after the monotonical decrease were similar to the tendencies observed in previous subsections. This shows that the slices also behaves as shown in Fig. 2.12. Moreover, the distance where the peak was formed with the field of 100 G was smaller than that with 70 G. This shows that the convergent point depends on the strength of the field. Therefore, the results in the present and previous subsections show that the outer plasma converges to a point depending on the velocity and the strength of the field like a magnetic lens.

In addition, the peak with the field of 100 G was formed around 690 mm. This means that the outer plasma converged to the point at the distance around 30  $\mu$ s. In this case, the plasma ion current density of the slice should be enhanced more largely than those of other slices at the distance. This is the reason that the slow peak was formed around 30  $\mu$ s in the current density waveform with the field of 100 G as shown in Fig.2.6. Furthermore, the reason of the peak shift with increase in magnetic field is that the velocity of the slice that converges at a detector position changes with the field strength.

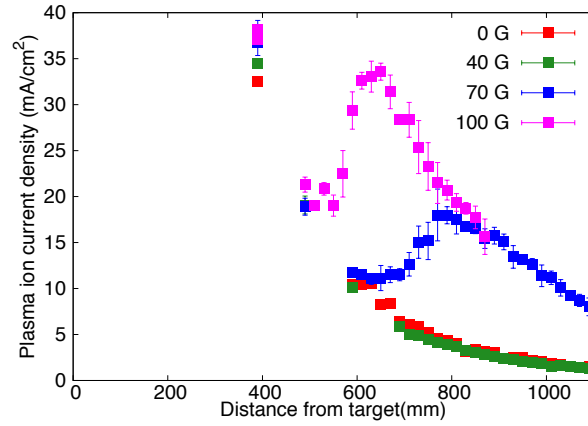


Figure 2.14: Dependence of plasma ion current density on magnetic field for slice with 22 mm/ $\mu$ s .

## 2.5 Behavior of head of plasma plume

In this section, we show the behavior of the head of the plasma plume based on the slice model. We measured plasma ion current density on the axis in a slice with 36 mm/ $\mu$ s as a function of distance from the target  $z$ . The arrival time of the slice at the distance of 690 mm is estimated to be 20  $\mu$ s. Around the time, the fast peak was formed in the plasma ion current density waveform as shown in Fig. 2.6. This means that the slice consisted of the fast peak.

Figure 2.15 shows that the plasma ion current density with various magnetic field. The red plots show the current density without magnetic field while the other curve show those with the field. In contrast to the tail of the plasma plume, peak was not formed and the current density increased monotonically with magnetic field regardless of the distance. This means that the slice did not have the converging region and that the ion density around the axis increased in the magnetic field. In other word, ions with small divergence near the axis was increased by the magnetic field. Therefore, the results show that the inner region of the head of the plasma plume are guided and directed by the magnetic field like a nozzle as illustrated in Fig. 2.16.

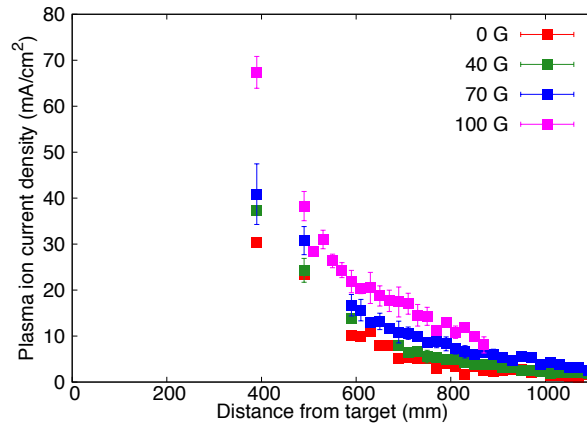


Figure 2.15: Plasma ion current densities of slice with 36 mm/ $\mu$ s with various magnetic field.

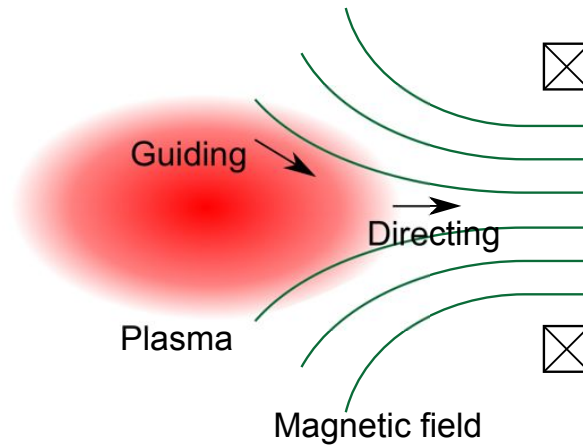


Figure 2.16: Image of guiding of the head of the plasma plume in the initial phase of the plasma interaction.

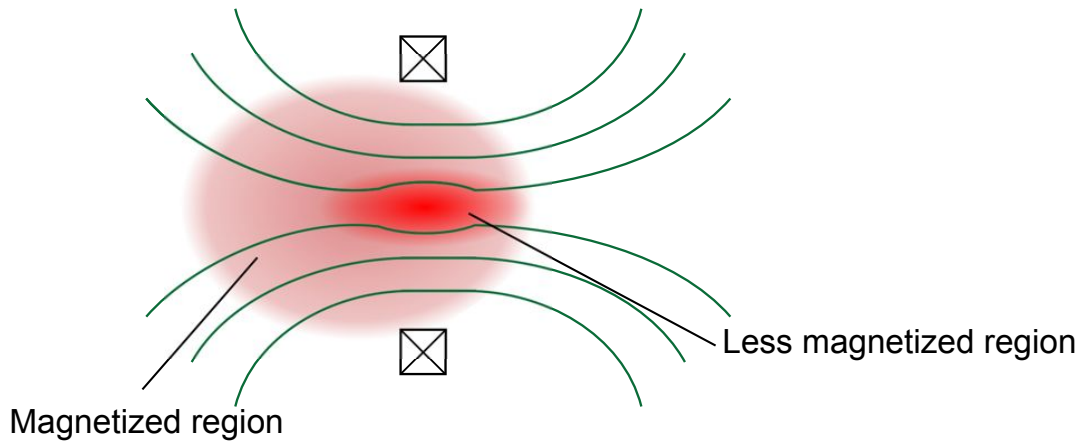


Figure 2.17: Image of the interaction obtained by measurements of plasma ion current density.

## 2.6 Discussion

The results showed that the influence of the magnetic field is different depending on the position of plasma elements in the plume, namely the head and the tail, and also inner and outer regions in the plume. These differences indicate that there are regions with different levels of magnetization in the plasma plume as illustrated in Fig. 2.17. Since the magnetic field gradually diffuses into the plasma plume from the outer region to the inner region, the outer region should be magnetized more strongly than the inner region. On the other hand, because the head is faster than the tail, the ratio of the diffusion time to the characteristic time of the plasma flow of the head is larger. Therefore, the head should exclude more field than the tail. In the dynamic interaction phase, the inner less magnetized plasma should be directed more effectively by the distorted magnetic field while the plasma in the magnetized outer region is bent with a strength depending on the magnetic field and the velocity.

## 2.7 Concluding remarks

In this chapter, effect of axial magnetic field on laser ablation plasma dynamics was discussed. Temporal and spatial distributions of the plasma ion current density were analyzed with a slice model. Firstly, we measured the current density of slices in the tail of the plume

as a function of  $z$ . In presence of the magnetic field, the current density decreased monotonically through a specific distance. That tendency was similar to that without magnetic field. However, the current density increased from the specific distance and then formed a peak. The peak position depended on the ion velocity and the magnetic flux density. Then, the transverse distribution of the current density in a slice was measured. The distribution was narrow around the peak position while a hollow region was observed between the coil and the position. Next, the current density of a slice in the head was measured as a function of  $z$ . In contrast to the result of the tail, the current density enhanced monotonically by the field application without forming a peak.

From the results, we found that the effects of the field are different between the head and the tail, and also the inner and the outer regions of the plume. Namely, the outer region is converged to a point depending on the longitudinal velocity and the magnetic flux density like a magnetic lens. On the other hand, the inner region of the head is guided and directed like a magnetic nozzle while the inner region of the tail is not affected. These differences indicate a progressive magnetization in the plume.



## Chapter 3

# Response of Axial Magnetic Field against Plasma Plume Injection

The results shown in chapter 2 indicated that when laser ablation plasma is injected into axial magnetic field, the field would make an evolving structure within the plasma plume. In the present chapter, we discuss the response of magnetic field against the plasma injection with  $R_m \sim 1$ . The field evolution is measured with a magnetic probe.

We show a waveform of plasma ion current density waveform to estimate interaction parameters and then the temporal and spatial distributions of the magnetic field. From the distribution, diamagnetic current density distribution is estimated. Then, we discuss the relation between the response and the plasma dynamics.

### 3.1 Experimental setup for measurement of diamagnetic field

Figure 3.1 is the experimental setup for the measurement of the diamagnetic field induced by the plasma injection. An iron target was placed in a chamber evacuated to  $4 \times 10^{-4}$  Pa. The laser specification and the irradiation condition are shown in Table 3.1. The target was moved slowly to avoid seriously damaging the target surface. To limit the solid angle of the plume, a disk with a 14-mm diameter aperture was placed at a distance of

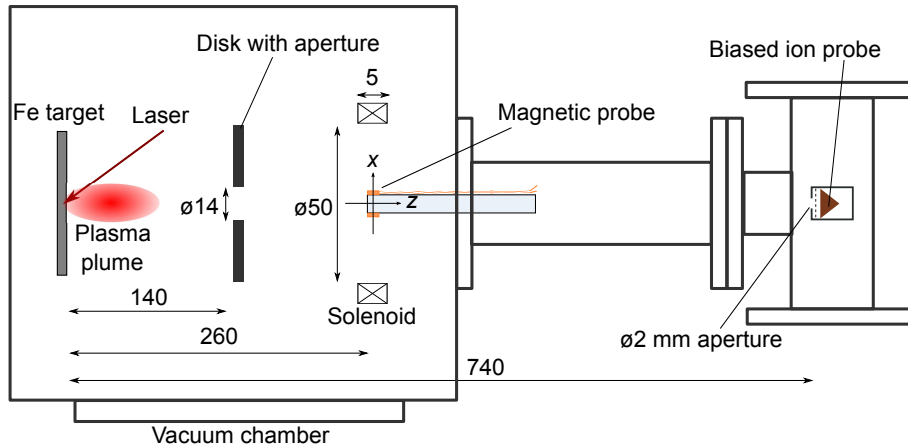


Figure 3.1: Experimental setup for measurement of magnetic field.

Table 3.1: Laser conditions for plasma ion current density measurement

Laser Model	THALES SAGA 230
Laser type	Nd:YAG Laser
Wave length	1064 nm
Pulse width (FWHM)	6 ns
Spot size	0.2 cm <sup>2</sup>
Laser energy on target	630 mJ
Power density	$4 \times 10^8$ W/cm <sup>2</sup>

140 mm from the target. The limitation of the plume region is important when we estimate diamagnetic current.

A short solenoid with 50 mm in diameter and 5 mm in length was placed at a distance of 260 mm. The solenoid was made of 14 times wound copper wire with 2 layers. The solenoid was covered by a grounded thin aluminum sheets for electrical shielding with axial slits to prevent the eddy current induced by rising magnetic field of the solenoid. We energized the solenoid using a DC power supply (LAMBDA, EMS 80-60). The longitudinal component of the magnetic field  $B_z$  was calculated by OPERA. Here,  $x$  and  $z$  are transverse and longitudinal components of a cartesian coordinate in which the origin is the solenoidal center as shown in Fig. 3.1. Figure 3.2 (a) and (b) show the  $B_z$  on  $z$  and  $x$  axes generated by 1 A, respectively. In this experiment,  $B_z$  was 65 G at the center.

Since the target material, the laser power density, and the solenoid dimensions are al-

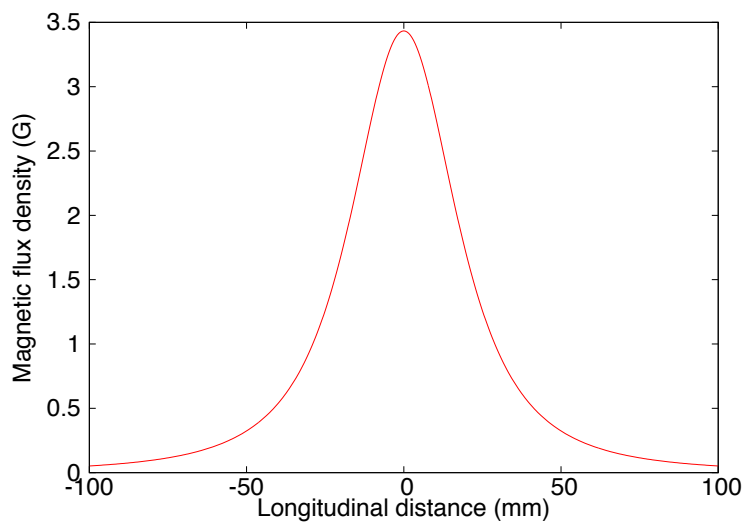
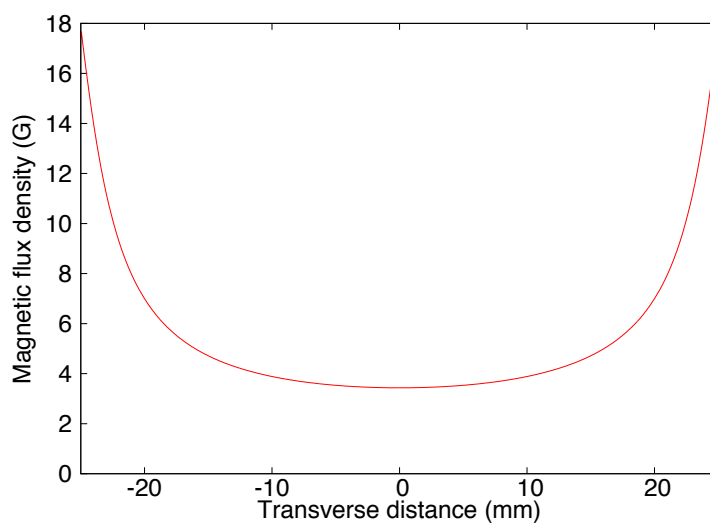


most the same as those in chapter 2,  $R_m$  in this experimental condition is also estimated to be around 1.

We measured the plasma ion current density with a detector at a distance of 740 mm from the target. The configuration of the detector was the same as the detector shown in Fig. 2.4. The bias voltage was -180 V to obtain stable signal.

A magnetic probe was used to measure the magnetic field change induced by the plasma injection. A schematic diagram of the probe is shown in Fig.3.3, in which a pickup coil was attached to the front edge. The diameter and the length were 6.4 (1/4 inch) and 2 mm, respectively. A 0.16-mm-diameter copper wire was wound 20 times on an acrylic rod with 2 layers. The cables connected to the pickup coil were twisted and then connected to two 50  $\Omega$  BNC cables and the terminal resistance of 50  $\Omega$ . When the magnetic flux through the pickup coil varies temporarily, a difference of the voltages is induced between both ends under the Faraday's law of induction. We installed the probe in the solenoid as the pickup coil was perpendicular to  $z$  direction. We measured both voltages, and then integrated the differential to obtain the varying magnetic flux. By averaging the flux in the cross section of the pickup coil, the variation of  $B_z$ , which we denote as  $\Delta B_z$ , was obtained. The reason of measuring both voltages  $V_1$  and  $V_2$  is to remove the common mode noise caused by the floating potential of the plasma [49, 50]. The probes are biased up by the plasma potential through the stray capacitance of the insulator covering the coil wire. Because the noises on both ends are same, we can eliminate them by using the differential,  $V_1 - V_2$ .

Here, to check the probe performance, we estimated the inductance of the pickup coil. We assume that the magnetic field generated by the coil current  $I$  is uniform and described by  $\mu_0 IN/2a$ , where  $a$  is the coil radius and  $N$  is the winding number. In this case, the inductance  $L$  is  $\sim \mu_0 \pi a N^2 / 2$ . Therefore,  $L$  is estimated to be  $\sim 3 \mu\text{H}$ . Because the plasma plume passes through the solenoid within several tens of micro seconds as shown later, the characteristic frequency of the varying magnetic field is expected to be  $\sim 0.1 \text{ MHz}$ . Consequently, the impedance of the pickup coil is estimated to be  $L\omega \sim 2 \Omega$ . Because the terminal resistance is 50  $\Omega$ , the accuracy of the measurement is expected to be more than 90 %. Then, to check the probe performance experimentally, we measured a magnetic field generated by the solenoid with a pulse current changing with time scale ( $\sim 10 \mu\text{s}$ ) of the plasma. We compared the magnetic field and the field estimated from the current measured

(a)  $B_z$  on  $z$  axis.(b)  $B_z$  on  $x$  axis.Figure 3.2: Calculated longitudinal magnetic field  $B_z$  on  $z$  and  $x$  axes.

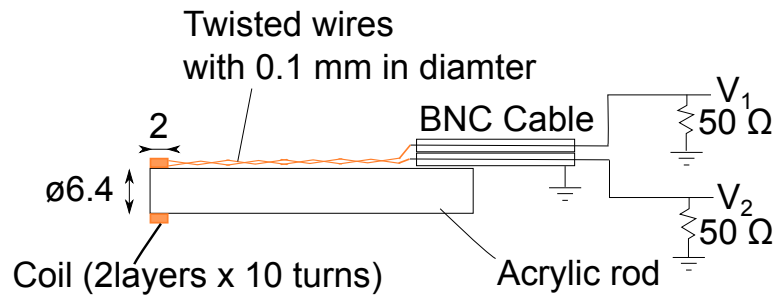


Figure 3.3: Schematic diagram of magnetic probe.

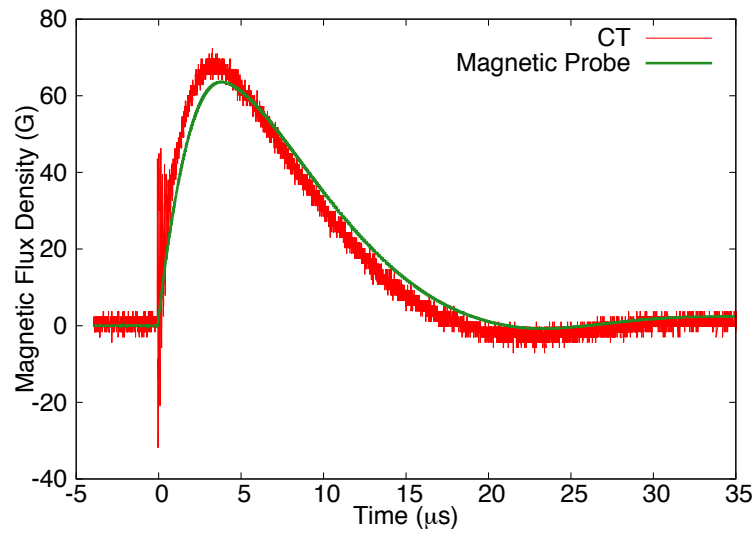


Figure 3.4: Magnetic field measured by the magnetic probe and calculated from the solenoid current measured by a current transformer (CT).

by a current transformer. The fields shown in Fig. 3.4 were similar enough to discuss the temporal variation of the magnetic field.

## 3.2 Plasma ion current density measurement

Figure 3.5 shows the plasma ion current density at a distance of 740 mm as a function of the time from the laser shot. The red and the green curves show the waveforms obtained in absence and presence of the magnetic field, respectively. As shown, the plasma ion current density of the head of the plume was enhanced. The enhancement means that the head was directed as shown in the chapter 2. On the other hand, the slow peak observed in the

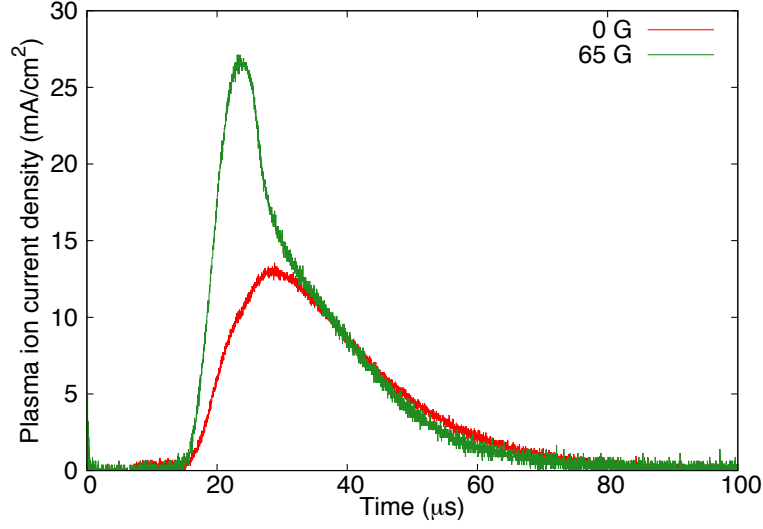


Figure 3.5: Plasma ion current density as a function of time at a distance of 740 mm.

measurement in chapter 2 did not appear. The reason may be the limitation of the plume radius by the aperture between the target and the solenoid. The small signal around 10  $\mu\text{s}$  was caused by lighter contaminant species such as carbon and oxygen.

From the waveform without magnetic field, the plasma ion current density at the solenoid center can be estimated using the scaling laws showing that the time of flight is proportional to the distance and the current density is proportional to  $z^{-3}$ . Figure 3.6 shows the estimated current density waveform. The peak is around 10  $\mu\text{s}$ . Therefore,  $\Delta B_z$  is expected to be detected around that time.

### 3.3 Response of axial magnetic field

Figure 3.7 shows typical signals of one end of the magnetic probe. The figure includes three signals taken at the same conditions. The spike signals right after 0  $\mu\text{s}$  were caused by the laser breakdown. The signals around 10  $\mu\text{s}$  were induced by the variation of  $B_z$  as expected from the plasma ion current density in Fig. 3.6. The signals show the reproducibility enough to discuss the variation of  $B_z$ . The spiky signal appearing every 20  $\mu\text{s}$  was caused by switching noises in the DC power supply. To eliminate the noise, we averaged 10 waveforms. The red curve in Fig. 3.8 is the averaged waveform. The green curve is

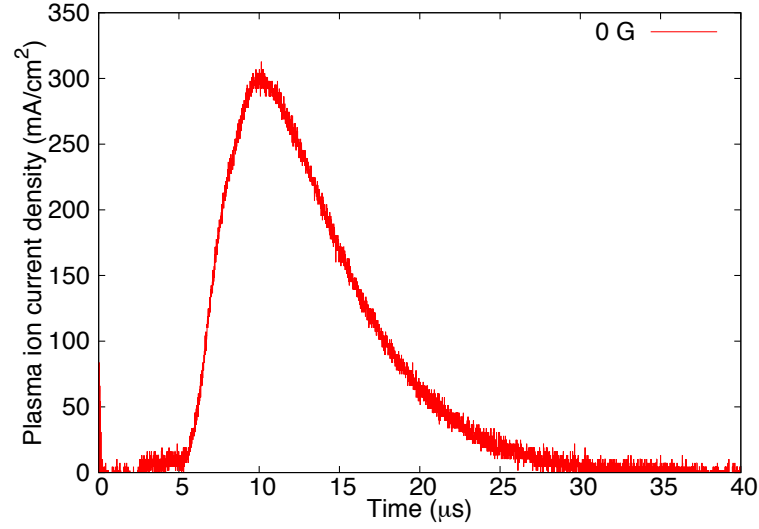


Figure 3.6: Estimated plasma ion current density at center of solenoid.

the averaged signal of the other probe end. The signals with the same polarity around  $3 \mu\text{s}$  were caused by the plasma potential. The opposite signals around  $10 \mu\text{s}$  were induced by the variation of the magnetic field. After  $20 \mu\text{s}$ , no signal was observed because the plasma had passed through the solenoid.

By integrating the differential of the probe signals,  $\Delta B_z$  was obtained as a function of time. The red curve in Fig. 3.9 shows  $\Delta B_z$  at the solenoid center. As shown,  $\Delta B_z$  was negative around  $8 \mu\text{s}$ . The negative value means that the magnetic field decreased. The peak value was  $-0.44 \text{ G}$ . This was  $0.67 \%$  of the external field at the same point. The gray curve is the estimated plasma ion current density at the solenoid center that is the same as the waveform shown in Fig. 3.6. The plasma ion current density peak is around  $10 \mu\text{s}$  while the peak of  $\Delta B_z$  was around  $8 \mu\text{s}$ . This means that the magnetic field decreased more largely when the head of the plasma plume passed through the center. The decrease means that the field was excluded from the plasma plume. Therefore, the results show that the field was excluded more largely by the plume head. On the other hand,  $\Delta B_z$  decreased around  $4 \mu\text{s}$  while the plasma ion current density had the small peak around  $4 \mu\text{s}$ . These were caused by the plasma composed of lighter species.

We scanned the magnetic probe longitudinally and transversely to obtain spatial distribution of  $\Delta B_z$ . Figure 3.10(a) shows  $\Delta B_z$  as a function of time measured on  $z$  axis at  $z = -20$ ,

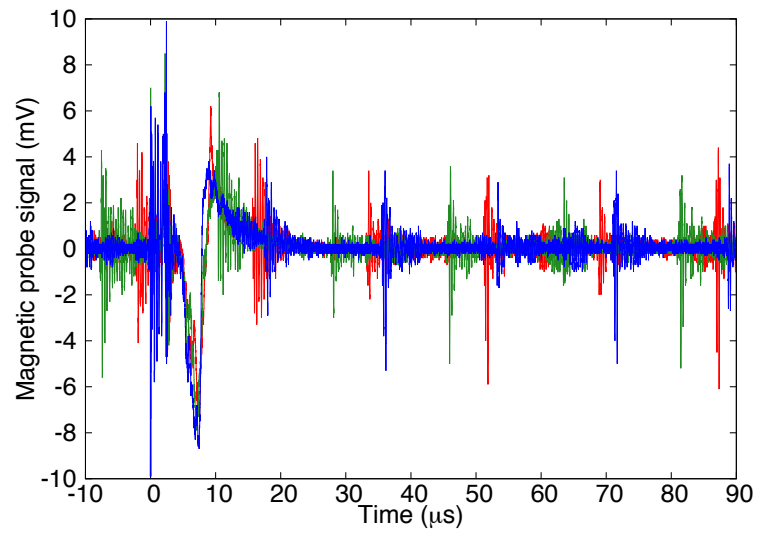


Figure 3.7: Three magnetic probe signals as a function of time taken at same condition.

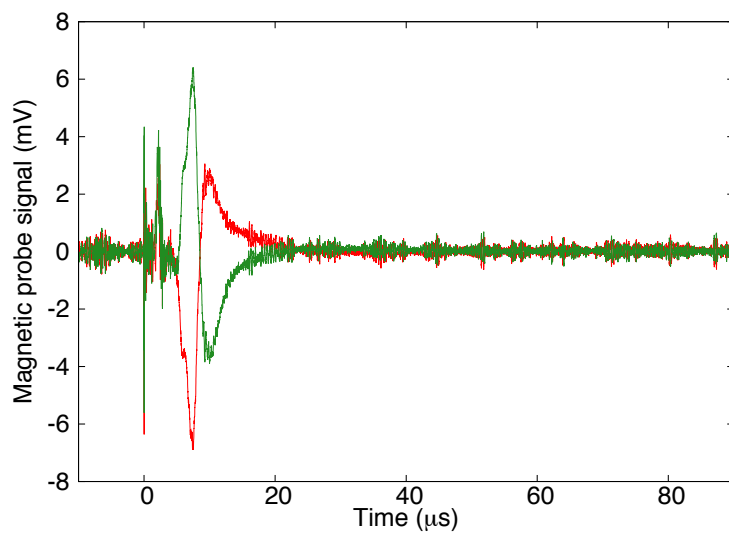


Figure 3.8: Averaged magnetic probe signals of both ends.

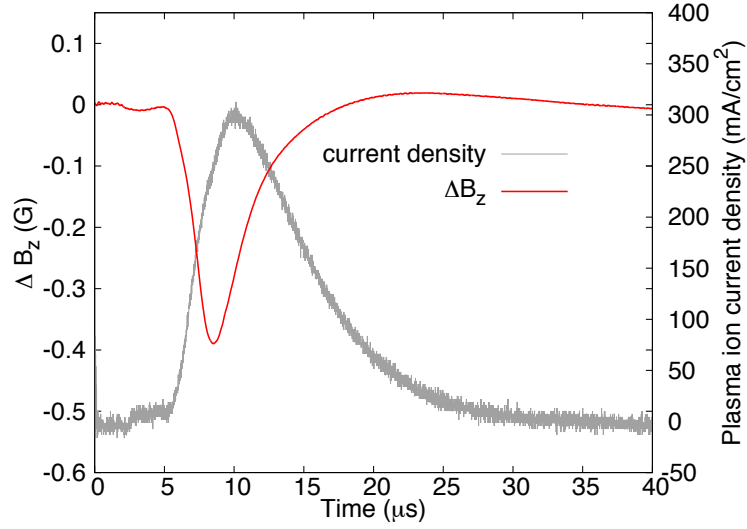


Figure 3.9:  $\Delta B_z$  and plasma ion current density as a function of time at the center.

0, 20, and 50 mm from the center. With increasing  $z$ , the peak of  $\Delta B_z$  waveform became larger from negative to positive. In addition, the peak time shifted to later. Figure 3.10(b) shows that  $\Delta B_z$  as a function of time measured on  $x$  at  $x=0, 4, 8$ , and 12 mm. With increasing  $x$ , the peak of  $\Delta B_z$  waveform became larger and was almost zero at 12 mm. From those waveforms and other ones measured at other positions, we obtained spatial distribution of  $\Delta B_z$  at various time.

Figure 3.11(a) shows  $\Delta B_z$  on  $z$  axis as a function of  $z$  at time of 6, 8, 10, and 14  $\mu$ s after the laser pulse. At 6  $\mu$ s,  $\Delta B_z$  was negative from -60 to 0 mm and smallest around -20 mm. As shown,  $\Delta B_z$  did not change over 0 mm. This is because that the front edge of the plume was around 0 mm at this early measurement time as shown in the plasma current density waveform in Fig. 3.6. At 8  $\mu$ s,  $\Delta B_z$  around -20 mm became smaller. The decrease was 2 % of the external magnetic field at the same position. On the other hand,  $\Delta B_z$  around 50 mm became positive. The absolute value of  $\Delta B_z$  around -20 mm was larger than that around 50 mm.  $\Delta B_z$  changed from negative to positive around 30 mm. Then, with increase in time from 8  $\mu$ s to 14  $\mu$ s,  $\Delta B_z$  around -20 mm became larger as shown in blue and pink plots. On the other hand,  $\Delta B_z$  around 50 mm became larger. Consequently, the difference of the absolute values of negative and positive  $\Delta B_z$  became smaller with time. In addition, the zero point where  $\Delta B_z$  changed from negative to positive became closer to the solenoid

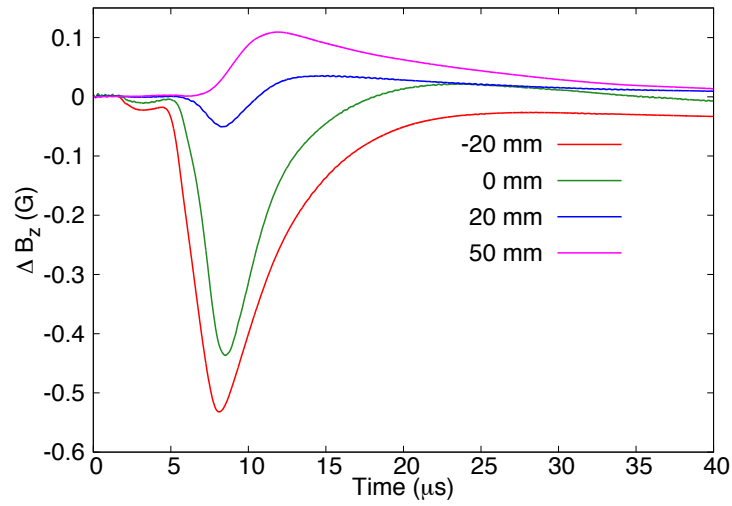
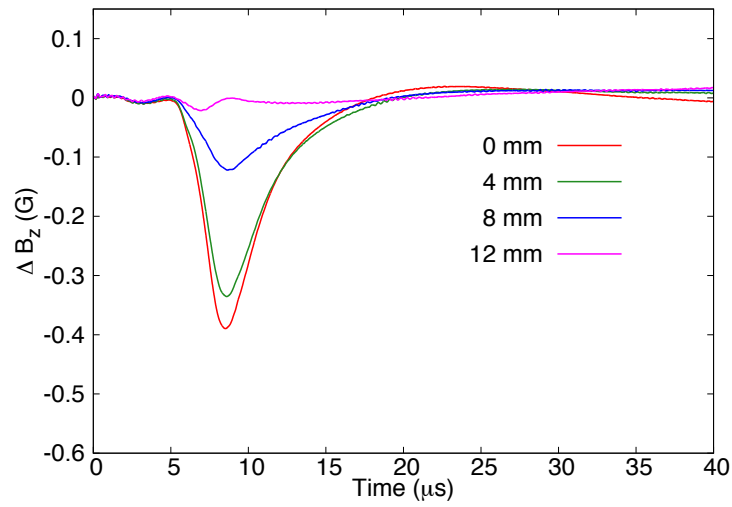
(a)  $\Delta B_z$  on  $z$  axis at various longitudinal distances.(b)  $\Delta B_z$  on  $x$  axis at various transverse distances.

Figure 3.10:  $\Delta B_z$  as a function of time measured at various longitudinal and transverse distances.



center gradually.

The longitudinal distributions of  $\Delta B_z$  showed that the magnetic field decreased at the upper stream of the solenoid and increased at the downstream. The absolute value of the decrease was larger than that of the increase. In addition, the change of  $\Delta B_z$  from negative to positive occurred at the downstream from the solenoid center. These show that the magnetic field is distorted asymmetrically with respect to the solenoid midplane by the exclusion from the plasma plume and the drag by the plume as illustrated in Fig. 3.12. Namely, the magnetic field is excluded at the upper stream, diffuses into the plasma gradually around the center, and then is dragged by the plasma due to the diamagnetic effect.

Additionally, the exclusion and the field asymmetry at 8  $\mu\text{s}$  were largest and then became smaller gradually. This shows that the magnetic field is excluded more largely by the head of the plasma plume than the tail.

Figure 3.11(b) shows  $\Delta B_z$  as a function of  $x$  at time of 6, 8, 10, and 14  $\mu\text{s}$ . For all the time,  $\Delta B_z$  was negative from  $x = 0$  to 13 mm and smallest at 0 mm. This shows that the magnetic field diffused from the outside of the plasma plume. The magnetic field decreased most largely at 8  $\mu\text{s}$ , and then gradually restored. On the other hand, the field was almost nothing in  $x > 13$  mm. This is because that the plasma was not in  $x > 13$  mm due to the aperture disk placed between the target and the solenoid.

In longitudinal and transverse distributions of  $\Delta B_z$ , the decrease of the magnetic field at 6  $\mu\text{s}$  was smaller than that at 8  $\mu\text{s}$ . This is because that the radius around the front edge of the plume are smaller.

From both distributions, we found that the magnetic field evolves asymmetrically within the plume, and the head near the axis distorts the field more largely.

### 3.4 Estimation of diamagnetic current density distribution

The variation of magnetic field  $\Delta \mathbf{B}$  is induced by a diamagnetic current  $\mathbf{j}$ . In non relativistic approximation, these are connected by the equation  $\nabla \times \Delta \mathbf{B} = \mu_0 \mathbf{j}$ . Therefore,  $\mathbf{j}$  can be estimated from the equation. From a two dimensional map of  $\mathbf{j}$ , we can image the

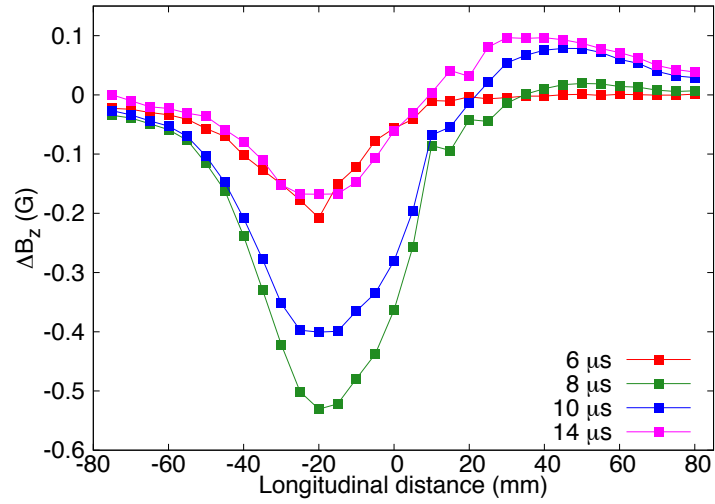
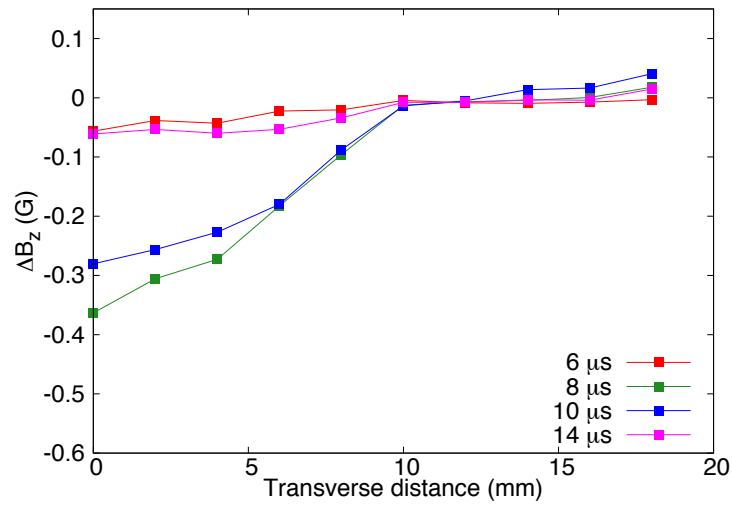
(a)  $\Delta B_z$  on  $z$  axis.(b)  $\Delta B_z$  on  $x$  axis.

Figure 3.11:  $\Delta B_z$  as functions of longitudinal and transverse distance at 6, 8, 10, and 14  $\mu\text{s}$  after the laser pulse.

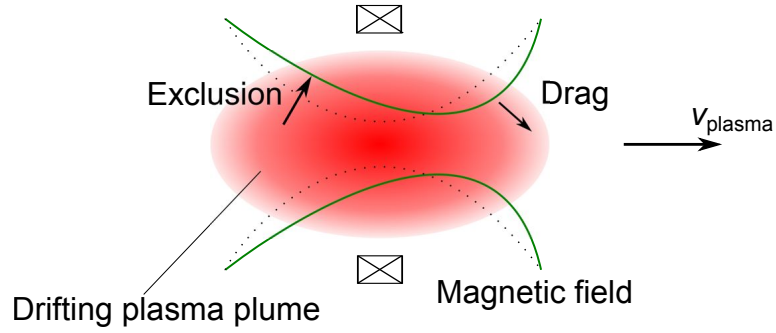


Figure 3.12: Image of exclusion and drag of magnetic field by plasma plume.

time-space evolutions of the diamagnetic effect and the force on the plume easily. In this chapter, we estimate  $j$  by reconstructing the measured  $\Delta B_z$  to discuss the response of the magnetic field. In the following sections, we will consider only the induced B-field; hence we will denote  $\Delta B$  as just  $B$  for simplicity.

### 3.4.1 Reconstruction method

The basic equations are

$$\nabla \times \mathbf{B} = \mu_0 \mathbf{j}, \quad (3.1)$$

$$\nabla \cdot \mathbf{B} = 0. \quad (3.2)$$

From the experimental setup, we can assume axial symmetry. We think a cylindrical coordinate system in which the origin is the solenoid center, and  $z$  is along the axis as in the previous sections. In this case,  $j$  had only an azimuthal component  $j_\theta$  because a closed current could exist only as azimuthal loop due to the axial symmetry and the finite volume of the plasma plume. In an axially symmetric system, the magnetic vector potential  $\mathbf{A}$  has only an azimuthal component  $A_\theta$ . Therefore, the equations are reduced to the following equation,

$$-\frac{\partial^2 A_\theta}{\partial z^2} - \frac{\partial^2 A_\theta}{\partial r^2} - \frac{1}{r} \frac{\partial A_\theta}{\partial r} + \frac{A_\theta}{r^2} = \mu_0 j_\theta. \quad (3.3)$$

If we assume the form of  $j_\theta$ , we can calculate longitudinal magnetic flux density  $B_{cal}$  by solving the equation. By adjusting the form of  $j_\theta$ , the calculated  $B_{cal}$  can be fitted to the measured longitudinal magnetic flux density  $B_{exp}$ . We reconstructed  $j_\theta$  using this method.

The form of  $j_\theta(r, z, t)$  was assumed to be a linear combination of functions  $F_n(r)$ ,  $G_m(z)$ . Namely,

$$\begin{aligned} j_\theta(r, z, t) &= \sum_{n,m} c_{n,m}(t) i_{n,m}(r, z), \\ i_{n,m}(r, z) &= F_n(r) G_m(z), \end{aligned} \quad (3.4)$$

where  $n$  and  $m$  are natural numbers.  $F_n(r)$ ,  $G_m(z)$  were assumed as follows:

$$F_n(r) = J_1(v_n r/R); (r < R = 25 \text{ mm}), \quad (3.5)$$

$$= 0; (r > R), \quad (3.6)$$

$$G_m(z) = \sin\{(m\pi/2)(z/L + 1)\}; (|z| < L = 100 \text{ mm}), \quad (3.7)$$

$$= 0; (|z| > L). \quad (3.8)$$

$J_1(x)$  is the Bessel function of the first kind for first order and  $v_n$  is  $n$ -th zero of the function.  $R$  was assumed to be 25 mm because the measured magnetic field was 0 around 25 mm as shown in Fig. 3.11(b). Values of  $n$  were 1, 2 or 3.  $L$  was assumed to be 100 mm because the magnetic field was expected to be almost 0 in  $|z| > 100$  mm from the measured magnetic field distribution shown in Fig. 3.11(a).  $m$  was an integer less than 13. By substituting the Equations for Eq. 3.3 and solving Eq. 3.3, we obtained the longitudinal magnetic flux density described by

$$B_{cal} = \sum_{n,m} c_{n,m} b_{cal,(n,m)}. \quad (3.9)$$

Each  $b_{cal,(n,m)}$  was calculated from each  $i_{n,m}$ . Then we fitted the  $B_{cal}$  to the measured longitudinal magnetic flux density  $B_{exp}$  by adjusting  $c_{n,m}$ .

Equation 3.3 was solved by the finite-difference methods. The difference equation

assuming a uniform spatial discretization grid separated by a lattice spacing  $h$  is

$$\begin{aligned} c_l^2 A_{k+1,l} + c_l^2 A_{k-1,l} + (c_k^2 + \frac{c_l}{2}) A_{k,l+1} \\ + (c_l^2 - \frac{c_l}{2}) A_{k,l-1} - (4c_l^2 + 1) A_{k,l} + \mu_0 j_{k,l} r_l^2 = 0, \end{aligned} \quad (3.10)$$

where  $k = 0, 1, \dots, K$ ,  $l = 0, 1, \dots, L$ ,  $z_k = hk$  and  $r_l = hl$  are points of the grid,  $c_l = r_l/h$ ,  $A_{k,l} = A(z_k, r_l)$ ,  $j_{k,l} = j_\theta(z_k, r_l)$ . We solved the equation by iterating the recursion,

$$\begin{aligned} A_{k,l}^{t+1} &= A_{k,l}^t + \frac{h^2}{7.8} \Delta_{k,l}^t, \\ \Delta_{k,l}^t &= (c_l^2 A_{k+1,l}^t + c_l^2 A_{k-1,l}^t + (c_k^2 + \frac{c_l}{2}) A_{k,l+1}^t \\ &\quad + (c_l^2 - \frac{c_l}{2}) A_{k,l-1}^t - (4c_l^2 + 1) A_{k,l}^t + \mu_0 j_{k,l} r_l^2). \end{aligned} \quad (3.11)$$

From the calculated potential, longitudinal magnetic flux density  $B_z(z_l, r_l)$  was calculated by

$$B_z(z_l, r_l) = \frac{r_{l+1} A_{k,j+1} - r_{l-1} A_{k,j-1}}{2r_j h}; (r > 0), \quad (3.12)$$

$$= \frac{2A_{k,1}}{h}; (r = 0). \quad (3.13)$$

To calculate  $b_{cal,(n,m)}$ , we solved Eq. 3.11 for each  $i_{n,m}(r, z)$ . The calculation region was  $0 < z < 300$  mm and  $0 < r < 300$  mm and the mesh numbers were  $K = 400$  and  $L = 400$ . The boundary condition for the vector potential was that  $A_\theta = 0$  on  $r = 0, 300$  and  $z = 300$ . In addition, when  $i_{n,m}(r, z)$  was an odd function,  $A_\theta = 0$  at  $z = 0$ , or when  $i_{n,m}(r, z)$  was an even function, the Neumann boundary condition was set at  $z = 0$ . We finished the iteration when  $\max\{|\Delta_{k,l}^t|\} < 1 \times 10^{-13}$ . From the calculated  $A_\theta$ , we calculated  $b_{cal,(n,m)}$  in the region where  $z > 0$ . Then, we also calculated  $b_{cal,(n,m)}$  in  $z < 0$  using the asymmetry with respect to  $r$  axis. Thus, we obtained  $b_{cal,(n,m)}$ .

Using  $b_{cal,(n,m)}$  and  $B_{exp}$ , we adjusted  $c_{n,m}$  by means of the least square method. Namely, we minimized the function,

$$\varepsilon(c_{n,m}) = \sum_s r_s \{B_{exp}(z_s, r_s) - \sum_{n,m} c_{n,m} b_{cal,(n,m)}(z_s, r_s)\}^2, \quad (3.14)$$

where  $(z_s, r_s)$  are coordinates of the measurement points. Here, we added points at  $z=-100$ ,  $-87.5$ ,  $90$ , and  $100$  mm on  $z$  axis to  $B_{exp}$  artificially. Namely, we assumed  $B_{exp}=0$  at  $z=-100$  and  $100$  mm, and then assumed  $B_{exp}$  at  $z=-87.5$  and  $90$  mm by linear interpolation. Then we adjusted  $c_{n,m}$  and obtained  $j_\theta(z, r, t)$ .

Figure 3.13(a) shows the calculated and the measured  $B_z$  on  $z$  axis as a function of  $z$ , and Fig. 3.13(b) shows those on the solenoid midplane as a function of  $r$  at  $10 \mu s$ . The figures show that the calculated  $B_z$  was well fitted. The calculated  $B_z$  around  $-30$  mm in Fig. 3.13(a) and around  $0$  mm in Fig. 3.13(b) were smaller than the measured  $B_z$ . This may be because that the order of the  $J_1(v_n r/R)$  in Eq. 3.6 (i.e.,  $n=3$ ) were not enough to fit to the sharp distribution around  $z = -30$  and  $r = 0$  mm. Therefore,  $j_\theta$  around there would be around 30 % smaller than the accurate value. Even so, the calculated  $B_z$  clearly shows an asymmetry with respect to the  $r$  axis as shown in Fig. 3.13(a). Hence, this is enough to support the diamagnetic effect discussed in the previous section.

### 3.4.2 Estimated current density distributions

Figure 3.14 shows the two dimensional color maps of the estimated  $j_\theta$  as functions of  $r$  and  $z$  at times of (a) 6, (b) 8, (c) 10, (d) 12, (e) 14, and (f)  $16 \mu s$ , respectively. At  $6 \mu s$ , a negative  $j_\theta$  was induced around  $z=-20$  mm and  $r=5$  mm.  $j_\theta$  did not exist over  $z=0$  mm because the front edge of the plasma plume was around there. At  $8 \mu s$ , the negative  $j_\theta$  around  $z=-20$  mm and  $r=5$  mm became smaller. In radial direction, the negative  $j_\theta$  was smallest around  $r=5$  mm and gradually became larger to zero in  $r > 5$  mm. A positive  $j_\theta$  was induced around  $z=40$  mm. The absolute value of the positive  $j_\theta$  was smaller than that of the negative one. In addition, the boundary where  $j_\theta$  changed from negative to positive was around  $z = 20$  mm. After that, with increase in time from 8 to  $16 \mu s$ , the negative  $j_\theta$  became larger as well as the positive one. Consequently, the difference of the negative and positive current became smaller. In addition, the boundary from negative to positive became closer to  $z = 0$  mm gradually. On the other hand, the boundary regions tilted toward the downstream. Namely, the boundary moved from  $(z,r)=(0,0)$  to  $(10,10)$ . Moreover, the positive current region shifted to outer region from  $r = 5$  mm at  $10 \mu s$  to  $10$  mm at  $16 \mu s$ .

The  $j_\theta$  map showed that the absolute value of the negative  $j_\theta$  in the upper stream side

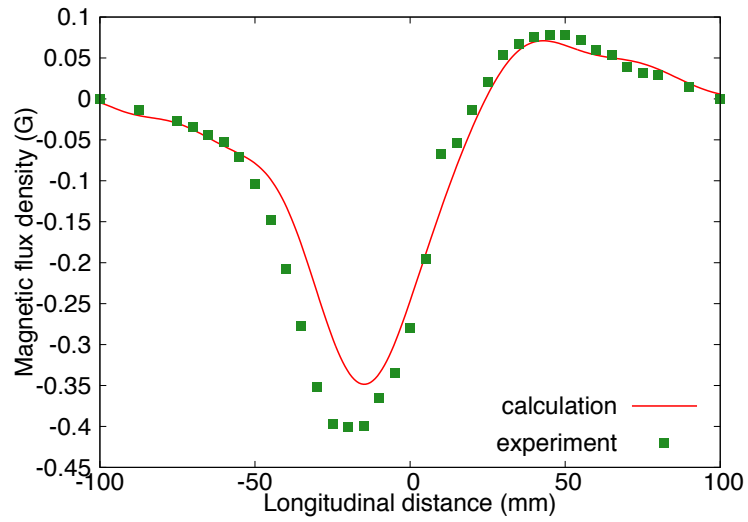
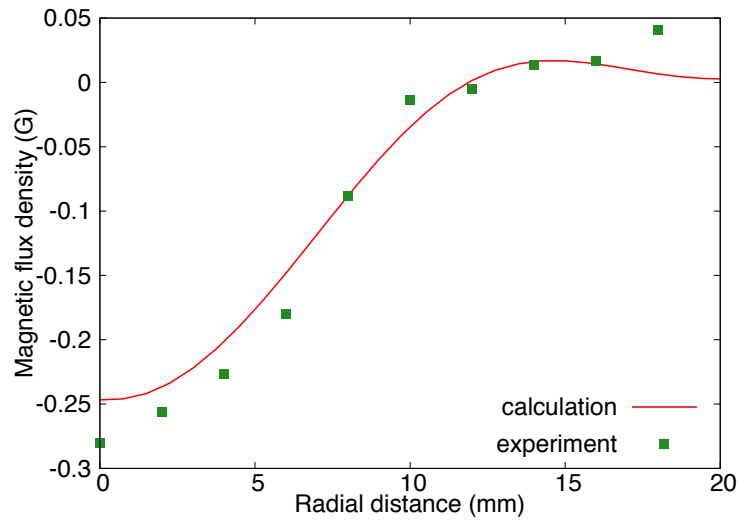
(a)  $\Delta B_z$  on  $z$  axis.(b)  $\Delta B_z$  on solenoid midplane.

Figure 3.13: Calculated and measured  $B_z$  on  $z$  axis as a function of longitudinal distance and on solenoid midplane as a function of radial distance at 10  $\mu$ s.

of the solenoid was larger than that of the positive  $j_\theta$  in the downstream side and the  $j_\theta$  changed from negative to positive at downstream,  $z > 0$ . These show  $j_\theta$  was induced asymmetrically with respect to the solenoid midplane. In addition, the asymmetry was largest at 8  $\mu$ s. This means that the head of the plasma plume induced the current more largely than the tail. Furthermore, in radial direction, the absolute value of  $j_\theta$  was smaller in the outer region.

From the  $j_\theta$  map, we found that the diamagnetic current evolves asymmetrically with respect to the  $r$  axis and  $z$  axis within the plasma plume, and the current is induced most largely by the head of the plume. Since negative and positive current generate negative and positive  $B_z$ , the  $j_\theta$  distribution is consistent with the evolving response of magnetic field shown in the section 3.3.

### 3.5 Discussion

We found that the magnetic field and the diamagnetic current evolves asymmetrically with respect to the solenoid midplane due to the diamagnetic effect. The asymmetries are induced more largely by the head of the plasma plume. The head has higher velocity. Consequently, the ratio of diffusion time of magnetic field to typical time of the plasma flow becomes larger for the head. In other word, effective  $R_m$  of the head region is higher. In this case, the head excludes more largely and is less magnetized. Therefore, the larger asymmetrical distortion of magnetic field probably results from the velocity distribution in the plume.

The diamagnetic current leads to radial Lorentz force  $j_\theta B_z$  on the plasma plume. Therefore, the larger negative current in the upper stream leads to larger force toward the axis while the smaller positive current leads to smaller force outward. Consequently, the plasma plume is subjected to net inward force. By this net force, the head of the plasma plume near axis are directed as shown in chapter 2.

On the other hand, the results showed that the outer region of plasma are magnetized more strongly. In chapter 2, we found that the outer region is converged like a magnetic lens. These indicate that the stronger magnetization results in such a behavior. For more



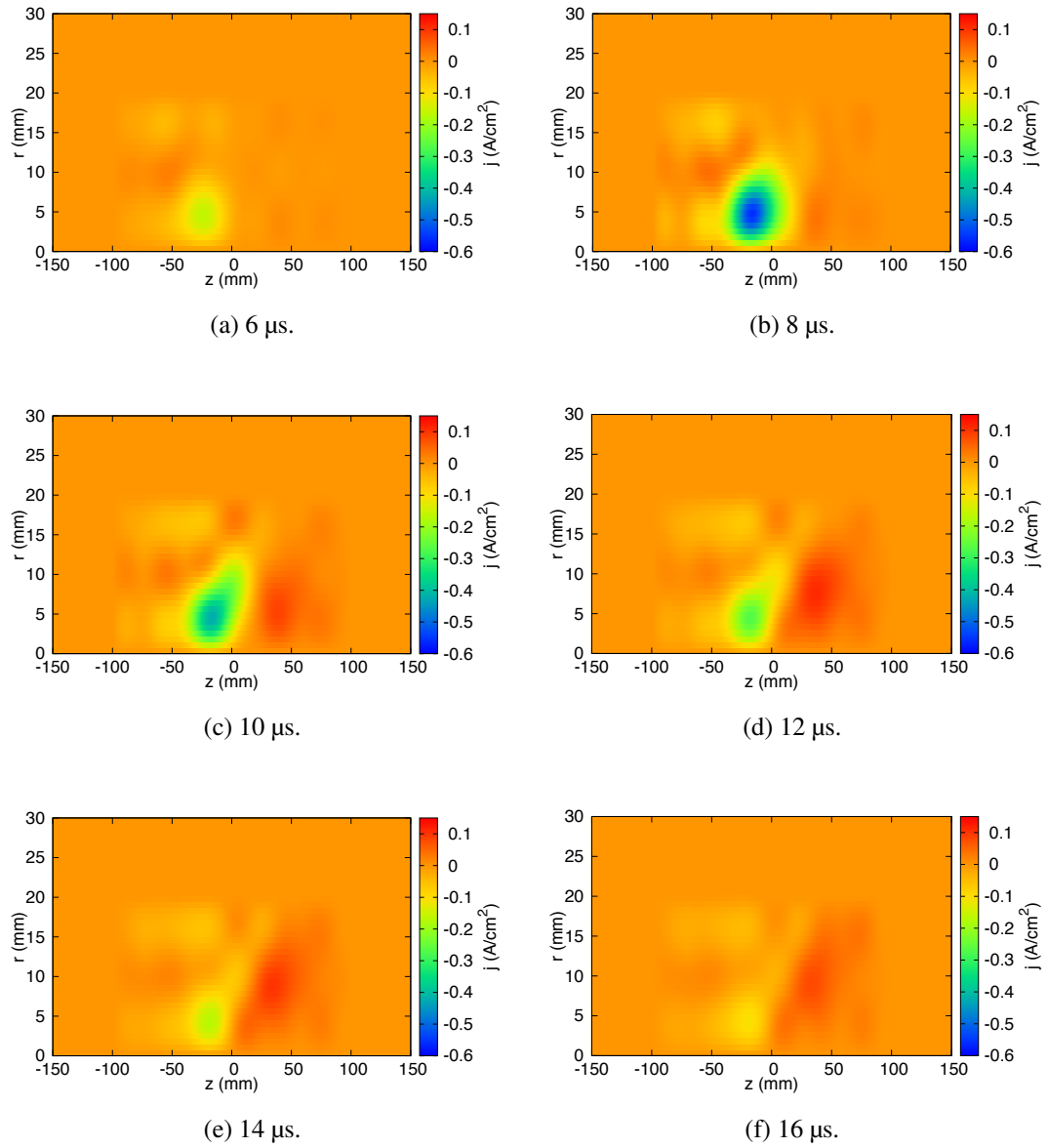


Figure 3.14: Diamagnetic current density distribution as functions of  $r$  and  $z$  at (a) 6, (b) 8, (c) 10, (d) 12, (e) 14, and (f) 16  $\mu\text{s}$ .

detail of the directing and converging process, further research is needed.

From the results in chapter 2 and 3, we found that magnetic field and diamagnetic current evolves asymmetrically while making a structure of the plasma plume. Namely, the head of the plume near the axis distorts the field more largely and is directed like a magnetic nozzle. On the other hand, the outer region are more magnetized and converged like a lens. This multiple behavior can not be explained by the conventional interaction models; snow-plow, collective guiding, and single particle model.

### 3.6 Concluding remarks

We measured the transient response of magnetic field  $\Delta B_z$  induced by the plasma injection with scanning a magnetic probe longitudinally and transversely. The longitudinal scan showed that the field decreased up to 2 % in the upper stream and restored in the downstream of the solenoid. The decrease was larger than the increase, and  $\Delta B_z$  became zero at the down stream. These mean that the field is excluded from the plume and dragged by the plume. Consequently the field is distorted asymmetrically by the interaction at  $R_m \sim 1$ . In addition, the asymmetric distortion by the head of the plume became larger than the tail. The transverse scan showed that the exclusion was larger at the inner region. This is corresponding to the fact that the magnetic field diffuses from the outside.

From  $\Delta B_z$ , we estimated diamagnetic current density distribution. The results showed that the current density was induced asymmetrically, namely the larger negative current in the upper stream and the smaller positive current at the down stream were induced, and additionally the current density changed from negative to positive at the downstream. In addition, the asymmetry induced by the head of the plume was larger probably due to the higher effective  $R_m$ . The distribution illustrated clearly the temporally and spatially evolving structure of the magnetic field.

We found that the magnetic field and the diamagnetic current evolve asymmetrically in laser ablation plasma. The behaviors are correlated to the plasma dynamics discussed in chapter 2. Namely, the inner head excludes and asymmetrically distorts the field more largely while directed the core plasma like a magnetic nozzle. On the other hand, the outer

region are more magnetized and converged like a magnetic lens. The guiding mechanisms induced by the time-dependent diamagnetic effects are not described by the snow-plow, the collective guiding, or the single particle model. This indicates that, by properly choosing the interaction parameter, the core of the laser ablation plasma can be guided by the nozzle-like effect without strong magnetization. By utilizing this effect, one could control laser ablation plasma without additional emittance growth.



## Chapter 4

# Guiding at Hot-dense Plasma Region

In the previous chapters, it was shown that, at the region with  $R_m \sim 1$ , inner head of the plasma plume is directed by the distorted magnetic field. This result indicates that if we increase  $R_m$ , the plasma would distort the field more largely and consequently the larger amount of the plasma is directed. During the early phase of expansion, the ablation plasma should have higher temperature and density in the smaller plume than those during the later lower density phase. The higher temperature leads to a higher conductivity and thus longer diffusion time. The higher density and the smaller plume size lead to a shorter characteristic time of the plasma flow. As a result,  $R_m$  should be higher if we apply the magnetic field during the early phase of expansion. Therefore, the plasma is expected to be directed more effectively.

From the view point, we investigated effects of magnetic field applied during the early high density phase [51, 52] and the later lower density phase of expansions by measuring plasma ion current density. In this chapter, we discuss the guiding effect during the early phase of expansion. Furthermore, we show the dependency of the effect on the charge state.

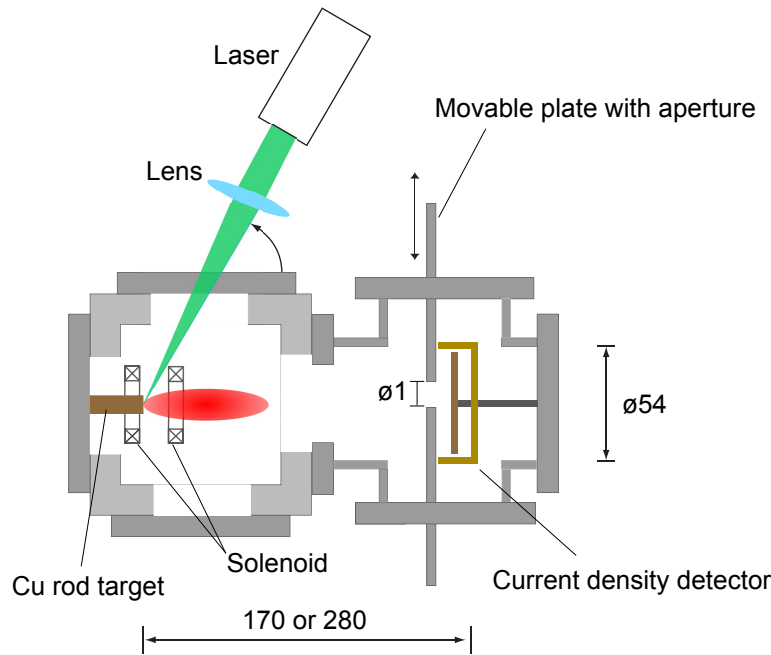


Figure 4.1: Schematic of experimental setup for plasma ion current density measurement.

## 4.1 Experimental setup for plasma ion current density measurement

The schematic of the experimental setup for the plasma ion current density measurements are shown in Fig.4.1. A Cu rod was placed in a chamber evacuated to  $5 \times 10^{-4}$  Pa. The surface was polished with an alumina powder to eliminate the influence of the surface roughness. The target was irradiated with laser at the incident angle of  $60^\circ$  to the target normal. The conditions are shown in Table 4.1. The spot size was estimated from the damage caused by the irradiation on the target surface. During the experiment, the Cu target was irradiated with weak laser light at 10 Hz to remove contaminations on the target surface while the main pulse was shot at about 1 Hz.

A split pair of solenoids was used for a generation of the axial magnetic field near the target. The diagram of the paired solenoid configuration is shown in Fig.4.2(a). The first of the pair of the solenoids was positioned over the target rod and the second was placed at a longitudinal distance of 7 mm. The former was 16 mm in length and wound 16 turns. The latter was 24 mm in length and wound 24 turns. Both were wound with 0.5 mm wire

Table 4.1: Laser conditions.

Laser Model	Spectra Physics: LAB-130
Laser type	Nd:YAG Laser
Wave length	532 nm
Pulse width (FWHM)	10 ns
Spot size on target	$4 \times 10^{-3} \text{ cm}^2$
Laser energy on target	50 mJ
Power density	$1 \times 10^9 \text{ W/cm}^2$

on a Delrin® tube with 14 mm in diameter. We also used a single solenoid to generate a magnetic field farther from the target. The diagram of the single solenoid configuration is shown in Fig.4.2(b) which was at a distance of 37 mm with respect to the target surface. The length and the diameter were 28 and 14 mm, respectively. The single solenoid was wound 56 turns with 0.5 mm wire on a Delrin® tube with 14 mm in diameter.

The magnetic field on the center axes were calculated as a function of the distance  $z$  from the target surface. Figures 4.3 (a) and (b) show the magnetic flux density on the axis for the solenoid current of 1 A.

The solenoids were energized by a LCR pulser. The equivalent circuit is shown in Fig. 4.4. The charge stored in the capacitor of 1500  $\mu\text{F}$  was discharged into the solenoids after a thyristor was triggered. The parameters of the circuit components were chosen so that a solenoid current did not vary during the time the plasma passed through the solenoid, around 5  $\mu\text{s}$ . From the calculated magnetic field shown in Fig. 4.3 and the solenoid dimensions, we can estimate the inductances of the solenoids. The magnetic flux through the solenoid is estimated by  $B_{z,c}\pi a^2 N$ , where  $B_{z,c}$  is the magnetic flux density of the center,  $a$  is the radius and  $N$  is the winding number. For the 17-mm-solenoid of the pair of solenoids, the inductance was estimated to be 2  $\mu\text{H}$ , while for the 26-mm-solenoid of the pair of solenoids, the inductance was estimated to be 4  $\mu\text{H}$ . Therefore, the inductance of the pair of solenoids were estimated to be 6  $\mu\text{H}$ . For the single solenoid, the inductance was estimated to be 20  $\mu\text{H}$ . In those case, the current with overdamping mode. The typical time scales of the current decay are estimated to be 600  $\mu\text{s}$  for the pair of solenoids and the single solenoid. Figure 4.5 shows a typical waveform of the current in the pair of solenoids measured with a current transformer. The current rose within 50  $\mu\text{s}$  and then decayed grad-

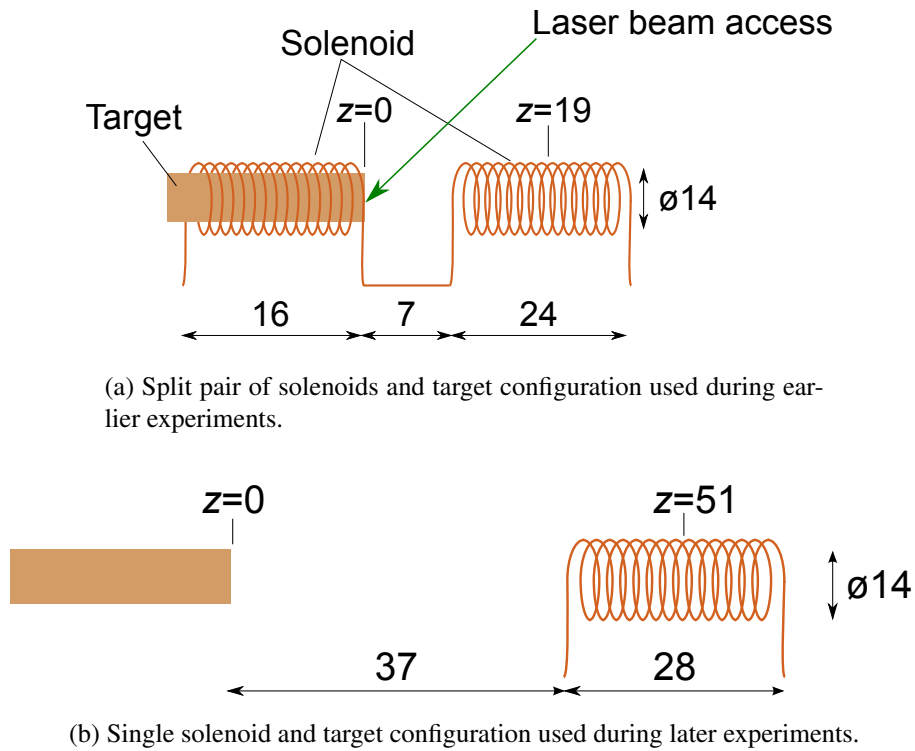


Figure 4.2: Diagram of solenoids.

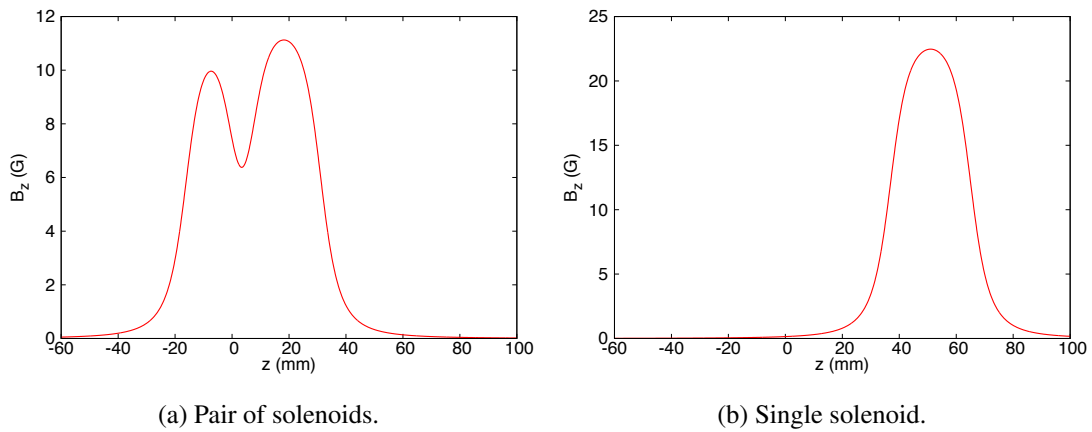


Figure 4.3: Calculated magnetic flux density of the solenoids on the axes when the current is 1 A.



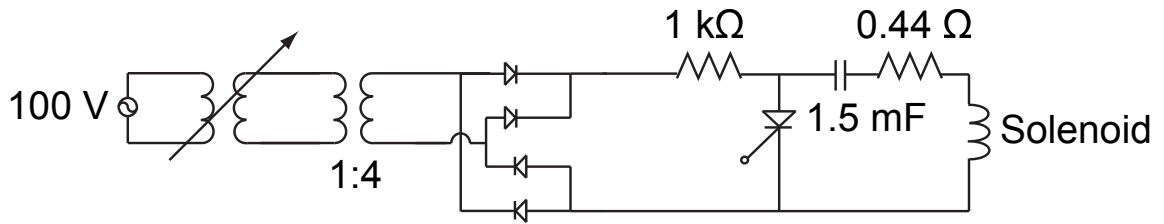


Figure 4.4: Diagram of pulse circuit energizing solenoids.

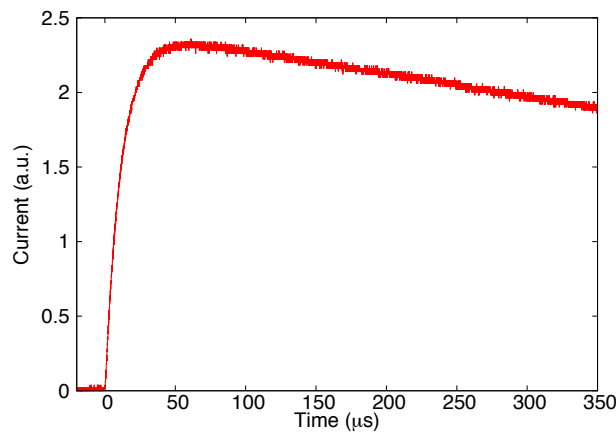


Figure 4.5: Typical waveform of current in pair of solenoids.

ually. The plasma passed through the solenoids when the current decayed. During the time, the solenoid current decreased by less than 0.5 %. Therefore, the magnetic flux through the solenoid was considered to be constant.

Figure 4.6 shows the schematic of a plasma ion current density detector. A copper plate covered by an aluminum sheet was negatively biased to repel the co-moving electrons and detect the ion current. A plate with 1-mm-diameter aperture was placed in the front. From the ion probe signal and the aperture area, we calculated the plasma ion current density. The plate with the aperture was movable transversely. A brass cover was placed around the ion probe to prevent the plasma coming around behind the plate. To determine the bias voltage, we investigated the relation between the plasma ion current and the voltage. Figure 4.7 shows the peak plasma ion current as a function of the absolute value of the voltage. The current was saturated at about -50 V. Therefore, we used -60 V as the bias voltage.

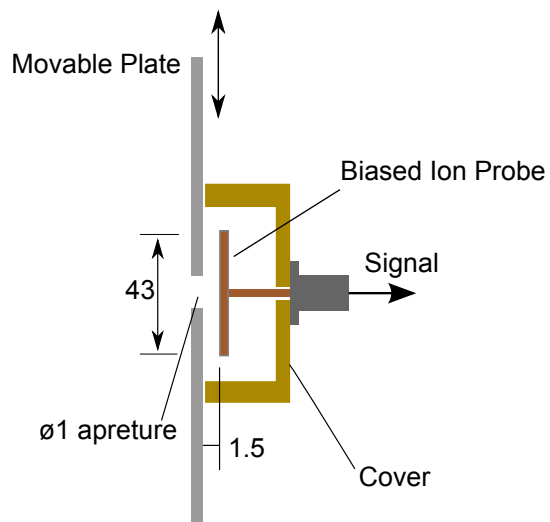


Figure 4.6: Schematic of plasma ion current density detector.

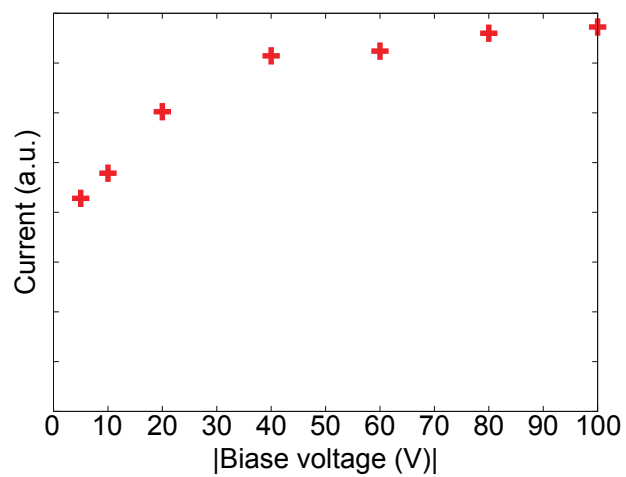


Figure 4.7: Peak plasma ion current as a function of absolute value of bias voltage.

## 4.2 Effects of magnetic field applications at hot-dense and lower density regions on plasma ion current density

### 4.2.1 Application at hot-dense region

Figures 4.8 show the typical waveforms of the plasma ion current density with various magnetic fields generated by the pair of solenoids. The horizontal axis is the time from the laser pulse. In the figures, 3 waveforms were overlaid at the same condition. The spike around 4  $\mu\text{s}$  was caused by the laser scattering. We took the spike signal as a time marker for the probe measurements. The figures show that the reproducibility was enough to discuss the effect of the magnetic field.

Figure 4.9 (a) shows the plasma ion current density waveform on the solenoid axis and at a distance of 170 mm from the target. The red curve shows the waveform without magnetic field. The peak current density was 50 mA/cm<sup>2</sup>. Since the peak time was around 4  $\mu\text{s}$ , the plasma drift velocity was estimated to be 40 mm/ $\mu\text{s}$ . From the scaling law of the proportionality of the plasma ion current density to  $z^{-3}$ , the current density was estimated to be  $4 \times 10^4$  mA/cm<sup>2</sup> at  $z=19$  mm and thus the ion number density was estimated to be  $6 \times 10^{13}$  cm<sup>-3</sup> there. Therefore, the number density decreased from the critical density ( $\sim 10^{21}$ ) to  $\sim 10^{13}$  cm<sup>-3</sup> within 1  $\mu\text{s}$ .

The green and blue curves show the plasma ion current density waveforms with the applied field of 1 kG and 3 kG, respectively. The magnetic flux densities were the values at the center of the solenoid at down stream, namely at  $z=19$  mm. The plasma ion current density was enhanced through the waveform and the peak current density was enhanced by larger than five times with both field strengths. On the other hand, the enhancement was different within the waveform and the difference depended on the magnetic field. Namely, the enhancement of the peak with the field of 1 kG was larger while that of the tail with the field of 1 kG was smaller. In addition, the plasma ion current density around 3  $\mu\text{s}$  increased while the current density with 0 G was almost nothing.

We measured angular distribution of the peak current density by changing the transverse distance  $x$  of the aperture.  $\theta$  was defined as the angle of the elevation of the aperture, namely  $\tan \theta = x/L$ , where  $L$  is the distance of the detector from the target. Figure 4.9(b)

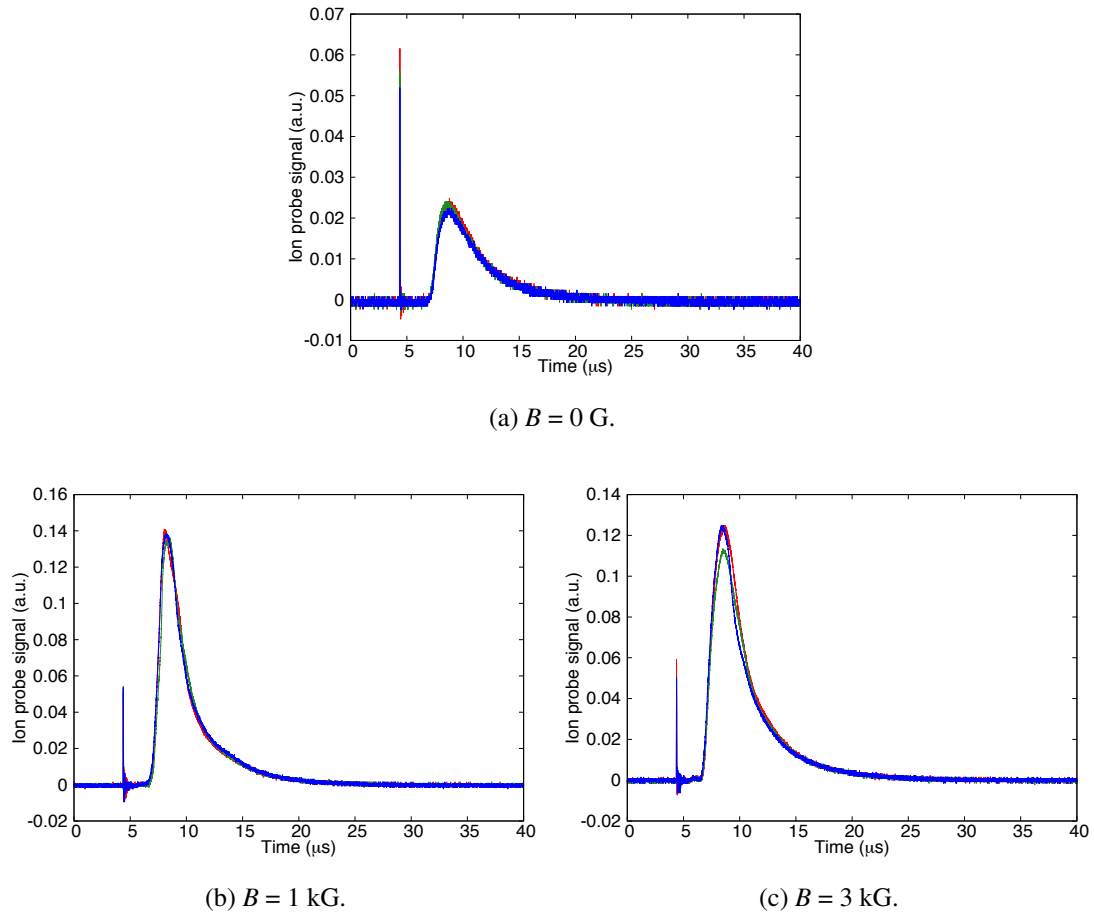


Figure 4.8: Typical waveforms of the ion probe signal with and without the magnetic field generated by the split pair solenoid and target configuration. 3 waveforms taken at same condition are overlaid in each figure.

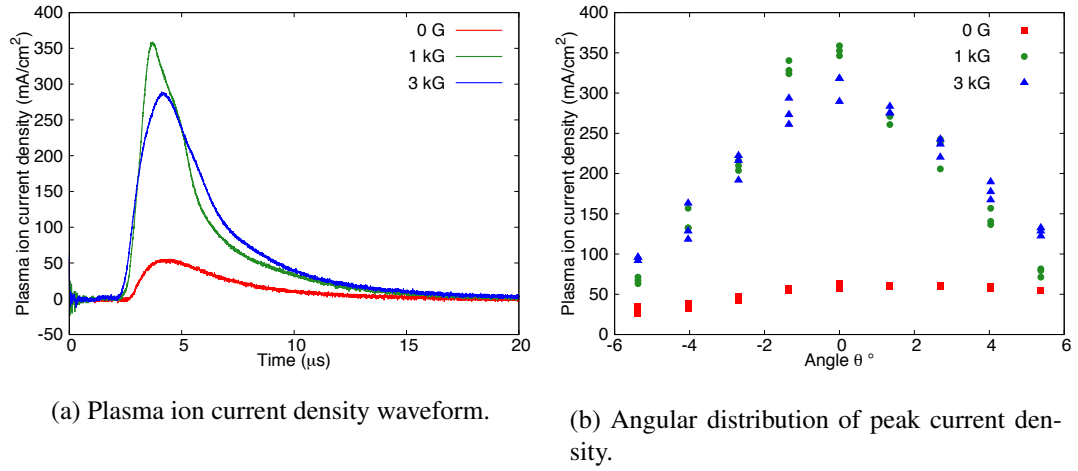


Figure 4.9: Plasma ion current density waveform on the solenoid axis and angular distribution of peak ion current density at a distance of 170 mm from the target with various magnetic fields.

shows the angular distributions with various magnetic field. Without magnetic field, the angular distribution was almost uniform. With the field, the plasma ion current density was enhanced and the distribution became narrow. This indicates that the plasma was directed. On the other hand, with the field of 3 kG, the distribution became wider and the plasma ion current density on the axis became smaller than those with the field of 1 kG.

Figures 4.10(a) and 4.10(b) show that the plasma ion current density waveform and the angular distribution of peak plasma ion current density at a distance of 280 mm. As shown in Fig. 4.10(a), the peak current density was one-fourth of that at  $z = 170$  mm without magnetic field. The decrease can be explained by the  $z^{-3}$  scaling law. With the magnetic field, the peak current density was enhanced by larger than five times, and the plasma ion current density was enhanced through the waveform. Figure 4.10(b) shows that the angular distribution of the peak current density became narrow with magnetic field. On the other hand, with the field of 3 kG, the plasma ion current density on the axis became smaller and the angular distribution became wider than those with the field of 1 kG. Fluctuations of the plasma ion current density occurred near the axis with the field of 1 kG while the fluctuation did not occur with the field of 3 kG.

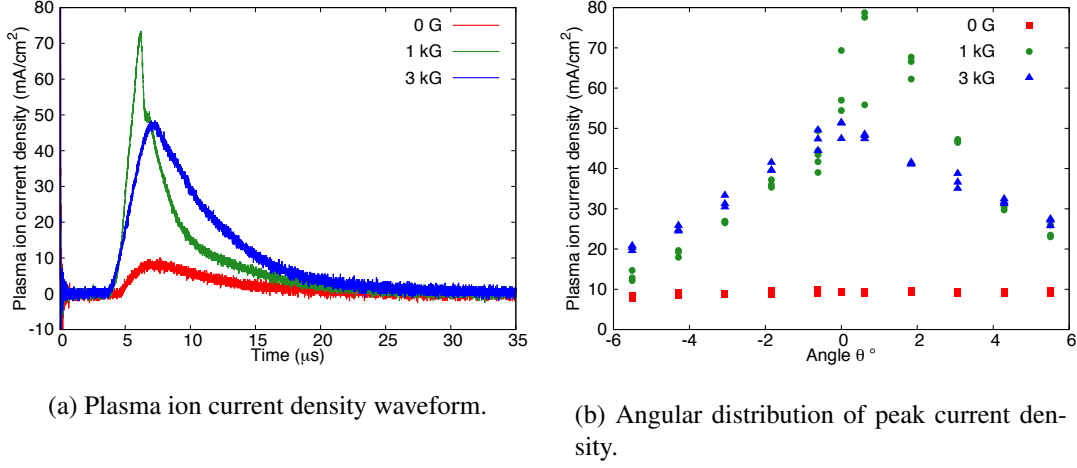


Figure 4.10: Plasma ion current density waveform on the solenoidal axis and angular distribution of peak ion current density at a distance of 280 mm from the target with various strengths of magnetic field.

We observed the enhancements and the narrow angular distribution at both distances of 170 and 280 mm with the magnetic field. These show that the enhancement did not result from converging ions but directed ones near the axis. From the fact, we found that the plasma is directed by the magnetic field and thus the plasma ion current density is enhanced through the waveform and the peak enhancement is more than five times. This is contrasting to the preferential enhancement of the plume head observed in chapters 2 and 3. On the other hand, the wider angular distribution by larger magnetic field may mean that the outer region was subjected to the diverging force from the diverging magnetic field due to the larger magnetization. Additionally, the fluctuations around the axis with the field of 1 kG may result from that the drifting direction was not along the axis.

#### 4.2.2 Application at lower density region

We investigated the effect of the single solenoid. Figure 4.11(a) shows the plasma ion current density as a function of time at a distance of 170 mm. Without magnetic field, the peak current density was around 50 mA/cm<sup>2</sup> around 4 μs. From the scaling law about the proportionality to  $z^{-3}$ , the plasma ion current density is estimated to be  $2 \times 10^3$  mA/cm<sup>2</sup>

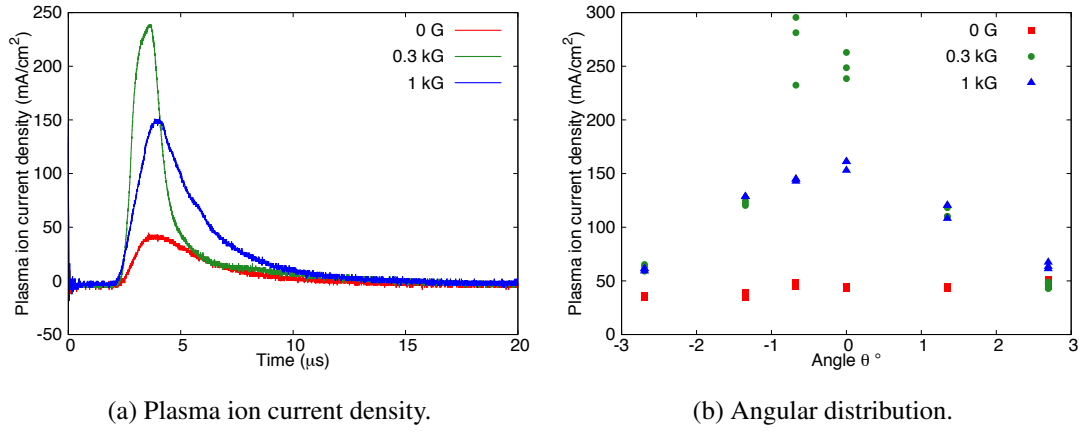


Figure 4.11: Plasma ion current density waveform on the solenoidal axis and angular distribution of peak ion current density at  $z=170$  mm with various strengths of magnetic field.

at the solenoid center ( $z=51$  mm). Therefore, the ion number density during the interaction with the magnetic field is estimated to be  $3 \times 10^{12} \text{ cm}^{-3}$ . With the field of 0.3 kG, the peak current density was enhanced by around 6 times. On the other hand, the tail of the waveform was not enhanced. With increase in the field to 1 kG, the peak current density became smaller while the tail increased. This is the same tendency as that in application at hot-dense region. However, the plasma ion current density around  $15 \mu\text{s}$  did not increase as much as at hot-dense region. This shows that the guiding at lower density region is less effective.

Figure 4.11(b) shows the angular distribution of the peak ion current density at  $z=170$  mm. Without magnetic field, the distribution was almost uniform. With the magnetic field, the plasma ion current density was enhanced and the angular distribution became narrow. This shows that the plasma was directed by the magnetic field. On the other hand, with the field of 1 kG, the plasma ion current density around the axis was enhanced preferentially. This indicates that there was an inner core interacting with the magnetic field more largely.

We investigated the effects of the guiding at hot-dense region and at lower density region on plasma ion current density. From the results, we found that the plasma ion current density near the axis is enhanced more largely through the waveform by the application at hot-dense region compared with that at the lower density region discussed in this section

and chapters 2 and 3. This shows that the magnetic field application at hot-dense plasma region leads to more effective guiding.

### 4.3 Dependency on charge state

The enhancement of the plasma ion current density on the axis was different within the current density waveform and the difference depended on the magnetic field. This indicates the influence of multiple charge state ions in the plasma plume. We used an electrostatic ion analyzer to investigate flux of ions for each charge state with various strengths of magnetic field.

#### 4.3.1 Principle of electrostatic ion analyzer and experimental conditions

Figure 4.12 shows the schematic of the analyzer. The analyzer was composed of two cylindrical deflection electrodes, two slits, and a secondary electron multiplier (SEM). The coaxial electrodes were biased such that the inner cylinder was negative with respect to the outer cylinder. The electric field between the electrodes are described by

$$E = \frac{U}{R \ln R_2/R_1}, \quad (4.1)$$

where the  $U$  is the potential between the electrodes,  $R_1$  and  $R_2$  are the outer radius of the inner electrode and the inner radius of the outer electrode, respectively, and  $R$  is a radius between the electrodes. The equation does not include the effect of the electrostatic fringe field. If the slits are small, the ions can be passed through the deflector only when the orbit coincides with the central equipotential. In this case, the following equation is satisfied,

$$\frac{mv^2}{Z} = \frac{eU}{\ln(R_2/R_1)}, \quad (4.2)$$

where  $v$ ,  $m$ , and  $Z$  are the velocity, the mass, and the charge state of the ion, respectively. Ions transmitted through the both slits are detected by the electron multiplier. From the



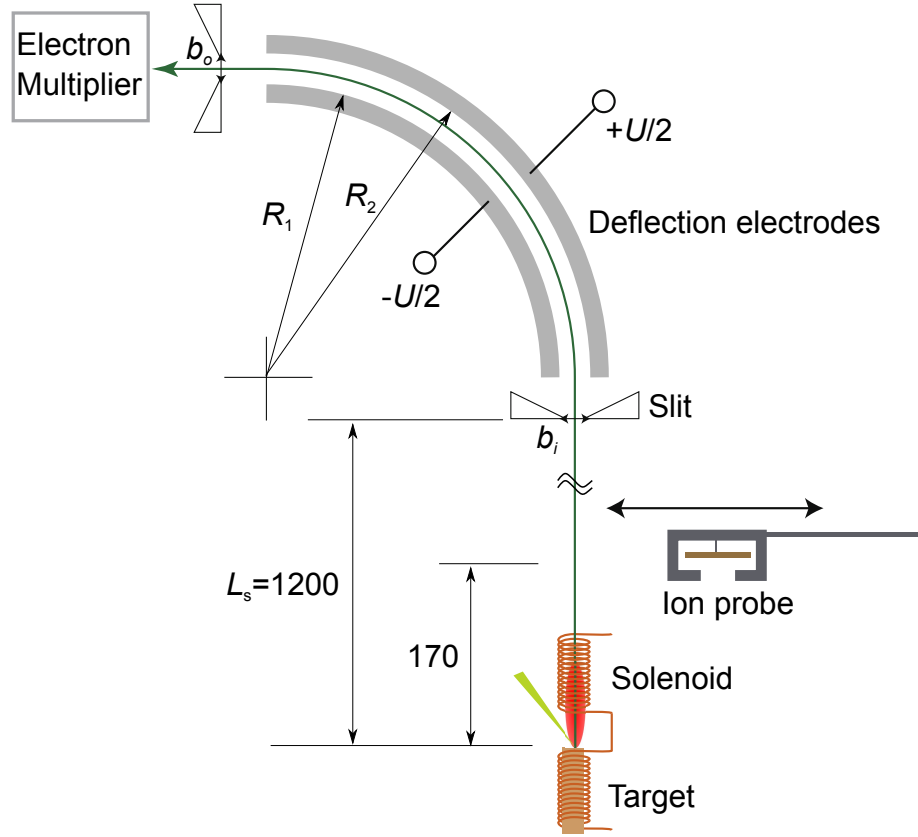


Figure 4.12: Schematic of electrostatic ion analyzer and arrangements of target and ion probe.

elapsed time and the length of flight path, the velocity can be calculated. Then we can identify the specific charge  $m/Z$ . If the ion mass are known, the charge state is identified. As a result, we determine the flux of the ions with the specific charge states and velocities [53].

We set  $R_1$  and  $R_2$  as 95 and 105 mm, respectively. The thickness of the electrodes was 5 mm. The slits were placed at a distance of 30 mm from the entrance and 25 mm from the exit.

Previous research showed that to avoid the space charge effect in the electrodes, the ion number density needs to satisfy the following inequality [54],

$$n_i \leq \frac{5 \times 10^8 E b_o}{L_s^2 z b_i}, \quad (4.3)$$

where  $L_s$  is the distance from the target to the slit at the entrance,  $b_i$  and  $b_o$  are the widths of the slits near the entrance and the exit. From this equation, we set the  $L_s = 1200$  mm,  $b_i = 0.05$  mm,  $b_o = 3$  mm. The path of flight was 1500 mm.

The SEM used in the analyzer was PHOTOS, MUGNUM 31308, Channeltron with the voltage of -1.2 kV.

We also measured plasma ion current density on the axis using an ion probe at a distance of 170 mm from the target. We used the laser condition and the pair of the solenoids used in previous section.

### 4.3.2 Flux of ions with various magnetic field

Figure 4.13 shows the typical signals of SEM with the magnetic field of 1kG, where 20 MHz low pass filter was used. In the figure, three signals at  $U=50$  V were overlaid which shows the good reproducibility. As shown, the 5 peaks were observed. The peak values mean the flux of each ion with a specific velocity  $v$  and ion charge state  $Z$  identified by Eq. 4.2. Because  $m/Z$  of  $\text{Cu}^{4+}$  and  $\text{O}^{+1}$  are almost same, those ions can not be resolved. However, since a series of charge state from 1+ to 5+ were observed and the signals from highly charged ions disappeared when the laser power density decreased, the peaks were identified to be signals of  $\text{Cu}^{4+}$  and  $\text{Cu}^{5+}$ . We obtained the flux of ions with other velocities  $v$  by changing  $U$ .

Figures 4.14 (a), (b), and (c) show the flux of each charge state ion as a function of time with 0, 1k, and 3 kG, respectively. Each plot is the average of 3 data. Figure 4.14(d) shows the estimated the plasma ion current density waveform at SEM from the ion probe signal at  $z=170$  mm. With the field of 0 G, the ions from 1+ to 4+ ions were observed. The fastest 4+ ions arrived around 20  $\mu\text{s}$ . This is consistent with the rising time of the plasma ion current density waveform. The flux of 2+ and 3+ ions were large around 35  $\mu\text{s}$ . This is also consistent with the peak in the waveform. The figure also shows that the highly charge state ions arrived earlier. This tendency was observed previously [20]. Some causes can be thought such as the temperature variation at the production, electrical acceleration by double layer [55], or difference of terminal mach number [56]. However, the reason has not been revealed in the measurements here.

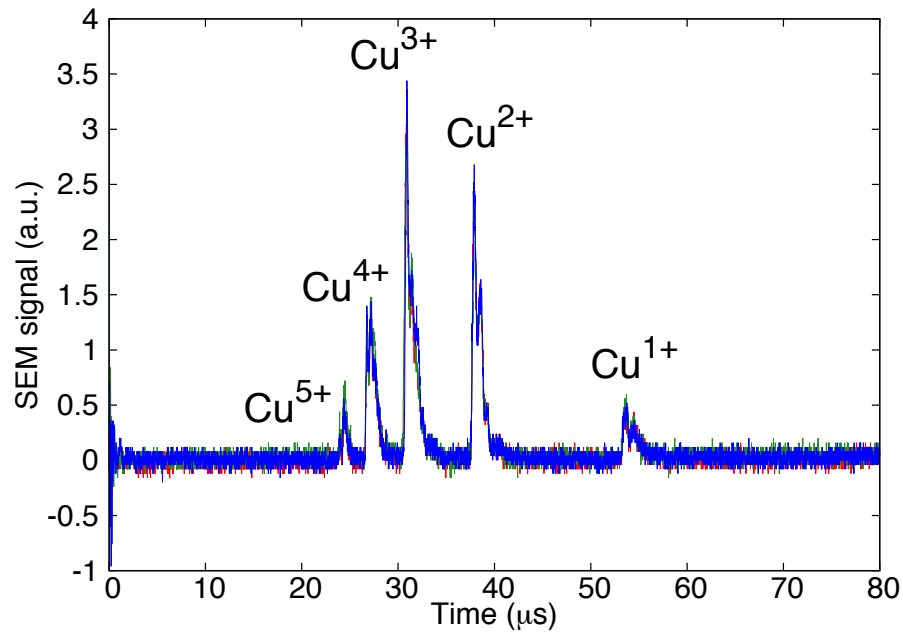


Figure 4.13: Overlaid three signals of secondary electron multiplier taken at same  $U$ .

Figure 4.14(b) shows the flux with the magnetic field of 1 kG. The flux of the 2+, 3+, and 4+ ions around 30  $\mu$ s were enhanced. This is consistent with the enhancement of the plasma ion current density around 30  $\mu$ s. Here, we emphasize again that the enhancements at 170 mm and 1500 mm mean that the plasma were *directed* along the axis. For 1+, the ions around 70  $\mu$ s were enhanced rather than 30  $\mu$ s. In addition, 5+ ions were observed while not with 0 G. This means that the enhancements was larger than those of other charge state ions.

Figure 4.14(c) shows that the flux with the magnetic field of 3 kG. The flux of 3+ ions around 30  $\mu$ s became smaller than that with the field of 1 kG. On the other hand, the flux of 2+ and 4+ ions did not change. Furthermore, the flux of 1+ ions around 50  $\mu$ s were enhanced. The tendency were consistent with that of the plasma ion current density waveform. Namely, the enhancement around the peak with the field of 1 kG was larger than that with the field of 3 kG while the enhancement of the tail with the field of 1 kG was smaller than that of the tail with the field of 3 kG.

The results showed that the guiding effect depends on the charge state of ions and that the effect is not explained by a gas dynamic effect.

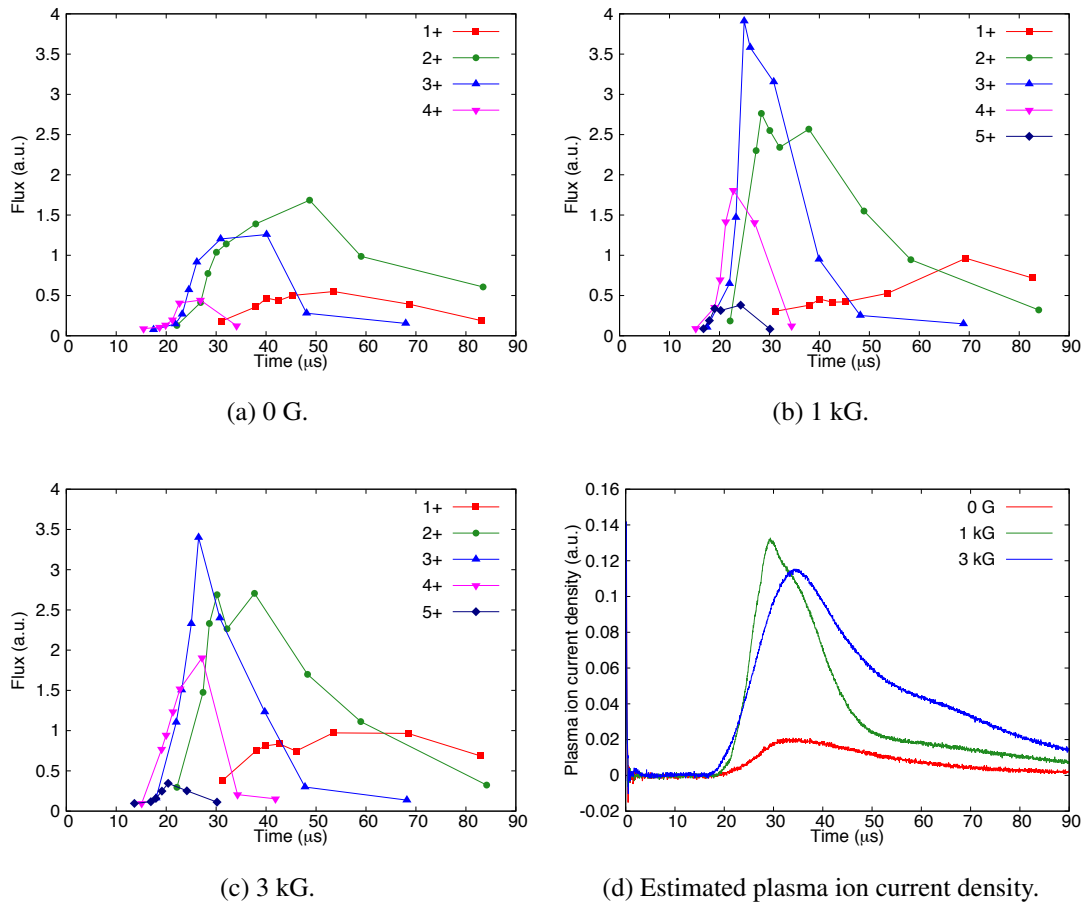


Figure 4.14: Flux of each charge as a function of time and estimated plasma ion current density at 1500 mm.

## 4.4 Concluding remarks

Effect of axial magnetic field on the plasma guiding at hot-dense region was investigated. When we applied the magnetic field near the ablation target, the peak current density enhanced more than 5 times near the axis. In addition, the enhancement occurred throughout the current density waveform. These mean that the plasma is directed from the head to the tail in contrast to the result in the previous chapters. Then, we applied the field farther a little from the target. The enhancement of the current density near the axis was observed again. On the other hand, the enhancement of the tail was smaller. The difference indicates that smaller amount of the plasma was guided due to the lower  $R_m$ . From the results, it was shown that the guiding effect becomes larger at the hotter-denser region.

We also measured the ion flux of a specific charge state with an electrostatic ion analyzer. The result showed that the magnetic field enhances the flux of ions for all charge states. On the other hand, the enhancement depends on the charge state, the velocity, and the magnetic flux density. This showed that the guiding of the ablation plasma is not simple, that is, it is neither explained completely by the lens effect nor by a gas dynamic effect.



## Chapter 5

# Plasma Control with Pulsed Magnetic Field

In the previous chapters, it was found that the plasma is directed by excluded magnetic field and it was indicated that the interaction with higher  $R_m$  leads to effective guiding. On the other hand, if the magnetic field is generated by a steady current as in the previous chapters,  $R_m$  is determined by parameters of the plasma. Moreover, the head of the plume is directed preferentially while the tail is hard to be guided. In case of guiding for long pulse beam, we need to guide the tail and reduce the variation of plasma ion current density within the pulse. In this chapter, we propose control of effective  $R_m$  and the behavior of the tail by a fast rising pulsed magnetic field. We show designs of a short solenoid and a pulse circuit to generate the pulsed field [57] and, then results of the test conducted in the laser ion source in the Brookhaven National Laboratory (BNL). The solenoid was designed so that it can be implemented during normal operating conditions.

### 5.1 Concept of control with pulsed field

If we apply a pulsed magnetic field faster than the diffusion time, in this case  $R_m$  is described by  $\tau_d/\tau_r$  and became higher, where  $\tau_d$  is the diffusion time and  $\tau_r$  is the rise time. Therefore, by using the fast rising pulsed field, the plasma guiding effect is expected to be larger. Furthermore, if we apply a proper pulsed field to the tail of the plasma plume,

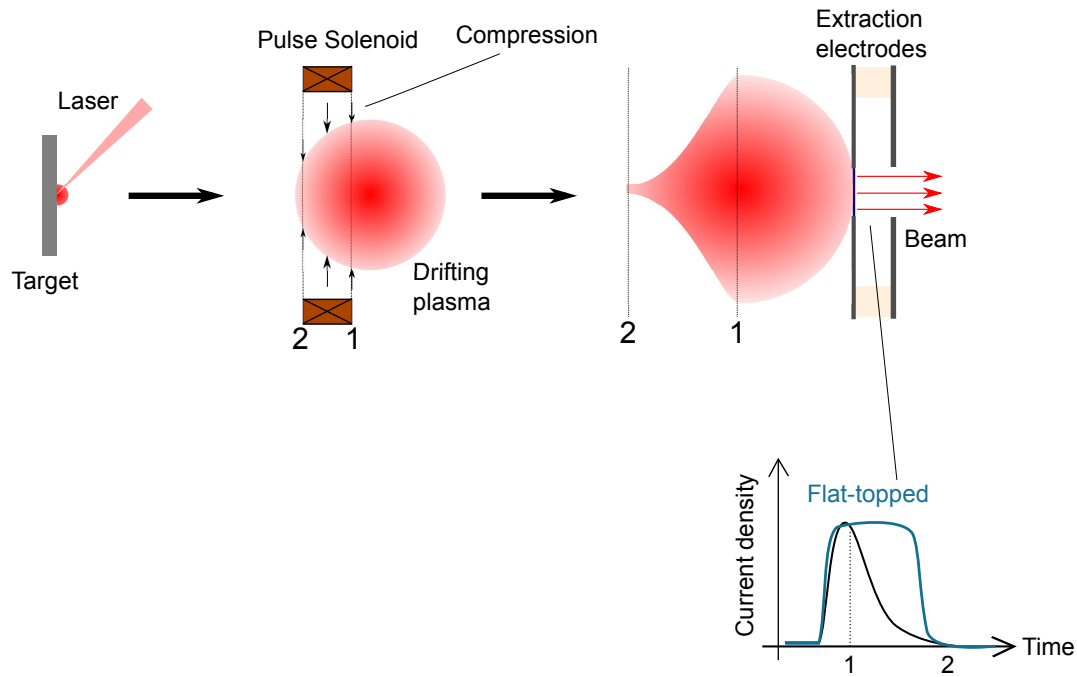


Figure 5.1: Image of ablation plasma control with pulsed magnetic field.

beam current waveform is expected to be regulated.

Figure 5.1 illustrates the idea. An ablation plasma drifts normal to the surface, then the head reaches a solenoid. The solenoid is not energized during the passage of the plume head. When the tail arrives, a fast rising magnetic field is applied. The field compresses and guides only the plume between the positions 1 and 2 as illustrated in the figure. Consequently, the plasma ion current density between 1 and 2 is enhanced at an extraction electrode that is placed at downstream. By adjusting the field properly, we can enhance the current of the tail and obtain a flat-topped shape.

## 5.2 Design of solenoid and pulse circuit

First we explain the laser ion source in BNL briefly [18]. Figure 5.2 shows a schematic diagram of the experimental set-up, which is composed of a target chamber, a 3-m drift tube, and an extraction system. In the chamber evacuated to  $\sim 10^{-5}$  Pa, various target species plates were placed on a linear stage. The stage allows the target motion and se-



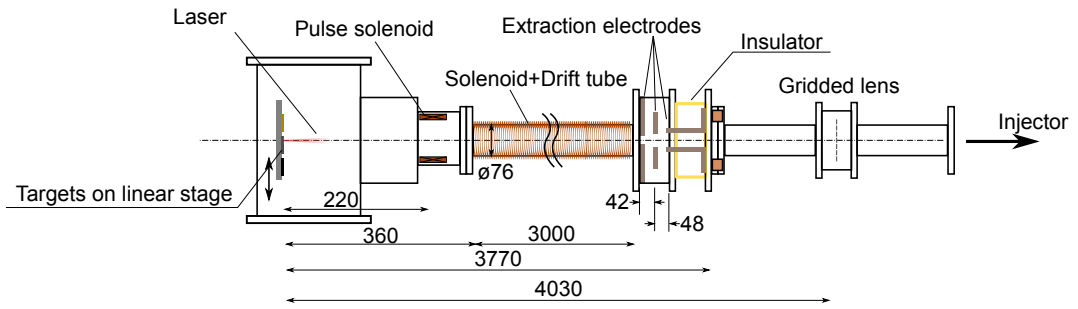


Figure 5.2: Setup of laser ion source in Brookhaven National Laboratory.

Table 5.1: Laser specifications for laser ion source in Brookahaven National Laboratory.

Laser Model	Quantel Brilliant B TWINS
Laser type	Nd:YAG Laser
Wave length	1064 nm
Pulse width (FWHM)	6 ns
Laser energy on target	400-700 mJ
Reputation rate	5 Hz

lection without breaking the vacuum and helps maintain suitable target surface. In the experiment using pulsed magnetic field, an iron plate was used as the target.

An ablation plasma was produced using a laser with specifications shown in Table 5.1. The power density was adjusted to produce singly charged ions. In the drift tube, the plasma is spread to to  $> 100 \mu\text{s}$  to adapt the extracted ion beam pulse width. A 3-m solenoid was placed on the space of the drift tube to modify the beam current in some cases. During experiments using the pulsed solenoid, it was not used. The extraction system was composed of three electrodes. The electrode at upper stream side was at the same potential as the target chamber that was designed to hold up to 40 kV. The potential of the intermediate electrode was adjusted to extract a parallel beam. The electrode at downstream side was grounded, i.e., to laboratory potential.

We installed a short solenoid producing the pulsed field in the target chamber. We designed the solenoid (referred to as pulse solenoid in the rest of this thesis) and the pulse circuit as follows.

The pulse solenoid was located at a distance of 220 mm from the target. Since the laser power density and the distance from the target to the pulse solenoid are similar to those of

the set-up in chapter 2, we can estimate that the plasma passes through the pulse solenoid around 10  $\mu\text{s}$  and around a field of 50 G is needed to guide the plasma. The inner diameter and the length of the solenoid were 80 and 56 mm, respectively, as shown in Fig.5.3. The solenoid coil was wound on a glass tube with inner diameter of 75 mm. The inner diameter is the same as that of the 3-m solenoid downstream to avoid disturbing the plasma during operation without the pulse solenoid. The length was chosen to be similar to the diameter.

To determine the rise time, we estimated the diffusion time  $\tau_d$  as below. The electron temperature is assumed to be 1 eV from the laser power density. From the number density estimation shown in chapter 2, the number density is assumed to be  $\sim 1 \times 10^{12} \text{ cm}^{-3}$ . Then, the plasma resistivity  $\eta$  is estimated to be  $\sim 5 \times 10^{-2} \Omega \cdot \text{cm}$  using the Spitzer resistivity described by Eq. 1.29. The characteristic length is assumed to be the radius of the pulse solenoid, 40 mm. Consequently, we obtained  $\tau_d = \mu_0 L_t^2 / \eta \sim 4 \mu\text{s}$ . From this, we set the required rise time of the pulse solenoid as 4  $\mu\text{s}$ . The fall time was set to be longer than the rise time.

To make the fast rising pulse, an LC circuit was used as explained later. From the requirements and the available capacitance, we decided to wind a coil with 86 times and 2 layers. A copper wire with a diameter of 2.3 mm was used. The inductance  $L_1$  measured by a Sencore Z meter was 700  $\mu\text{H}$ . The magnetic field distribution on axis was calculated by the software OPERA as shown in Fig. 5.4. The current was assumed to be 1 A. The horizontal axis is the distance from the target. A 0.3 mm thick steel shield was placed in the solenoid to eliminate the influence of the electric potential of the solenoid. As shown in the cut view (Fig. 5.5) and the photo (Fig. 5.6), a slit was made on the shield and the steel flange holding the solenoid to suppress the eddy currents driven by the pulsed magnetic field that would have counter acted the rising field.

Figure 5.7 shows the equivalent circuit of the pulse solenoid. The circuit is an LC circuit modified to set the rise time and fall time independently. First, the discharge capacitor C1 is charged up by a power supply V1 (SPELLMAN MPS5). V1 can be changed variably up to 5 kV. Then the discharge starts when the switch S1 (BAHLKE HTS 61-40) is turned on. Since the capacitors C2 and C3 are isolated due to the diode D2, the current flows into only the pulse solenoid L1 with a rise time determined by the C1 and L1. To rise the current around 4  $\mu\text{s}$ , we set the capacitance to 7.5 nF. In this case, the rising time is

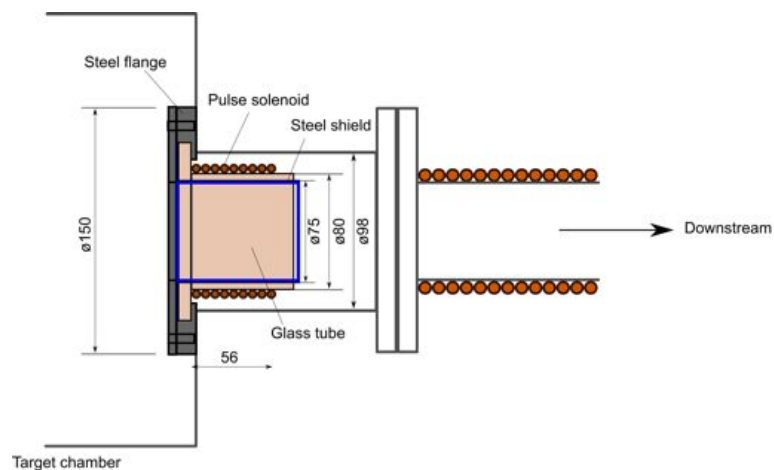


Figure 5.3: Dimension of pulse solenoid.

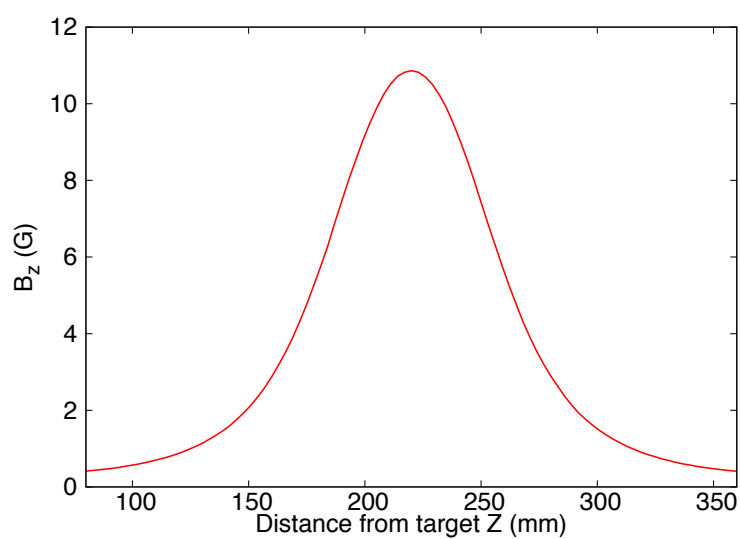


Figure 5.4: Calculated magnetic flux on axis as a function of distance from target.

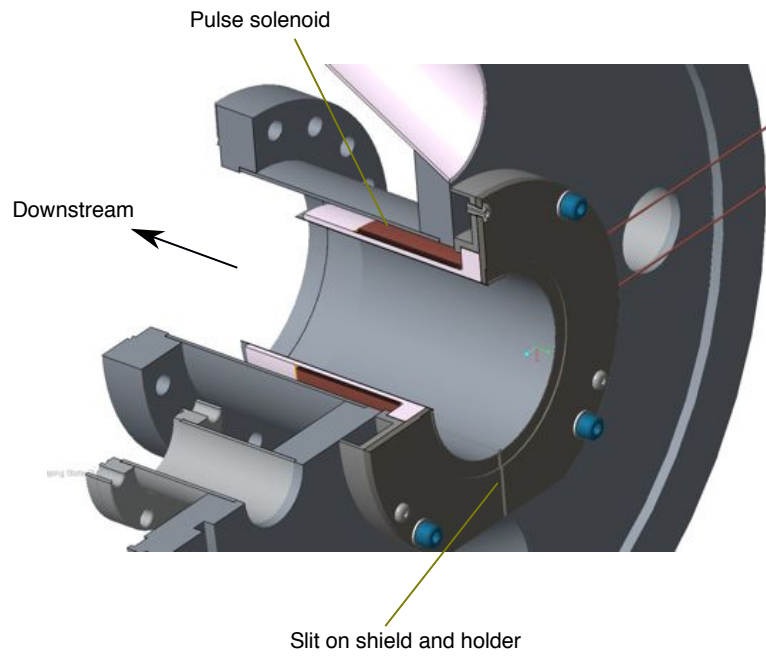


Figure 5.5: Cut view of pulse solenoid.



Figure 5.6: Photo of pulse solenoid.

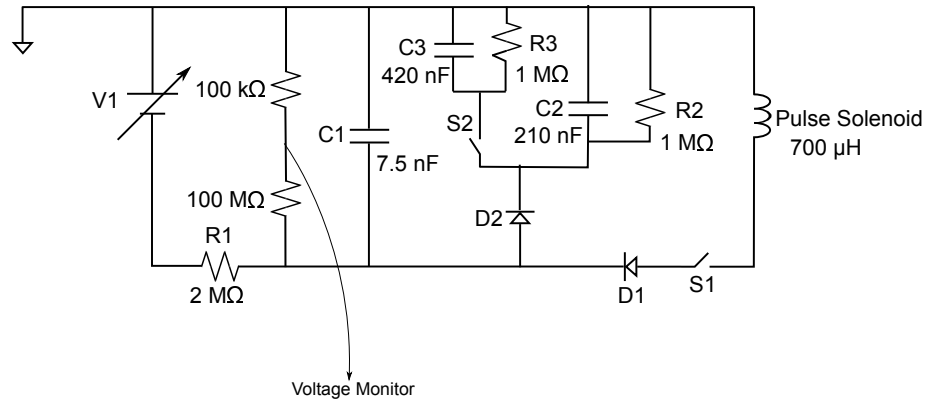


Figure 5.7: Equivalent circuit of the pulse solenoid.

$T/4 = 0.5\pi\sqrt{LC_1} = 3.6 \mu\text{s}$ . After  $C_1$  finishes discharging, the polarity of the voltage on  $L_1$  reverses and the current flows from  $L_1$  into  $C_1$  and  $C_2$ . At this time, if the switch  $S_2$  is on, the current also flows into  $C_3$ . The fall time of the current is determined by the capacitances. We chose the  $C_2$  and  $C_3$  as 210 and 420  $\mu\text{F}$  to produce the longer fall time  $\sim 20 \mu\text{s}$ . After the current becomes zero, the polarity reverses again and the current stops due to the diode  $D_1$ . Then,  $C_3$  and  $C_4$  are discharged through the resistances  $R_3$  and  $R_4$  until the voltages become zero. The  $R_1$ ,  $R_2$ , and  $R_3$  were chosen to accommodate the 0.25 Hz repetition rate of the laser ion source.

Figure 5.8 shows the typical current waveform in the pulse solenoid measured with a current transformer. The fast noise is pickup generated by the switch  $S_1$ , and is not real current. As shown, the current rose within 4  $\mu\text{s}$  and then fell with about 20  $\mu\text{s}$ . The 2 MHz oscillation at about 2  $\mu\text{s}$  may be caused by the resonance of the inductance and the stray capacitance of the pulse solenoid.

To investigate the influence of the electrostatic shield, the magnetic field at the center of the solenoid was measured with the magnetic probe used in the experiment in the chapter 3. In Fig. 5.9, the red curve shows the magnetic flux density estimated from the measured current while the green curve displays the measured value with the magnetic probe. The result shows that the magnetic field around the peak was reduced by about 50%. In addition, the fast oscillations were cut. This is because the slit capacitance allowed some eddy current to flow. In the following sections, the value of the magnetic flux density at the solenoidal center is estimated from the measured field, at the solenoid center.

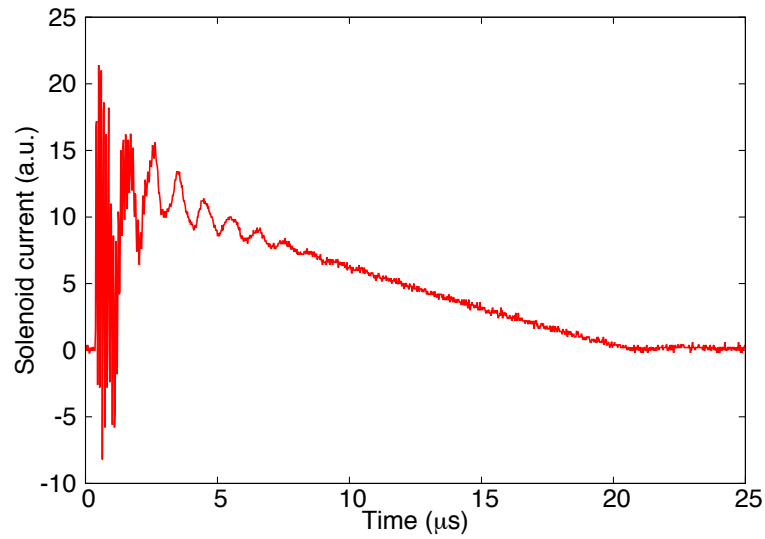


Figure 5.8: Typical current waveform of the pulsed circuit.

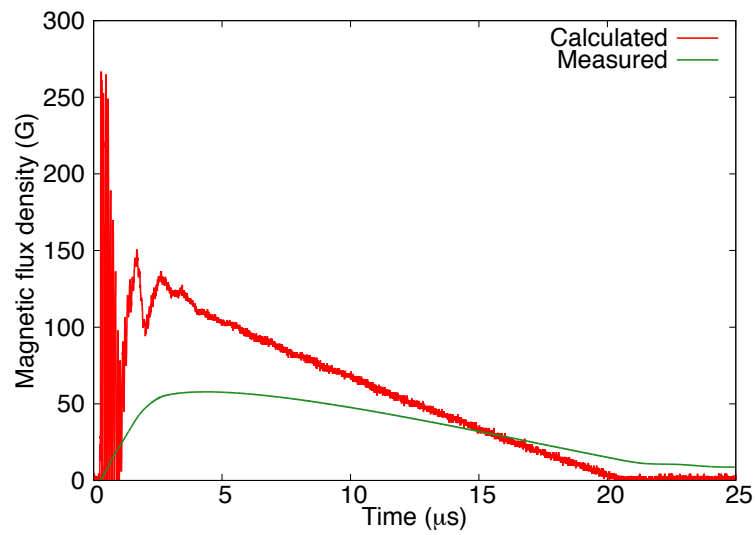


Figure 5.9: Magnetic flux densities calculated from solenoidal current and measured with magnetic probe as a function of time.

Table 5.2: Laser conditions for plasma ion current density measurement.

Spot size	0.3 cm <sup>2</sup>
Laser energy on target	400 mJ
Power density	$2 \times 10^8$ W/cm <sup>2</sup>

### 5.3 Effect of pulsed magnetic field

We installed the pulse solenoid in the ion source and conducted an experiment to test the effect. An iron target was placed on the linear stage in the target chamber evacuated to  $9 \times 10^{-6}$  Pa. The laser irradiating conditions are shown in Table 5.2. The vacuum target chamber was biased up to +15 kV with respect to ground. The potential of the intermediate electrode was adjusted to be -2.2 kV with respect to the target to extract a parallel beam. As shown in Fig. 5.2, we measured the beam current with a current transformer (ACCT-S-082) and a metal mesh added to a gridded lens downstream from the drift region. The lens was not energized. When the beam current waveforms measured by the detectors were similar, the ion beam was evaluated to be parallel.

Figure 5.10 shows the beam current waveforms measured by the metal mesh. The horizontal axis is the time from laser shot. The red curves in all the figures show the beam current obtained without the pulsed magnetic field. We estimated the current waveform at the center of the pulse solenoid by using a scaling law of time of flight. At the extraction, the ions were accelerated to  $2 \times 10^5$  m/s, and thus time of flight to the gridded lens was 1  $\mu$ s. Since the time is much smaller than that to the electrode, we do not take the time into account. The estimated current shape is shown in Fig. 5.11. It is found that the duration of the plasma passage through the solenoid is  $\sim 10$   $\mu$ s.

The blue curves in Fig. 5.10 show the beam current waveforms obtained with the pulsed magnetic field of 60 G. We triggered the pulse circuit at  $t_{on} =$  (a) 12, (b) 16, (c) 20, and (d) 24  $\mu$ s after the laser pulse. As shown, the beam current was enhanced partially within the tail part of the beam pulse. The enhancement was different within enhanced part, or namely the peak was formed in enhanced part. The peak and the enhanced part shifted later with increase in  $t_{on}$ . On the other hand, the beam current was reduced after the enhancement.

To confirm that the partial enhancement was caused by the rising magnetic field, we

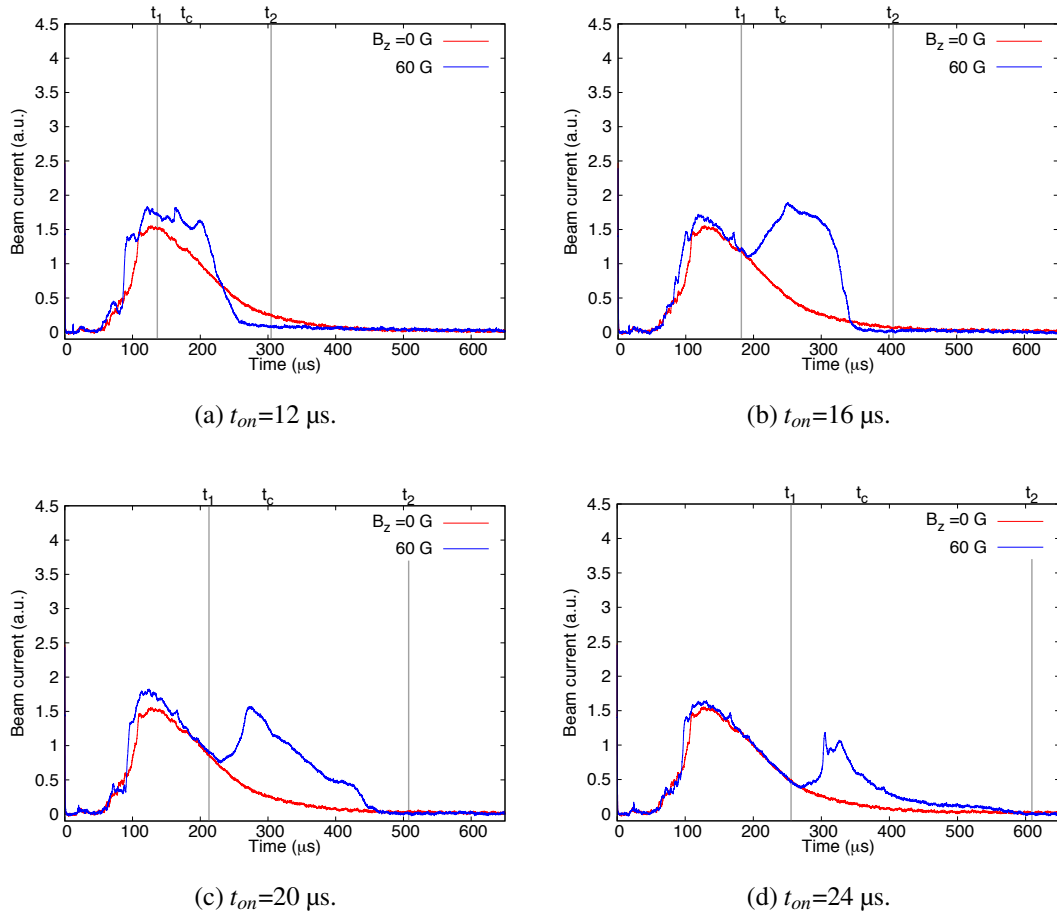


Figure 5.10: Beam currents as a function of time in the cases of 0 G and 60 G with the some trigger timings  $t_{on}$ .



estimated durations of the enhanced parts in current waveform as below. Figure 5.12 shows an image of the time sequence from the application of the pulsed magnetic field to the beam extraction. At  $t = t_{on}$ , the pulsed field was triggered as shown in Fig. 5.12(a). At this time, a part of the plasma in the solenoid between the distances of  $L_1$  and  $L_2$  was compressed. Although the plasma was moving while the field was rising, we assumed that the field rose immediately for simplicity of this estimation. From the field distribution shown in Fig. 5.4, we assume  $L_1=310$  mm and  $L_2=130$ , where the magnetic fields become 10 % of the peak value. Then, the plume drifts to the extraction electrodes. At  $t = t_1$ , the front edge of the compressed part arrived as shown in Fig. 5.12(b), where  $t_1$  is estimated by  $t_{on}(L_e/L_1)$ , and  $L_e$  is the distance to the electrodes. The rear edge arrived at  $t_2$  as shown in Fig. 5.12(c), where  $t_2$  is also estimated by  $t_{on}(L_e/L_2)$ . We show the  $t_1$  and  $t_2$  as the vertical lines in Fig. 5.10. We can find that the extracted ion pulse current was enhanced between  $t_1$  and  $t_2$  for all  $t_{on}$ . This shows that the fast rising pulsed magnetic field enhances the beam current partially within the beam pulse.

The peak formation in the enhanced part indicates the influence of the variation of the magnetic field along the solenoid axis. To check this, we also estimated the arrival time of the part of the plasma that was at the solenoidal center at  $t = t_{on}$ . The arrival time  $t_c$  is estimated by  $t_{on}(L_e/L_c)$ , where  $L_c$  is the distance from the target to the center, 220 mm. We put the labels  $t_c$  at the time and on the top of Fig. 5.10. As shown,  $t_c$  was around the peak forming time for all  $t_{on}$ . This shows that the reason of the peak formation is the stronger magnetic field around the center. Therefore, it was found that the shape of the enhanced part depends on the variation of the magnetic field along the axis.

Figure 5.13 shows the extracted ion beam current waveforms with various pulsed magnetic field strengths and with different  $t_{on}$ . The waveforms shown in Fig. 5.13(a) were obtained for the case of  $t_{on}=12$   $\mu$ s. The current was enhanced partially between  $t_1$  and  $t_2$  with increasing the field. The peaks were formed around  $t_c$  with the field of 40 and 60 G while the peak with the field of 80 G was formed slightly later than  $t_c$ . For all magnetic field strengths, the reduction of the current around  $t_2$  was observed. The waveforms shown in Fig. 5.13(b) were obtained for the case of  $t_{on}=16$   $\mu$ s. The current was also enhanced partially with increase in the magnetic field, and the peak formed around  $t_c$ . On the other hand, the enhancement with the field of 60 G was not so different from that with the field

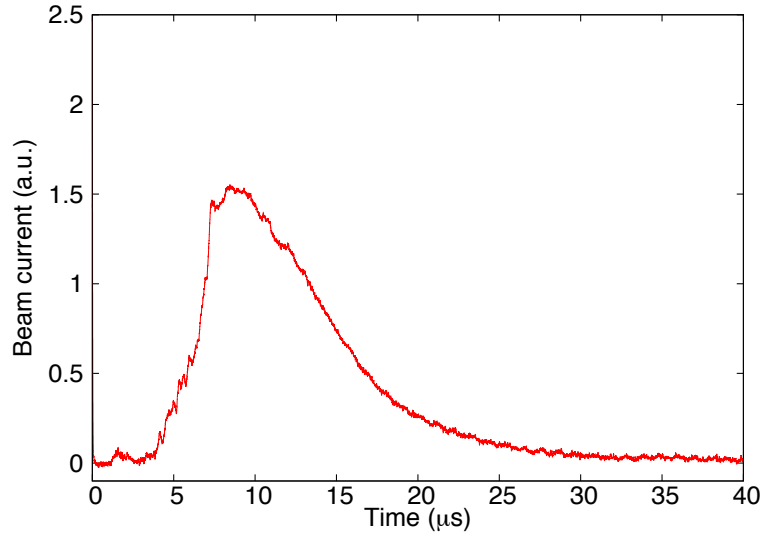


Figure 5.11: Estimated current with no magnetic field at center of pulse solenoid.

of 80 G compared to the difference in the case of  $t_{on}=12\ \mu\text{s}$ .

The results show that the enhancement depended on the magnetic field strengths and in most cases, the peak was around  $t_c$ . These show that the enhancement can be controlled the strength and the distribution of the magnetic field. On the other hand, we observed that the increase of the enhancement with increase in magnetic field was different with  $t_{on}$ . In addition, the peak was formed later than  $t_c$  with  $t_{on} = 12\ \mu\text{s}$  and with the field of 80 G. These tendencies indicate the enhancement does not depend only on the strength of the magnetic field, and further research is needed for more optimization.

The results showed that the pulsed field can be used to control the current waveform of the extracted ion beam by changing the pulsed magnetic field timing and strength. Finally, we adjusted the field to tailor the shape to be flat-topped. Figure 5.14 shows the result. The blue curve was obtained with the magnetic field of 60 G applied at  $t_{on}=14\ \mu\text{s}$ . The current maintained the peak for 200  $\mu\text{s}$ . In addition, the current of the tail was cut. This is also better from the point of ion source, because of the reduction of the extra beam. It is believed that such a flat-topped ion pulse will lead to a more efficient transport ion injection into the electron beam ion source at the Brookhaven National Laboratory. From the results, we demonstrated to make a flat-topped pulse shape by the pulsed magnetic field.

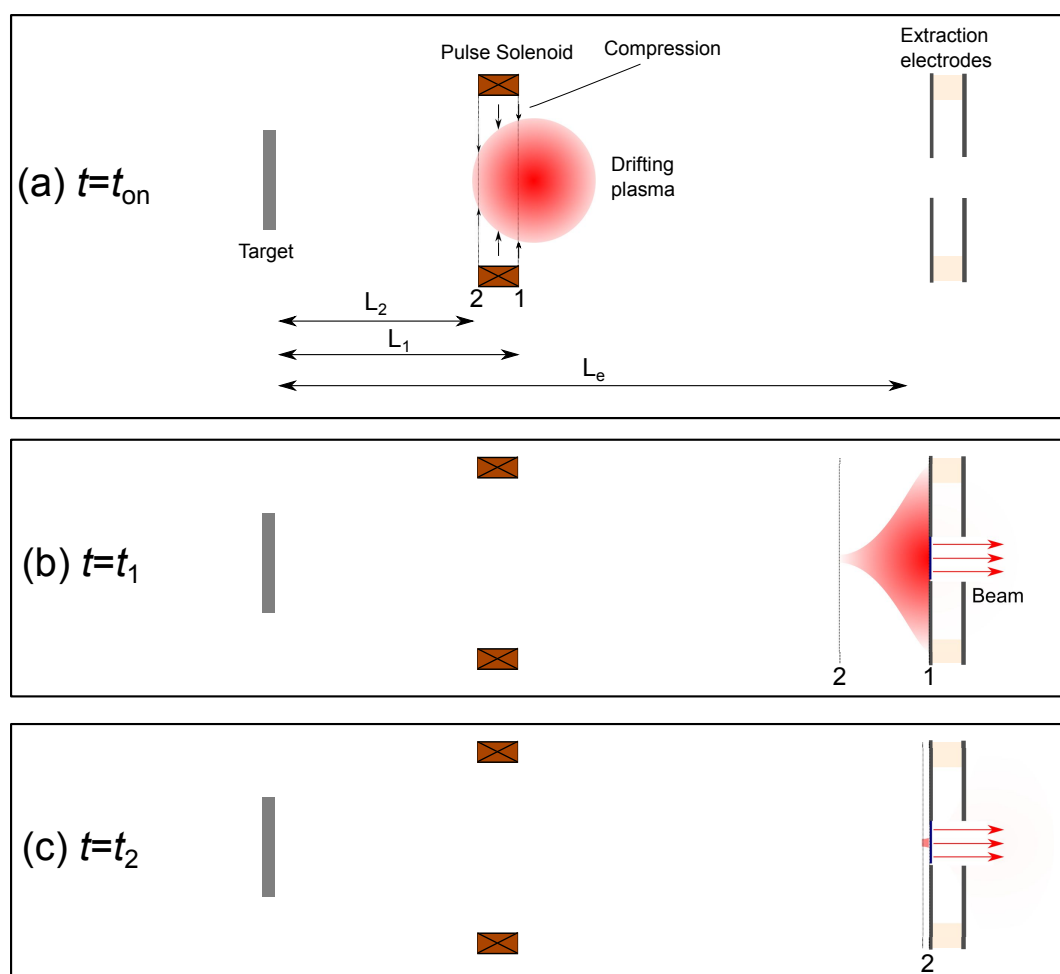


Figure 5.12: Time sequence from pulse compression to extraction.

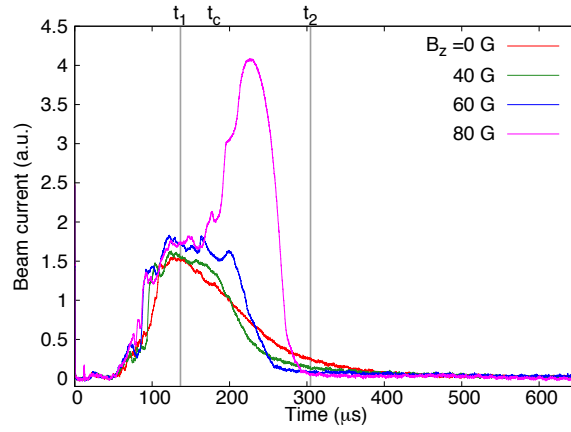
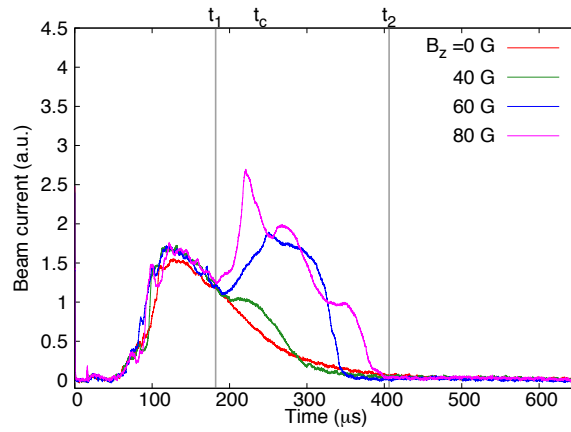
(a)  $t_{on}=12\ \mu\text{s}$ .(b)  $t_{on}=16\ \mu\text{s}$ .

Figure 5.13: Beam currents as a function of time with various pulsed magnetic field amplitudes.

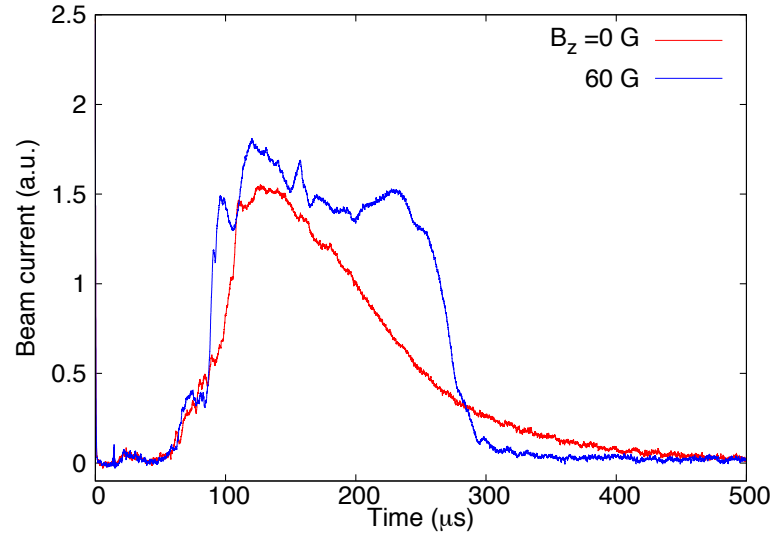


Figure 5.14: Example of flat-topped current shape formed by applying pulsed magnetic field of 60 G at  $t_{on}=14\ \mu\text{s}$ .

## 5.4 Concluding remarks

We designed a short solenoid and a pulse circuit to produce a pulsed magnetic field faster than the diffusion time for enhancement of the beam current of the tail part. The magnetic field driven by the pulsed coil rose within  $4\ \mu\text{s}$  and then fell within  $20\ \mu\text{s}$ . We installed it into the laser ion source in Brookhaven National Laboratory to test the effect of pulsed field on the extracted beam current. The result showed that the beam current of the tail part is enhanced and the enhanced part shifts when the trigger timing from the laser shot is varied. In addition, the enhancement of the extracted ion beam current depends on the magnetic field distribution and strength. These showed that the fast-rising pulsed magnetic field guides the tail part of the plasma plume it acts upon, and that we can control the beam pulse shape by adjusting the rise time, timing, strength, and distribution. On the other hand, the pulse field decreased the subsequent part of the enhanced current waveform. Finally, we demonstrated making a flat-topped ion current waveform by adjusting the pulsed magnetic coil.



# Chapter 6

## Conclusions

In this thesis, behaviors of laser ablation plasma through an axial magnetic field were discussed to develop a well-controlled high current ion source.

In chapter 1, the background and the purpose of the study were presented, in which it was pointed out that control of laser ablation plasma with magnetic field is a key technique to develop a high current and low emittance ion source. After discussion of the interaction process, we indicated that the qualitative behavior can be characterized by the magnetic Reynolds number  $R_m$ . We also showed that, in the case of the high flux ion source utilizing a laser ablation plasma,  $R_m$  is always around 1 in the interaction region. Therefore, both the convective and the diffusive effects play some roles. From this view point, we pointed out that the interaction should make a structure in the plasma plume which needs to be made clear to develop the well-controlled ion source.

In chapter 2, effects of a magnetic field on the behavior of laser ablation plasma was discussed in a parameter region with  $R_m \sim 1$ . We applied an axial magnetic field to the plasma with a short solenoid. Then, the time-space distribution of the plasma ion current density were measured with an ion probe. The results showed that the magnetic field makes a structure in the plasma plume. Namely, the outer plasma converges to a point like a magnetic lens depending on the magnetic flux density and the ion velocity. On the other hand, the tail of the plume near axis is not affected while the head is directed rather than converged.

In chapter 3, responses of the magnetic field against the plasma injection were dis-

cussed. Time and space distributions of the field were measured by a magnetic probe. The field was excluded from the plume in the upper stream side and dragged by the plume in the down stream side of the solenoid. The field exclusion was larger than the drag. In addition, we observed larger distortion by the head of the plasma plume than the tail. Furthermore, we also observed that the field near the axis was excluded more largely than in the outer region. These results showed that the magnetic field evolves asymmetrically with respect to the midplane of the solenoid within the plasma plume, and that the head of the plasma plume near axis distorts the field more largely.

Based on the field measurements, distributions and evolutions of diamagnetic current were estimated. The results showed that the current is induced asymmetrically, which leads to a net converging force on the plasma. The results also showed that the field evolves asymmetrically within the plume. From the comparison of the results in the chapter 2 and 3, it was found that the plasma and the magnetic field interact accompanied by making a structure in the plume.

We predicted that the hot and dense plasma at an early phase of the expansion was expected to exclude more magnetic field and be guided effectively because of the higher  $R_m$ . The guiding was investigated by the measurement of the plasma ion current density with applying an axial magnetic field near the target. We observed around 5 times enhancement of the peak current near the axis. In addition, the current density was enhanced throughout the waveform. These showed that the guiding effect becomes larger at the region. On the other hand, we found the enhancement depends on the charge states from the measurements with an electrical ion analyzer.

In chapter 5, we showed an example of plasma current control, in which a waveform control was demonstrated using a fast field. We expected that effective  $R_m$  can be increased by using a pulsed field rising faster than the diffusion time. Then we proposed a scheme using the pulsed field for control of the beam current waveform. A solenoid and a pulser to generate the pulsed field with rising time of 4  $\mu\text{s}$  were designed and the effect on the extracted beam current was tested. We observed a partial enhancement of the current waveform increase depending on the timing and the strength of the field application. This showed that the plasma can be guided by the fast rising pulsed field. Finally, by adjusting the timing and the strength, we demonstrated a flat-topped beam current waveform.



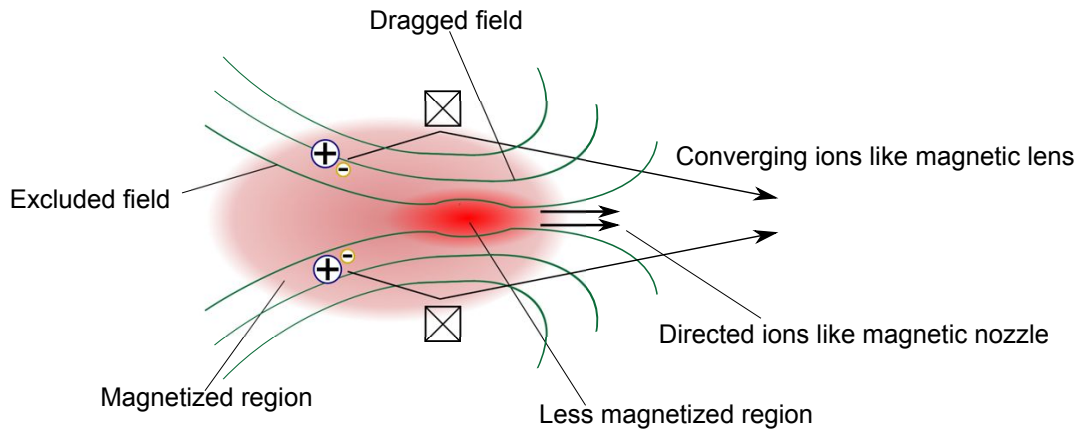


Figure 6.1: Illustration of interaction between laser ablation plasma and magnetic field.

Figure 6.1 shows a schematic illustration of the plasma and magnetic field interaction and the guiding mechanisms. From the results in this study, we found new guiding mechanisms; the guiding of the inner head like a magnetic nozzle and the guiding of the magnetized outer region like a magnetic lens as shown in Fig. 6.1. These are not described by conventional guiding mechanisms; a guiding by snow-plow like compression, a collective guiding, and a guiding of single particle.

A notable point obtained in this study is that there is a region that directs the ions like a magnetic nozzle in this guiding mechanisms. The region is desirable for ion source because the current density can be enhanced without additional emittance growth. Results showed that the effect can become more effective by applying the magnetic field at higher  $R_m$  region. This can be accomplished by interacting the plasma at hot-dense phase of ablation and/or by applying a pulsed magnetic field faster than the field diffusion time. That is a basic concept of plasma guiding obtained in this study for the development of a well-controlled ion source.

Finally, we would like to emphasize that the guiding with axial magnetic field at proper parameter regions will be a key technique leading to a novel ion source and thereby an intense ion accelerator beyond conventional power levels.



# Appendix A

## Guiding of Plasma with Long Solenoid

A laser ablation plasma can be guided by a solenoidal magnetic field in a laser ion source for controlling the beam current. For a practical use, a relatively low magnetic field, which is from 1 to 100 G, is important. In Brookhaven National Laboratory (BNL) a 3 m long solenoid is being used for the routine operation. In this chapter, we discuss the effects of the solenoidal magnetic field on the beam as a part of the ion source based on a setup used in BNL. First, we show the effects on the current and the total charge within a single pulse of beams of several types of ion species, and then the influence on the beam extraction related to the beam optics. Finally, we show the behavior of the plasma inside the solenoid and discussed the plasma confinement.

### **A.1 Effects on current and total charge of beam extracted from laser ablation plasma**

A systematic analysis of the long solenoid effects had not been performed on the laser ion source in BNL. Therefore, we investigated the effects on peak current, total charge within a single beam pulse, and a waveform for several types of ion species [58].

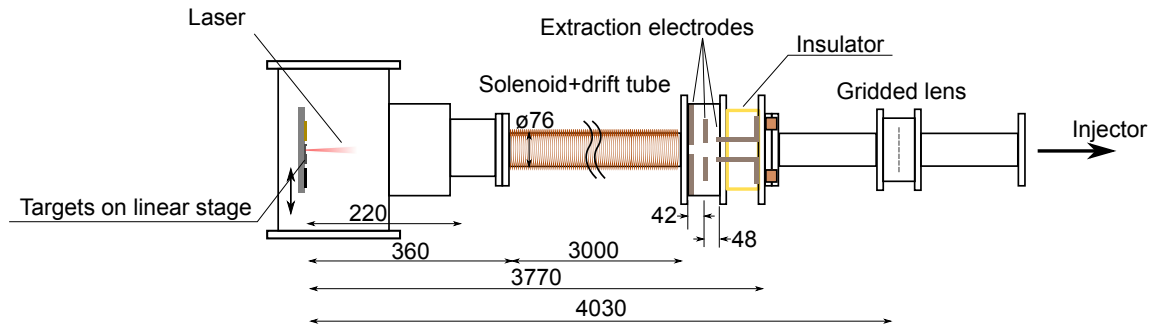


Figure A.1: Schematic diagram of experimental setup for beam current measurement.

Table A.1: Laser conditions for beam current measurement.

Laser Model	modified Quantel Brilliant B TWINS
Laser type	Nd:YAG Laser
Wave length	1064 nm
Pulse width (FWHM)	6 ns
Spot size	0.31 cm <sup>2</sup>
Laser energy on target	420 mJ
Power density	$2.3 \times 10^8$ W/cm <sup>2</sup>

### A.1.1 Experimental setup for beam current measurement

Figure A.1 is a schematic diagram of the experimental setup. We used several types of materials as target plates (Li, Al, Fe, and Au). The targets were placed onto a linear stage that allows the target motion and selection without breaking the vacuum and helps maintain suitable target surface. The targets were installed into a vacuum chamber evacuated to  $9 \times 10^{-6}$  Pa. Table A.1 is laser conditions. The laser with the power density produces singly charged ions mainly.

The length and the inner diameter of the solenoid are 3000 mm and 76 mm, respectively. A wire with 2.1 mm in diameter was turned 2860 times totally and 2 layers. The solenoid was energized by a DC power supply.

The extraction system was the same as explained in the chapter 5. The vacuum target chamber and the solenoid were charged up to around 20 kV. The potential of the intermediate electrode was adjusted for each ion species to extract a parallel beam. We measured the beam current with a current transformer (ACCT-S-082) and a metal mesh added to a

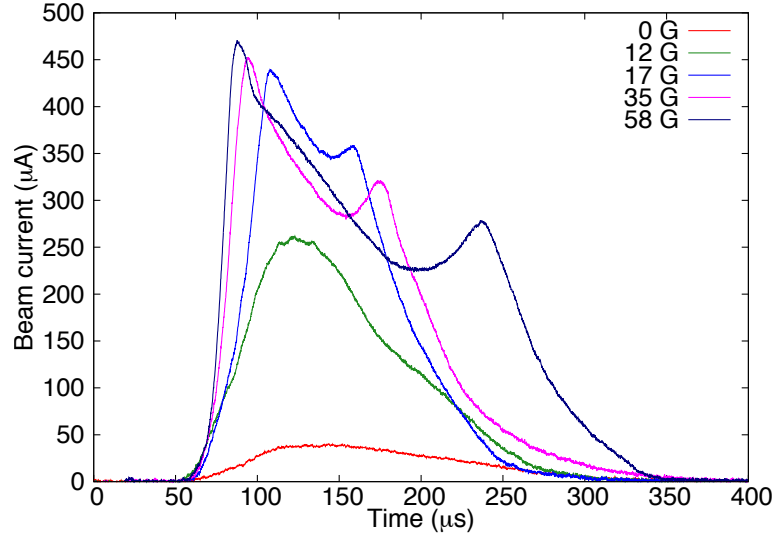


Figure A.2: Iron beam current waveforms measured by a current transformer.

gridded lens. When the current waveforms measured by the detectors were similar, the ion beam was evaluated to be parallel.

### A.1.2 Results and discussion

Figure A.2 shows the iron beam current waveforms measured by the current transformer. The time is referenced from the laser shot. Each curve is an average of eight data taken under a same condition. The red curve represents the current waveform without magnetic field and the others show the waveforms with various field strength. The peak current was enhanced up to 10 times with increase in the magnetic field from 0 to little less than 17 G. When the magnetic field increased over 17 G, the peak current was saturated around 450  $\mu\text{A}$ . On the other hand, the current in the tail part of the waveform kept increasing. This means that the total charge within a single beam pulse also kept increasing.

We measured the current waveforms of the other ion species and calculated the ratios of the peak current and the total charge with/without the magnetic field as shown in Fig. A.3. As shown in Fig. A.3 (a), for all species, the ratio of the peak current increased with increasing magnetic field. For the ion species other than Al, the ratios of the peak current became 10 with less than 100 G. Then, the rate of increase of the ratios for Li, Fe, and Au became smaller. This tendency was not observed for Al and Si. A larger magnetic

field could not be applied because the plasma ion current became too high to be extracted. On the other hand, when we compare the ratios of the light and heavy ions with a same magnetic flux density such as 10 G, we can find that the beam current of the lighter ions were enhanced more largely than that of the heavier ions.

The total charges shown in Fig. A.3 (b) shows similar tendencies. As for all the ions, the ratios of the total charges increased with increasing the magnetic field. The ratios for the species other than Al became around 10 with the magnetic field less than 100 G. The rate of increase for Li, Fe, and Au became smaller after certain magnetic flux densities. The reason of the decrease of the rate is that the current around the peak did not increase over 20 G while the current at the tail part of the waveform continued to increase. On the other hand, the comparison of the ratios with a same magnetic flux density shows that the total charges of the lighter ions were more amplified than those of the heavier ions.

### A.1.3 Summary

To investigate effects of a solenoid on beam current extracted for several ion species, we measured the beam current and the total charge within a single beam pulse. We found that magnetic field less than 100 G can enhance the peak current and the total charge of any ion species other than Al by 10 times. On the other hand, the rate of increase of the peak current as a function of magnetic flux density became smaller when the field became larger than certain values depending on the species. In addition, the results showed that the magnetic field is more effective on the lighter ions.

## A.2 Influence on beam extraction

In operation of the low charge laser ion source in BNL, the solenoid is mainly operated around 5 G to enhance the beam current by 1.5 times and compensate the current decrease due to the degradation of the target surface. However, the field may increase the emittance by causing some fluctuations of the plasma [28, 33, 59]. Namely, the fluctuation affects the transverse velocity of the plasma resulting in the fluctuation of the emission surface. To investigate the influences on the extraction and the beam optics, we measured the phase

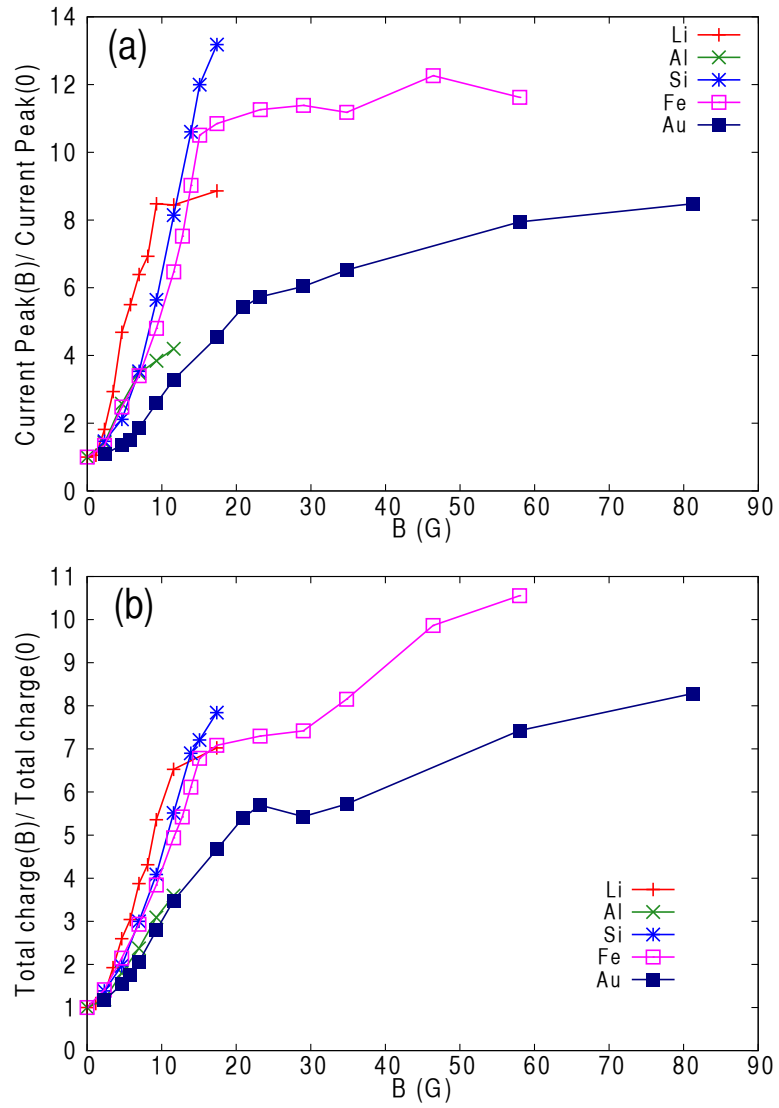


Figure A.3: Amplifications of the peak current and the total charge within a beam pulse as a function of the magnetic flux density.

space profile and obtained Twiss parameters with a pepper pot monitor in the test beam line [60].

### A.2.1 Experimental setup for phase space profile measurement

Figure A.4 is a schematic diagram of the setup for the phase space profile measurement. An iron plate target was placed in a vacuum chamber evacuated to  $\sim 6 \times 10^{-4}$  Pa. The laser condition is shown in Table A.2.

A 3 m solenoid consisted of 1 m and 2 m solenoids. As for the both solenoids, the inner diameter was 76 mm. The winding number of the copper wire of 2 mm in diameter of the 1 m solenoid was 475 turns with 9 layers. The winding number of the 2 m solenoid was 950 turns with 9 layers. The magnetic flux density was set to 4.2 G.

An ion beam was extracted by an extractor consisting of 3 electrodes. The target vacuum chamber and the solenoid was charged up at 20 kV. The voltage of the intermediate electrode was 18.5 kV. A gridded lens at a voltage of -7kV was placed to transport the beam.

A pepper pot monitor was composed of a mask of pinholes, a multi channel plate, a phosphor, and a ccd camera. The mask was a tungsten foil with 100  $\mu\text{m}$  in thickness and 43 mm in diameter. The pinholes with 100  $\mu\text{m}$  in diameter were spaced 2 mm horizontally and vertically. The mask was covered with two 0.5 mm thick copper plate with the same structure of the mask. The multi channel plate was placed at a distance of 11 mm from the mask, and the phosphor (P64) was mounted behind the plate. The image of the beamlets on the phosphor screen was taken by the ccd camera (Sony XCD-SX910). The phosphor had decay time 300 ns. We opened the shutter of the camera by sending a trigger signal and controlled the opening time. We measured the integrated phase space profile by opening the shutter of the camera all over the beam pulse. We also measured the variation of the phase space profile by opening the camera shutter for 20  $\mu\text{s}$  and changing the time of the trigger.

Besides the phase space profile measurement, we also measured the plasma ion current density into the extraction electrodes with a detector. The detector consisted of an aperture, a biased metal mesh, and a Faraday cup as shown in Fig. A.5 and Fig. A.6. When the



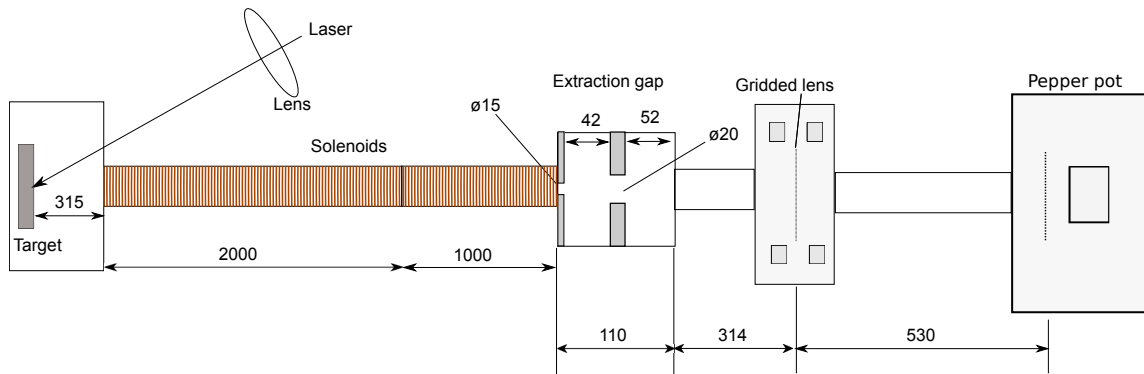


Figure A.4: Schematic diagram of experimental setup for beam profile measurement.

Table A.2: Laser conditions for beam profile measurement.

Laser Model	Quantel Brilliant B TWINS
Laser type	Nd:YAG Laser
Wave length	1064 nm
Pulse width (FWHM)	6 ns
Spot size	$0.38 \text{ cm}^2$
Laser energy on target	450 mJ
Power density	$2.0 \times 10^8 \text{ W/cm}^2$

plasma enters the detector, the electric field between the aperture and the mesh repels the electron and accelerates the ions whose current is detected by the cup. When this measurement, we set the detector at the exit and the center axis of the solenoid.

## A.2.2 Results and discussion

Figure A.7 shows the plasma ion current density waveform at the exit of the solenoid. The red curve shows the current density waveform without magnetic field and the green curve shows that with the field of 4.2 G. The current density around the peak around  $10 \mu\text{s}$  was enhanced by around 1.4 times. A peak was formed around  $30 \mu\text{s}$  due to lighter ions such as the carbon or the oxygen. Since the magnetic field is more effective on lighter ions, the peak current density of the lighter ions was enhanced more largely than that of the iron ions.

A typical phase space profile in transverse X-X' plane is shown in Fig. A.8. An RMS

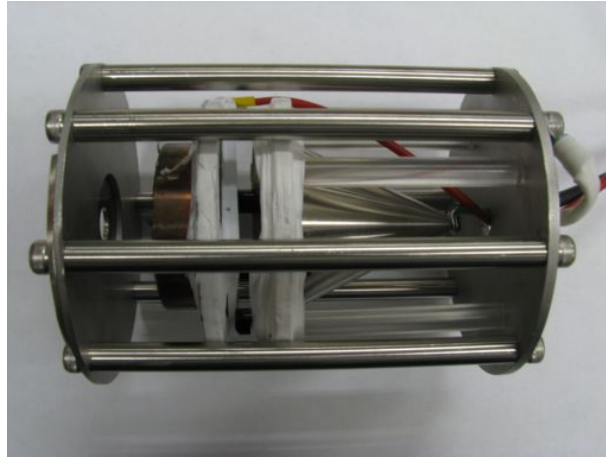


Figure A.5: Photo of Faraday cup.

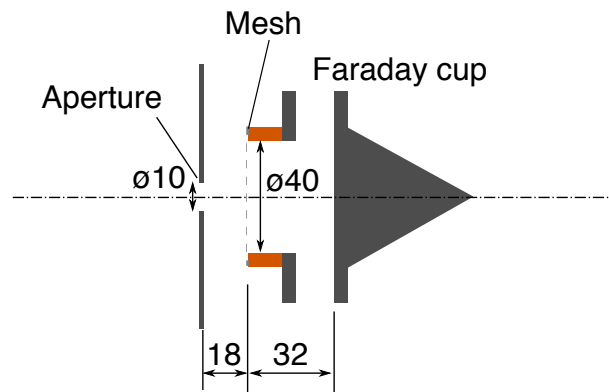


Figure A.6: Diagram of Faraday cup.

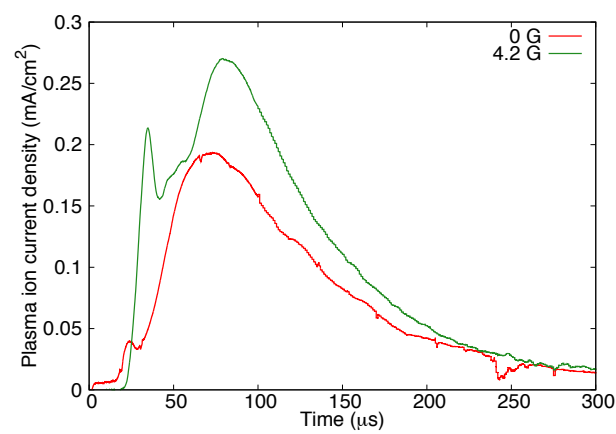


Figure A.7: Plasma ion current density waveform at the exit of the solenoid.

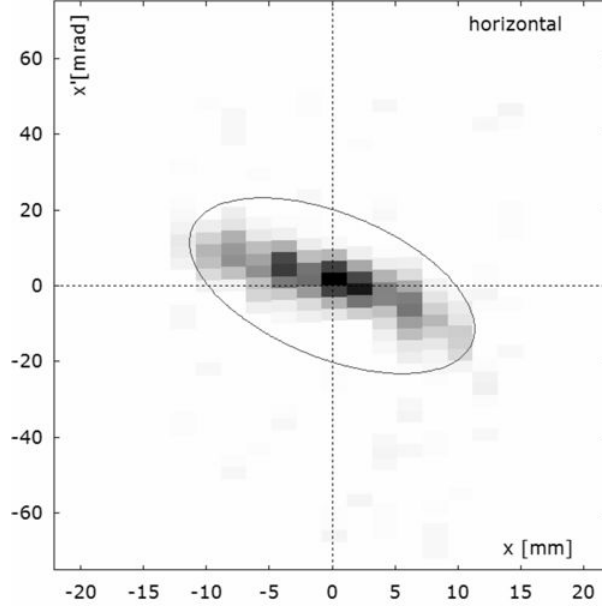


Figure A.8: Typical phase space profile in X-X' plane.

Table A.3: Integrated Twiss parameters.

Magnetic flux density	0 G	4.2 G
$\alpha$	0.68	0.66
$\beta$ (mm/mrad)	0.61	0.54
$\gamma$ (mrad/mm)	2.4	2.6
Normalized $\varepsilon_x$ ( $\pi$ mm mrad)	0.032	0.035

ellipse was fit to the profile to obtain the Twiss parameters,  $\alpha$ ,  $\beta$ ,  $\gamma$ , and normalized emittance  $\varepsilon$ .

We measured the integrated Twiss parameters over the entire period of a beam pulse. The results are shown in Table A.3. From the table, we can find almost no effect of the solenoid on the parameters.

We also measured the Twiss parameters as a function of time from laser shots as shown in Figs. A.9. The red plots show the Twiss parameters without magnetic field. As shown in Fig. A.9(a),  $\alpha$  varied positive to negative. This variation shows the variation of the beam divergence at the monitor within the beam pulse. Namely, the beam around the head of the pulse was converging, the beam around the center was parallel while forming waist, and the beam around the tail was diverging. The diverging at the tail means that the beam at the

tail over-focused before reaching the monitor. The reason of the behaviors is the variation of the divergent angle of the beam during the beam extraction. As shown in Fig. A.9(b),  $\beta$  was minimum around 100  $\mu\text{s}$ . This means that the diameter of the beam was minimum around 100  $\mu\text{s}$ . This is consistent with that  $\alpha$  became 0 around 100  $\mu\text{s}$  while forming the beam waist.  $\gamma$  was determined by  $\beta\gamma - \alpha^2 = 1$ .

As shown in Fig. A.9(d),  $\varepsilon$  from 60 to 180  $\mu\text{s}$  were much smaller than the integrated emittance. This is because that the integrated value was determined mainly by an  $\varepsilon$  which gave the maximum intensity. In addition, the divergent angle variation also would cause the ellipse rotation in the phase space and consequently the increase of the integrated  $\varepsilon$ .

The green plots in Fig. A.9 show the Twiss parameters with the magnetic field. As shown in Fig. A.9(a), (b), and (c), for  $\alpha$ ,  $\beta$ , and  $\gamma$ , significant differences with the fields of 0 and 4.2 G were not observed. On the other hand, as shown in Fig. A.9(d), from 50 to 150  $\mu\text{s}$ , the  $\varepsilon$  with the field was larger than that without the field. Figure A.7 showed that the plasma ion current density was enhanced mainly from 50 to 150  $\mu\text{s}$ . This means that the plasma within the duration was affected strongly. Therefore, these show that the increase of  $\varepsilon$  from 50 to 150  $\mu\text{s}$  was caused by the magnetic field. On the other hand, the increase was 70 % and still smaller than the integrated emittance. Therefore, one can say that the influence of the solenoid on the extraction is small that the solenoid does not affect the beam optics much in the practical setup.

### A.2.3 Summary

We measured the phase space profile and Twiss parameters with the solenoidal field of 4.2 G to investigate the effects on the beam extraction. We did not observed the significant differences of  $\alpha$ ,  $\beta$ , and  $\gamma$  between 0 G and 4.2 G. On the other hand, we observed that the emittance at a time increased by 70 %. However, the integrated emittance over the beam pulse did not changed since the integrated emittance was much larger than that at a time even without magnetic field. Therefore, the results showed that the solenoid does not affect the beam optics much in practical setup.

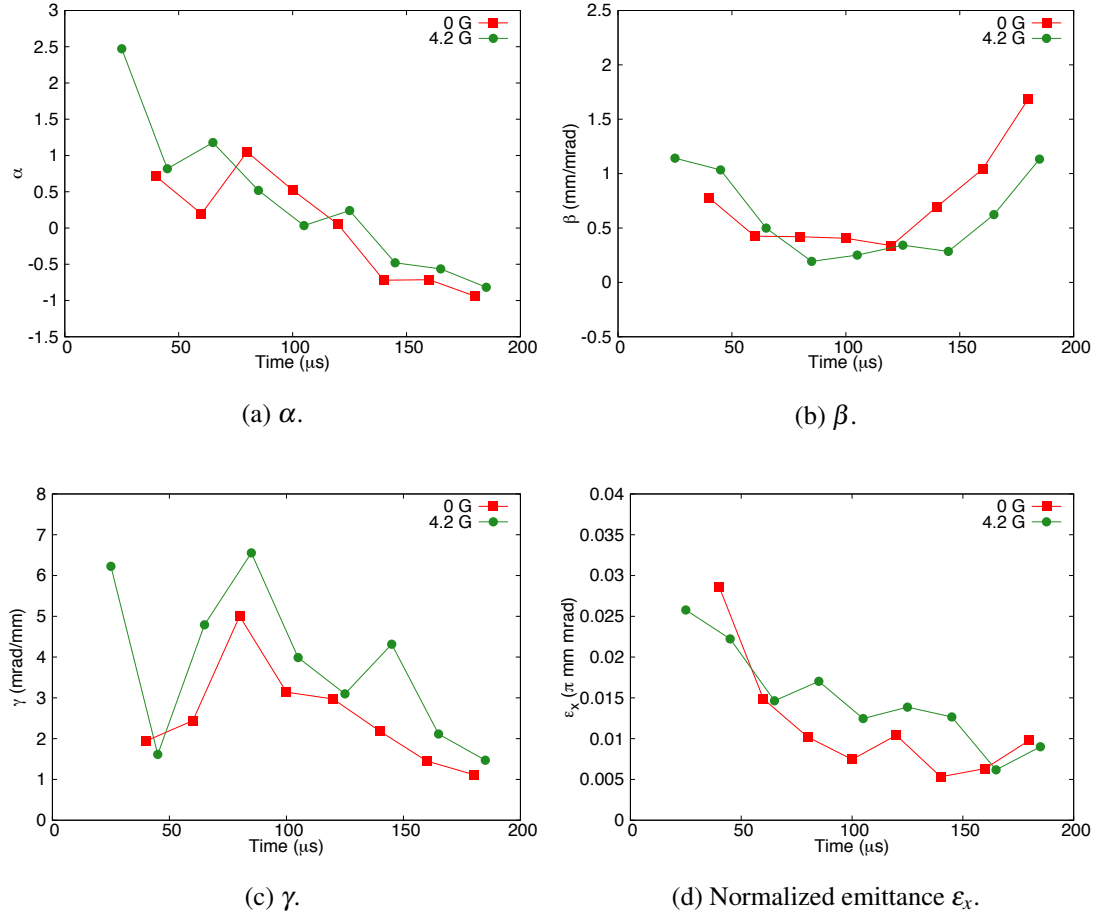


Figure A.9: Twiss parameters as a function of time from laser shot.

Table A.4: Laser specifications for current measurement in solenoid.

Laser Model	THALES SAGA 230
Laser type	Nd:YAG Laser
Wave length	1064 nm
Pulse width (FWHM)	6 ns
Spot size	0.24 cm <sup>2</sup>
Laser energy on target	630 mJ
Power density	$4.4 \times 10^8$ W/cm <sup>2</sup>

### A.3 Plasma ion current in solenoid

Confinement of a laser plasma with a magnetic field larger than 100 G has been studied for plasma physics [61, 62] and the application of the field to a laser ion source also has been discuss [14, 30, 31]. However, the mechanism of the guide by several tens of gauss has not been clarified. Therefore, we investigated the guide of the plasma by measuring the plasma ion current in the solenoid [63] and compared them with the results obtained in the previous sections.

#### A.3.1 Experimental setup for plasma ion current measurement in solenoid

Figure A.10 is a schematic diagram of the setup for the plasma ion current measurement. An iron target was placed in a vacuum chamber evacuated to  $4 \times 10^{-4}$  Pa. The laser conditions are shown in Table A.4. A solenoid with 480 mm in length and 74 mm in diameter was placed at a distance of 320 mm from the target. We calculated a magnetic field with a software (OPERA). The longitudinal components of the magnetic flux density on the solenoid axis is shown in Fig. A.11. The horizontal axis is the longitudinal distance from the entrance of the solenoid. This shows that the magnetic field is almost uniform in the solenoid. The plasma ion current was measured by a detector. The components and the dimensions of the detector were the same as those shown in Fig. 2.4 and Fig. 2.5. The co-moving electrons are repelled and the ions are accelerated by the electric field between the grounded aperture and the negatively biased mesh. The current of the ions are detected by the cup. The biased voltage of the mesh was -5 kV.

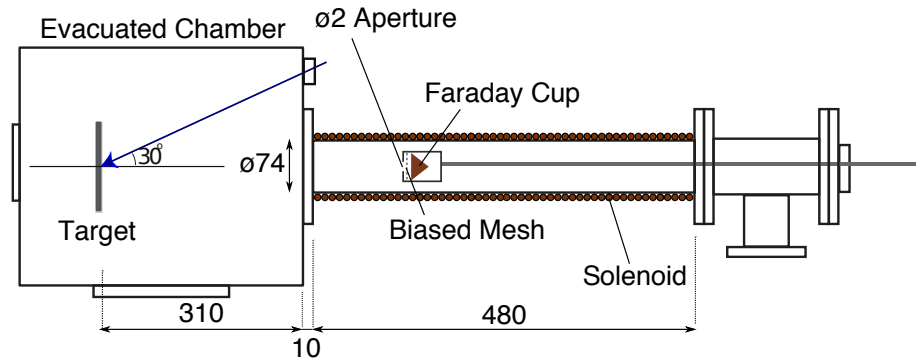


Figure A.10: Schematic diagram of experimental setup for current measurement in solenoid.

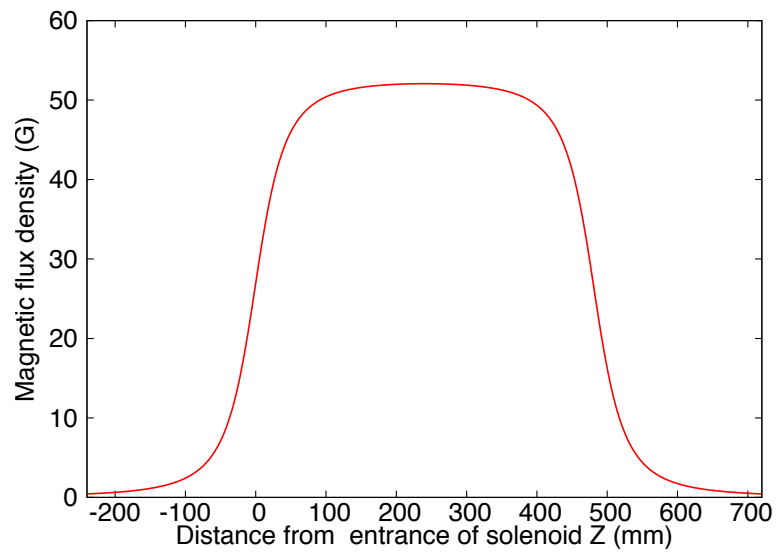


Figure A.11: Longitudinal components of magnetic flux density on axis as a function of longitudinal distance from entrance of solenoid.

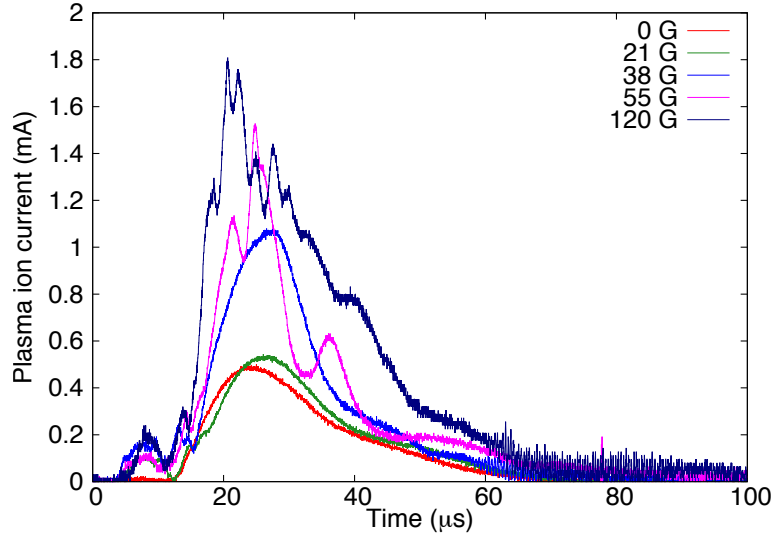


Figure A.12: Plasma ion current at distance waveform of 230 mm from solenoid entrance.

### A.3.2 Results and discussion

Figure A.12 shows the plasma ion current waveform at a distance of 230 mm from the solenoid entrance with various strengths of the magnetic field. The horizontal axis is the time from the laser shot. The magnetic flux density was the value at the center of the solenoid. The plasma ion current was enhanced as the magnetic field increased. When the magnetic field was smaller than 55 G, the current waveform was similar to that without magnetic field. On the other hand, when the field was larger than 55 G, a fluctuation appeared in the waveform. Because the reproducibility became much worse, we did not use the currents with larger than 55 G for following discussions.

We measured the plasma ion current waveform with changing the distance from the solenoid entrance, and then obtained the total charges within a single pulse by integrating the waveform. Figure A.13 shows the charge as a function of the distance with various magnetic field strengths. Each plot was an average of from 6 to 10 data. Without magnetic field, the total charge decreased monotonically. In addition, the plots of the charge were well fitted by the dashed curve proportional to the inverse square of the distance from the target. This shows that the plasma emitted radially from the laser spot on the target, and hence the detected charge was proportional to the detection solid angle.

As shown, the charge was enhanced as the magnetic field became larger. Moreover, the



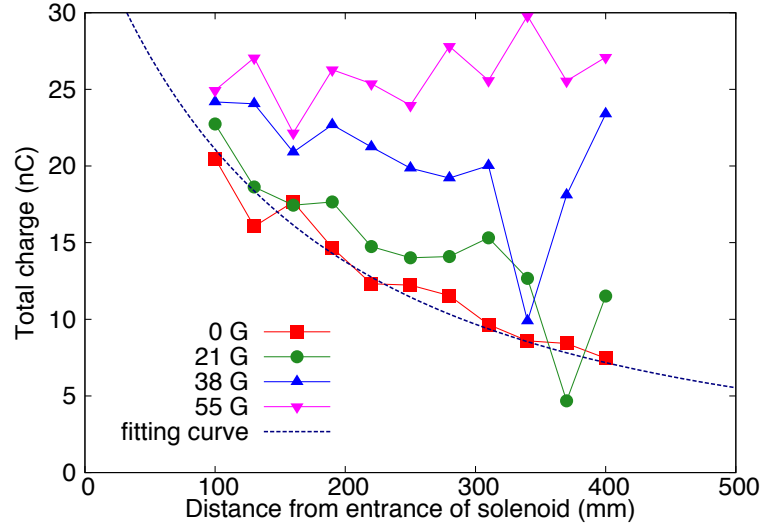


Figure A.13: Total charge within a single beam pulse as function of distance from solenoid entrance.

decrease rate of the charge as a function of the distance became smaller with increase in the magnetic field and then was almost constant with the field of 38 and 55 G. The decrease of the rate means that the divergent of the ions decreased due to the guiding by the magnetic field. Furthermore, the constant charge shows that the plasma can be confined transversely for 50 cm with the solenoid.

From Fig. A.13, the total charge is expected to be constant (25 nC) even if we extend the solenoid to 3 m. On the other hand, the charge without magnetic field is expected to be 0.3 nC by using the fitting curve proportional to the inverse square of the distance from the target. Thus, we expect to obtain 80 times larger charge at the exit of 3 m solenoid of 50 G. However, we obtained only 10 times larger charge experimentally as shown in Fig. A.3 (b). This shows that the charge was not kept to be constant for 3 m. A previous research [28] showed that plasma ion current at the exit of a 3 m solenoid was unstable at 9 G while we observed that with larger than 50 G. This may mean that a threshold of the magnetic flux density causing the instability depends on the length of guide, and the instability occurred after 50 cm in the experiment using 3 m solenoid.

### **A.3.3 Summary**

We measured the plasma ion current in a 50 cm solenoid and obtained the total charge as a function of the longitudinal distance from the entrance of the solenoid. The results showed that the magnetic field enhanced the total charge and especially the field of 50 G kept the charge constant for 50 cm. This shows that we can confine the plasma transversely for 50 cm with the solenoid. On the other hand, the experiment with 3 m solenoid discussed in the previous section showed that the plasma was not confined for 3 m at 50 G. Therefore, this shows that the confinement was broken between 50 cm and 3 m in the 3 m solenoid.

## **A.4 Concluding remarks**

From a view point of ion sources, we investigated a plasma guide by a moderate magnetic field of from 1 to 100 G generated by a long solenoid on a laser ablation plasma. We found that a 3 m solenoidal field less than 100 G can enhance the current and the total charge within a pulse 10 times for almost any species. The phase space profile measurements showed that a 3 m solenoidal field of 5 G can increase the current by 1.4 times without influences on the beam extraction and integrated emittance over the beam pulse. Furthermore, we measured the total charge on a solenoidal axis in the solenoid to investigate the behavior of the plasma. The results showed that the the plasma was confined transversely with 50 G through the distance of 50 cm.

# Bibliography

- [1] H. Hahn, E. Forsyth, H. Foelsche, M. Harrison, J. Kewisch, G. Parzen, S. Peggs, E. Raka, A. Ruggiero, A. Stevens, *et al.*, “The rhic design overview,” *Nuclear Instruments and Methods in Physics Research Section A: Accelerators, Spectrometers, Detectors and Associated Equipment*, vol. 499, no. 2, pp. 245–263, 2003.
- [2] J. M. Jowett, “The lhc as a nucleus–nucleus collider,” *Journal of Physics G: Nuclear and Particle Physics*, vol. 35, no. 10, p. 104028, 2008.
- [3] H. Sakurai, “Riken ribf project—present status and future plan—,” vol. 1269, no. 1, pp. 84–90, 2010.
- [4] P. Spiller and G. Franchetti, “The fair accelerator project at gsi,” *Nuclear Instruments and Methods in Physics Research Section A: Accelerators, Spectrometers, Detectors and Associated Equipment*, vol. 561, no. 2, pp. 305–309, 2006.
- [5] J. Wei, D. Arenius, E. Bernard, N. Bultman, F. Casagrande, S. Chouhan, C. Compton, K. Davidson, A. Facco, V. Ganni, *et al.*, “The frib project—accelerator challenges and progress,” *HIATC2012, Chicago, USA*, vol. 51, 2012.
- [6] J.-W. Xia, W.-L. Zhan, B.-W. Wei, Y. Yuan, M. Song, W. Zhang, X. Yang, P. Yuan, D. Gao, H. Zhao, *et al.*, “The heavy ion cooler-storage-ring project (hirfl-csr) at lanzhou,” *Nuclear Instruments and Methods in Physics Research Section A: Accelerators, Spectrometers, Detectors and Associated Equipment*, vol. 488, no. 1, pp. 11–25, 2002.
- [7] K. Noda, T. Furukawa, T. Fujisawa, Y. Iwata, T. Kanai, M. Kanazawa, A. Kitagawa,

- M. Komori, S. Minohara, T. Murakami, *et al.*, “New accelerator facility for carbon-ion cancer-therapy,” *Journal of radiation research*, vol. 48, no. Suppl. A, pp. A43–A54, 2007.
- [8] D. Lowenstein and A. Rusek, “Technical developments at the nasa space radiation laboratory,” *Radiation and environmental biophysics*, vol. 46, no. 2, pp. 91–94, 2007.
- [9] A. Tanaka, N. Shikazono, and Y. Hase, “Studies on biological effects of ion beams on lethality, molecular nature of mutation, mutation rate, and spectrum of mutation phenotype for mutation breeding in higher plants,” *Journal of radiation research*, vol. 51, no. 3, pp. 223–233, 2010.
- [10] J. Barnard, R. Bangerter, A. Faltens, T. Fessenden, A. Friedman, E. Lee, B. Logan, S. Lund, W. Meier, W. Sharp, *et al.*, “Induction accelerator architectures for heavy-ion fusion,” *Nuclear Instruments and Methods in Physics Research Section A: Accelerators, Spectrometers, Detectors and Associated Equipment*, vol. 415, no. 1, pp. 218–228, 1998.
- [11] K. Takayama and R. J. Briggs, *Induction Accelerators*. Springer Science & Business Media, 2011.
- [12] G. F. Tonon, “Laser sources for multiply-charged heavy ions,” *Nuclear Science, IEEE Transactions on*, vol. 19, p. 172, 1972.
- [13] V. Dubenkov, B. Sharkov, A. Golubev, A. Shumshurov, O. Shamaev, I. Roudskoy, A. Streltsov, Y. Satov, K. Makarov, Y. Smakovsky, *et al.*, “Acceleration of ta 10+ ions produced by laser ion source in rfq maxilac,” *Laser and particle beams*, vol. 14, no. 03, pp. 385–392, 1996.
- [14] V. Kutner, Y. A. Bykovsky, V. Gusev, Y. P. Kozyrev, and V. Peklenkov, “The laser ion source of multiply charged ions for the u-200 ln timer cyclotron,” *Review of scientific instruments*, vol. 63, no. 4, pp. 2835–2837, 1992.
- [15] S. Sha, H. Zhao, X. Guo, Z. Zhang, X. Fang, J. Guo, W. Zhang, W. Lu, Y. Cao,

- H. Ma, *et al.*, “Status of the laser ion source at impa),” *Review of scientific instruments*, vol. 83, no. 2, p. 02B303, 2012.
- [16] B. Sharkov and R. Scrivens, “Laser ion sources,” *Plasma Science, IEEE Transactions on*, vol. 33, no. 6, pp. 1778–1785, 2005.
- [17] A. Picciotto, J. Krasa, L. Laska, K. Rohlena, L. Torrisi, S. Gammino, A. Mezzasalma, and F. Caridi, “Plasma temperature and ion current analysis of gold ablation at different laser power rates,” *Nuclear Instruments and Methods in Physics Research Section B: Beam Interactions with Materials and Atoms*, vol. 247, no. 2, pp. 261–267, 2006.
- [18] T. Kanesue, M. Okamura, J. Alessi, E. Beebe, A. Pikin, D. Raparia, C. Liaw, R. Lambiase, V. LoDestro, M. Costanzo, R. Lehn, L. DeSanto, R. Olsen, A. Steszyn, M. Sekine, S. Ikeda, and K. Kondo, “THE COMMISSIONING OF THE LASER ION SOURCE FOR RHIC EBIS,” *Proceedings of IPAC2014, Dresden, Germany*, pp. 1890 – 1892, 2014.
- [19] J. Alessi, D. Barton, E. Beebe, S. Bellavia, O. Gould, A. Kponou, R. Lambiase, R. Lockey, A. McNerney, M. Mapes, *et al.*, “The brookhaven national laboratory electron beam ion source for rhica),” *Review of Scientific Instruments*, vol. 81, no. 2, p. 02A509, 2010.
- [20] D. Doria, A. Lorusso, F. Belloni, V. Nassisi, L. Torrisi, and S. Gammino, “A study of the parameters of particles ejected from a laser plasma,” *Laser and Particle Beams*, vol. 22, no. 04, pp. 461–467, 2004.
- [21] M. Muramatsu, A. Kitagawa, Y. Sakamoto, S. Sato, Y. Sato, H. Ogawa, S. Yamada, H. Ogawa, Y. Yoshida, and A. Drentje, “Development of a compact electron-cyclotron-resonance ion source for high-energy carbon-ion therapy,” *Review of scientific instruments*, vol. 76, no. 11, p. 113304, 2005.
- [22] Y. Higurashi, J. Ohnishi, T. Nakagawa, H. Haba, M. Tamura, T. Aihara, M. Fujimaki, M. Komiyama, A. Uchiyama, and O. Kamigaito, “Results of riken superconducting electron cyclotron resonance ion source with 28 ghza),” *Review of Scientific Instruments*, vol. 83, no. 2, p. 02A308, 2012.

- [23] A. T. Forrester, *Large ion beams: fundamentals of generation and propagation*. Wiley-Interscience, New York, NY, 1988.
- [24] L. Torrissi, L. Andò, S. Gammino, J. Krasa, and L. Laska, “Ion and neutral emission from pulsed laser irradiation of metals,” *Nuclear Instruments and Methods in Physics Research Section B: Beam Interactions with Materials and Atoms*, vol. 184, no. 3, pp. 327–336, 2001.
- [25] Y. Tsui, R. Fedosejevs, and A. Offenberger, “Experimental study of charge state distribution from krf and ruby laser-produced plasmas,” *Physics of Fluids B: Plasma Physics (1989-1993)*, vol. 5, no. 9, pp. 3357–3368, 1993.
- [26] R. Kelly and R. Dreyfus, “On the effect of knudsen-layer formation on studies of vaporization, sputtering, and desorption,” *Surface science*, vol. 198, no. 1, pp. 263–276, 1988.
- [27] J. Wołowski, J. Badziak, I. Ivanova-Stanik, P. Parys, W. Stepniewski, and E. Woryna, “Magnetic field influence on laser-produced ion stream,” *Review of scientific instruments*, vol. 75, no. 5, pp. 1353–1356, 2004.
- [28] K. Takahashi, M. Okamura, M. Sekine, E. Cushing, and P. Jandovitz, “Effect of solenoidal magnetic field on drifting laser plasma,” *Proceedings of APPLICATION OF ACCELERATORS IN RESEARCH AND INDUSTRY: Twenty-Second International Conference, Ft. Worth, TX, USA*, vol. 1525, no. 1, pp. 241–244, 2013.
- [29] T. Kanesue, Y. Fuwa, K. Kondo, and M. Okamura, “Laser ion source with solenoid field,” *Applied Physics Letters*, vol. 105, no. 19, p. 193506, 2014.
- [30] J. Wolowski, L. Celona, G. Ciavola, S. Gammino, J. Krása, L. Láska, P. Parys, K. Rohlena, L. Torrissi, and E. Woryna, “Expansion of tungsten ions emitted from laser-produced plasma in axial magnetic and electric fields,” *Laser and Particle Beams*, vol. 20, no. 01, pp. 113–118, 2002.
- [31] M. Okamura, A. Adeyemi, T. Kanesue, J. Tamura, K. Kondo, and R. Dabrowski,

- “Magnetic plasma confinement for laser ion source,” *Review of Scientific Instruments*, vol. 81, p. 02A510, 2010.
- [32] M. Goossens, *An Introduction to Plasma Astrophysics and Magnetohydrodynamics*. Kluwer Academic Publishers, 2003.
- [33] S. Robertson, “Magnetic guiding, focusing and compression of an intense charge-neutral ion beam,” *Physics of Fluids (1958-1988)*, vol. 26, no. 4, pp. 1129–1138, 1983.
- [34] S. Robertson, “Collective focusing of an intense ion beam,” *Physical Review Letters*, vol. 48, no. 3, p. 149, 1982.
- [35] S. Robertson, “Collective focusing of a charge-neutral ion beam with warm electrons,” *Journal of applied physics*, vol. 59, no. 5, pp. 1765–1767, 1986.
- [36] R. Kraft, B. Kusse, and J. Moschella, “Collective focusing of an intense pulsed ion beam,” *Physics of Fluids (1958-1988)*, vol. 30, no. 1, pp. 245–251, 1987.
- [37] M. A. Dorf, I. D. Kaganovich, E. A. Startsev, and R. C. Davidson, “Collective focusing of intense ion beam pulses for high-energy density physics applications,” *Physics of Plasmas (1994-present)*, vol. 18, no. 3, p. 033106, 2011.
- [38] I. Weaver, G. Martin, W. Graham, T. Morrow, and C. Lewis, “The langmuir probe as a diagnostic of the electron component within low temperature laser ablated plasma plumes,” *Review of scientific instruments*, vol. 70, no. 3, pp. 1801–1805, 1999.
- [39] L. Spitzer, *Physics of Fully Ionized Gases*. Wiley Inter- science, New York, 1962.
- [40] J. Hendron, C. Mahony, T. Morrow, and W. Graham, “Langmuir probe measurements of plasma parameters in the late stages of a laser ablated plume,” *Journal of applied physics*, vol. 81, no. 5, pp. 2131–2134, 1997.
- [41] B. Toftmann, J. Schou, T. Hansen, and J. Lunney, “Angular distribution of electron temperature and density in a laser-ablation plume,” *Physical review letters*, vol. 84, no. 17, p. 3998, 2000.

- [42] B. Toftmann, J. Schou, T. Hansen, and J. Lunney, "Evolution of the plasma parameters in the expanding laser ablation plume of silver," *Applied surface science*, vol. 186, no. 1, pp. 293–297, 2002.
- [43] J. G. Lunney, B. Doggett, and Y. Kaufman, "Langmuir probe diagnosis of laser ablation plasmas," vol. 59, no. 1, p. 470, 2007.
- [44] B. Ilyas, M. Hussain, A. Dogar, S. Ullah, A. Nadeem, and A. Qayyum, "Temporal behavior of the tungsten plasma produced by 1064nm pulsed nd-yag laser," *Nuclear Instruments and Methods in Physics Research Section B: Beam Interactions with Materials and Atoms*, vol. 295, pp. 81–84, 2013.
- [45] S. Ikeda, M. Okamura, and K. Horioka, "Control of plasma flux with pulsed solenoid for laser ion source," *Proceedings of IPAC2014, Dresden, Germany*, pp. 601 – 603, 2014.
- [46] S. Ikeda, K. Horioka, and M. Okamura, "Investigation of the tail of a Fe plasma plume passing through solenoidal magnetic field for a laser ion source," *Plasma Science, IEEE Transactions on*, vol. 43, no. 10, pp. 3456–3460, 2014.
- [47] J. Kools, T. Baller, S. De Zwart, and J. Dieleman, "Gas flow dynamics in laser ablation deposition," *Journal of Applied Physics*, vol. 71, no. 9, pp. 4547–4556, 1992.
- [48] S. Ikeda, M. Romanelli, D. Cinquegrani, M. Sekine, M. Kumaki, Y. Fuwa, N. Munemoto, T. Kanesue, Q. Jin, M. Okamura, *et al.*, "Creation of mixed beam from alloy target and couple of pure targets with lasera)," *Review of Scientific Instruments*, vol. 85, no. 2, p. 02B913, 2014.
- [49] E. Everson, P. Pribyl, C. Constantin, A. Zylstra, D. Schaeffer, N. Kugland, and C. Niemann, "Design, construction, and calibration of a three-axis, high-frequency magnetic probe (b-dot probe) as a diagnostic for exploding plasmas," *Review of Scientific Instruments*, vol. 80, no. 11, p. 113505, 2009.



- [50] C. M. Franck, O. Grulke, and T. Klinger, “Magnetic fluctuation probe design and capacitive pickup rejection,” *Review of scientific instruments*, vol. 73, no. 11, pp. 3768–3771, 2002.
- [51] S. Ikeda, M. Nakajima, and K. Horioka, “Control of laser ablation plasma with longitudinal magnetic field,” *Plasma and Fusion Research*, vol. 7, no. 0, pp. 1201015–1201015, 2012.
- [52] S. Ikeda, M. Nakajima, J. Hasegawa, T. Kawamura, and K. Horioka, “Magnetic control of laser ablation plasma for high-flux ion injectors,” *Nuclear Instruments and Methods in Physics Research Section A: Accelerators, Spectrometers, Detectors and Associated Equipment*, vol. 733, pp. 103–106, 2014.
- [53] E. Woryna, P. Parys, J. Wołowski, *et al.*, “Corpuscular diagnostics and processing methods applied in investigations of laser-produced plasma as a source of highly ionized ions,” *Laser and Particle beams*, vol. 14, no. 03, pp. 293–321, 1996.
- [54] T. Green, “Space charge effects in plasma particle analyzers,” *Plasma Physics*, vol. 12, no. 11, p. 877, 1970.
- [55] N. M. Bulgakova, A. V. Bulgakov, and O. F. Bobrenok, “Double layer effects in laser-ablation plasma plumes,” *Physical Review E*, vol. 62, no. 4, p. 5624, 2000.
- [56] J. Zheng, Z. Huang, D. Shaw, and H. Kwok, “Generation of high-energy atomic beams in laser-superconducting target interactions,” *Applied physics letters*, vol. 54, no. 3, pp. 280–282, 1989.
- [57] S. Ikeda, M. Costanzo, T. Kanesue, R. Lambiase, C.-J. Liaw, and M. Okamura, “Control of laser ablation plasma by pulsed magnetic field for heavy ion beam production,” *Proceedings of HIAT2015, Yokohama, Japan*, to be published.
- [58] S. Ikeda, M. Kumaki, T. Kanesue, and M. Okamura, “Effect of the solenoid in various conditions of the laser ion source at brookhaven national laboratory,” *Review of Scientific Instruments*, vol. 87, no. 2, p. 02A915, 2016.

- 
- [59] G. Ohlsen, J. McKibben, R. Stevens, and G. Lawrence, “Depolarization and emittance degradation effects associated with charge transfer in a magnetic field,” *Nuclear Instruments and Methods*, vol. 73, no. 1, pp. 45–52, 1969.
- [60] S. Ikeda, M. Romanelli, D. Cinquegrani, M. Sekine, M. Kumaki, Y. Fuwa, T. Kanetsue, M. Okamura, and K. Horioka, “Investigation of effect of solenoid magnet on emittances of ion beam from laser ablation plasmaa),” *Review of Scientific Instruments*, vol. 85, no. 2, p. 02B919, 2014.
- [61] R. Tuckfield and F. Schwirzke, “Dynamics of a laser created plasma expanding in a magnetic field,” *Plasma physics*, vol. 11, no. 1, p. 11, 1969.
- [62] S. Sudo, T. Sekiguchi, and K. Sato, “Re-thermalisation and flow of laser-produced plasmas in a uniform magnetic field,” *Journal of Physics D: Applied Physics*, vol. 11, no. 3, p. 389, 1978.
- [63] S. Ikeda, K. Takahashi, M. Okamura, and K. Horioka, “Behavior of moving plasma in solenoidal magnetic field in a laser ion source,” *Review of Scientific Instruments*, vol. 87, no. 2, p. 02A912, 2016.